A Laboratory Study of Railway Ballast Behaviour under Traffic Loading and Tamping Maintenance

by

Bhanitiz Aursudkij, MEng (Hons)

Thesis submitted to The University of Nottingham

for the degree of Doctor of Philosophy

September 2007

Abstract

Since it is difficult to conduct railway ballast testing in-situ, it is important to simulate the conditions experienced in the real track environment and study their influences on ballast in a controlled experimental manner. In this research, extensive laboratory tests were performed on three types of ballast, namely granites A and B and limestone. The grading of the tested ballast conforms to the grading specification in The Railway Specification RT/CE/S/006 Issue 3 (2000). The major laboratory tests in this research were used to simulate the traffic loading and tamping maintenance undertaken by the newly developed Railway Test Facility (RTF) and large-scale triaxial test facility.

The Railway Test Facility is a railway research facility that is housed in a 2.1 m (width) x 4.1 m (length) x 1.9 m (depth) concrete pit and comprises subgrade material, ballast, and three sleepers. The sleepers are loaded with out of phase sinusoidal loading to simulate traffic loading. The ballast in the facility can also be tamped by a tamping bank which is a modified real Plasser tamping machine. Ballast breakage in the RTF was quantified by placing columns of painted ballast beneath a pair of the tamping tines, in the location where the other pair of tamping tines squeeze, and under the rail seating. The painted ballast was collected by hand and sieved after each test.

It was found from the RTF tests that the amount of breakage generated from the tests was not comparable to the fouling in the real track environment. This

is because the external input (such as wagon spillage and airborne dirt) which is the major source of fouling material was not included in the tests. Furthermore, plunging of the tamping tines caused more damage to the ballast than squeezing. The tested ballast was also subjected to Los Angeles Abrasion (LAA) and Micro-Deval Attrition (MDA) tests. It was found that the LAA and MDA values correlated well with the ballast damage from tamping and could indicate the durability of ballast.

The large-scale triaxial test machine was specially manufactured for testing a cylindrical ballast sample with 300-mm diameter and 450-mm height and can perform both cyclic and monotonic tests with constant confining stress. Instead of using on-sample instrumentations to measure the radial movement of the sample, it measures sample volume change by measuring a head difference between the level of water that surrounds the sample and a fixed reference water level with a differential pressure transducer.

The test results from cyclic tests were related to the simulated traffic loading test in the RTF by an elastic computer model. Even with some deficiencies, the model could relate the stress condition in the RTF to cyclic triaxial test with different confining stresses and q/p' stress ratios.

Acknowledgements

I would like to thank my main supervisor, Professor Glenn McDowell, for his invaluable guidance and supervision throughout the whole research. This thesis would not have been completed without his support. I would also like to express my sincere gratitude to the following people for their advice and help:

- Professor Andy Collop, my co-supervisor, for his helpful advice.
- Mr. Barry Brodrick, Chief experimental officer, for his thoughts on both experiments and the thesis. His suggestions have always been excellent and helpful.
- Dr. Nick Thom and Mr. Andrew Dawson from the University of Nottingham, Dr. David Thompson from Balfour Beatty Rail Technologies Limited, and Mr. Eric Hornby from Micron Hydraulics for their technical support.
- Mr. John Bradshaw-Bullock from Foster Yeoman Ltd. for his help on providing the ballast for the experiments and Mr. John Harris from Lafarge Aggregates Ltd. for performing various ballast index tests.
- All technicians and experimental officers in the School of Civil Engineering for their help with the experiments, in particular Ian Richardson, Andrew Maddison, Bal Loyla, and Michael Langford.
- My fellow researchers in the School of Civil Engineering, in particular Wee Loon Lim, Cho Kwan, and Pongtana Vanichkobchinda.
- The Engineering and Physical Science Research Council (EPSRC) for funding this project.
- Finally, my greatest gratitude goes to my family and Ms. Napaon Chantarapitak for their constant support, belief, and encouragement.

Table of contents

List of figures

List of tables

Notation

a	Crack length
d	Particle size or distance between two flat platens
DPT	Differential pressure transducer
d_0	Reference particle size
D_y	Particle size at y percentage passing
D/d_{max}	Ratio of triaxial sample diameter and maximum particle size
E	Young's modulus
E_s	Secant modulus
E_t	Tangent modulus at zero axial strain
$\varepsilon_{a,r}$	Resilient axial strain
$\varepsilon_{a,p}$	Permanent axial strain
$\varepsilon_{v,r}$	Resilient volumetric strain
$\varepsilon_{v,p}$	Permanent volumetric axial strain
F	Force
FI_D	Ballast fouling index (Ionescu, 2004)
F_I	Ballast fouling index (Selig and Waters, 1994)
FI_P	Modification of ballast fouling index of Selig and Waters (1994)
GDP	German dynamic plate
G_C	Toughness
H/D	Height to diameter ratio of triaxial test sample
K	Stress intensity factor
K_{IC}	Fracture toughness
k_1 and k_2	Empirical constants

LAA	Los Angeles abrasion
LVDT	Linear variable differential transformer
m	Weibull modulus
MDA	Micro-Deval attrition
M_r	Resilient modulus
ν	Poisson's ratio
ODZ	Optimum degradation zone
p.d.f.	Probability density function
p'	Mean principal stress or stress invariant p'
P_S	Survival probability
P_x	Percentage passing at x mm sieve / 100
q	Deviatoric stress or stress invariant q
θ	Sum principal stresses
R^2	Correlation coefficient
RTF	Railway Test Facility
S	Standard deviation
S.E.	Standard error
σ	Stress
σ_0	Characteristic stress at which 37 % of particles survive
$\sigma_{0,d}$	Characteristic stress at which 37 % of particles of size d survive
σ_1	Major principal stress
σ_2	Intermediate principal stress
σ_3	Minor principal stress
σ_{av}	Average strength
UPT	Ultrasonic proximity transducer

1. Introduction

1.1. Background and problem definition

The rail network is one of the most important transportation systems in everyday life. It provides a fast means of transportation by a durable and economical system. To achieve optimum performance of the rail track, it is necessary to understand how track structure components work. Railway maintenance is also inevitable in order to attain this goal.

In the past, the train and track superstructure, such as rails and sleepers were the focus of attention of railway engineers. Less attention was given to the substructure such as ballast, subballast and subgrade even though they are as important as the superstructure. While the superstructure provides the main function of the railway, the substructure provides the foundation to support the superstructure and to help the superstructure to reach its optimum performance.

Track settlement occurs after long-term service. According to Selig and Waters (1994), ballast contributes the most to track settlement as shown in Figure 1.1 even though one of the functions of ballast is to restrain track geometry. Excessive settlement can cause poor passenger comfort, speed restriction, and potential derailment. The most conventional method of restoring the settlement is tamping. However, tamping also deteriorates the ballast in addition to the damage from traffic loading. Thus, it is important to study the degradation of ballast to increase and predict ballast life on the track, reduce waste ballast, minimise the frequency and cost of ballast replacement, and lead to further developments in the railway industry.

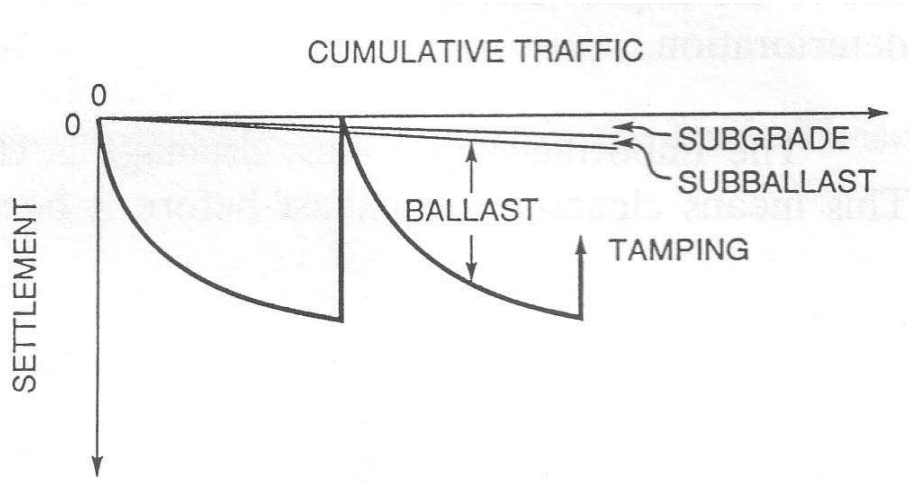

Figure 1.1. Substructure contributions to settlement (Selig and Waters, 1994)

Despite the problems associated with ballast, ballast is still a preferable choice for substructure material over other alternatives such as concrete slabs or asphalt. This is because ballast provides less stiff support (which is an important factor in case of differential settlement or subgrade failure), is more economical, and produces less noise (Profillidis, 2000).

1.2. Aims and objectives

The goal of this project is to provide an understanding of the railway ballast behaviour, including degradation, under traffic loading and tamping maintenance. The aims of this project can be stated as:

- To study the fracture behaviour of a range of single ballast particles.
- To develop a large-scale triaxial test facility and a test facility which can perform traffic loading simulation and laboratory tamping.

- To study ballast behaviour and degradation under stresses induced by traffic loading and tamping.

To achieve these aims, there are seven specific objectives:

1. A literature review on the behaviour of crushable soil and performance and degradation of ballast.
2. Measurement of the tensile strengths of single grains of ballast by single particle crushing tests, and the application of Weibull Statistics.
3. Design, build, and operation of a Railway Test Facility (RTF) for tamping tests and traffic loading simulation.
4. Simulation of traffic loading and tamping tests on ballast in the RTF to study ballast degradation.
5. Development of a large-scale triaxial test facility.
6. Large triaxial tests on ballast to study degradation and stress-strain behaviour as a function of stress level and stress ratio.
7. Relation of the triaxial test results to the simulated traffic loading test results.

1.3. Thesis outline

This thesis is divided into seven chapters. The brief outline of each chapter is given below.

A review of background knowledge and literature relevant to this work is presented in Chapter 2. It covers information on rail track environment, ballast,

particle breakage, behaviour of aggregates under monotonic and cyclic loading, and laboratory tests on ballast.

Chapter 3 focuses on the material properties and strength of three types of ballast that were used in all experiments in this project. Ballast was sent to Lafarge Aggregates Ltd. for Los Angeles abrasion, micro-Deval attrition, flakiness index, and water absorption tests. The strengths of ballast particles were also measured by compressing a ballast particle between two flat platens and analysed by Weibull statistics and the two-sample unpaired t-test.

The development of the Railway Test Facility (RTF) and large-scale triaxial test facility are described in Chapters 4 and 5. These chapters also include test procedures, analysis of test results, and a discussion of the findings.

Chapter 6 attempts to draw together the data from the RTF and triaxial tests. Lastly, Chapter 7 presents the conclusions of the work and recommendations for further research.

2. Literature review

2.1. Introduction

Railway ballast is one of the most important components in a rail track. It is a crushed granular material that supports the rails and sleeper. Various types of materials are used as ballast such as granite, limestone, or basalt. The chosen type of ballast material usually depends on the local availability.

This chapter presents a literature review related to ballast and its mechanical properties. The six sections of this literature review focus on

- Rail track environment
- Ballast in the track
- Particle breakage
- Behaviour of granular materials under monotonic loading
- Behaviour of granular materials under cyclic loading
- Previous laboratory tests on ballast

2.2. Rail track

2.2.1. Track components

Track components are divided into two parts, namely the superstructure and substructure which are the top and bottom parts as shown in Figure 2.1. The superstructure includes the rails, fastening system, and sleepers. The substructure includes the ballast, subballast, and subgrade.

The rails are a pair of longitudinal steel members which are in contact with the train wheels. Their functions are to guide the train in the desired direction and to transfer the traffic loading to the sleepers which are joined to the rails by the fastening system. The sleepers then transfer the load from the rails to the ballast and also restrain the rail movement by anchorage of the superstructure in the ballast.

Ballast is a crushed granular material placed as the top layer of the substructure and between sleepers in a track and has many functions. The most important ones are to resist vertical, lateral, and longitudinal forces applied to the sleepers and to provide resiliency and energy absorption for the track. Moreover, voids provide drainage of water in the track. However, the voids in the ballast will eventually be filled with fouling material and thus the ballast will need to be cleaned or replaced.

Similar to ballast, subballast is also a granular material but is generally finer and more broadly-graded than ballast. The subballast further reduces the stress levels on the subgrade and prevents the upward migration of fine material from the subgrade into the ballast. Subgrade is the foundation for the track structure and can be existing natural soil or placed soil. As with all foundations, excessive settlement should be avoided.

2.2.2. Track forces

Forces in the vertical, lateral, and longitudinal directions act on the track structure. These forces can be due to moving traffic and changing temperature.

The longitudinal force is usually due to acceleration and braking of trains and thermal expansion or contraction of the rails. The lateral force usually comes from the lateral wheel force due to the friction between the rail and wheel especially when a train goes round corners. It also comes from the buckling reaction force of the rail which is usually caused by a high longitudinal force in the rail.

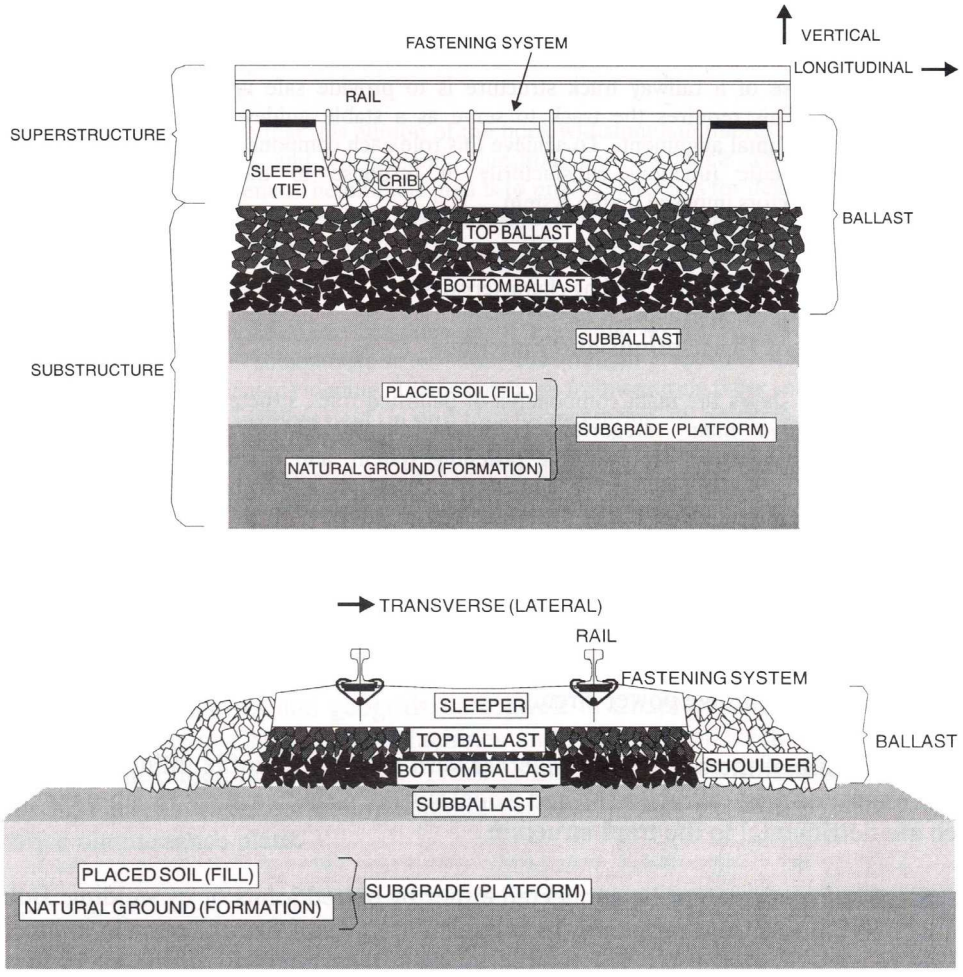

Figure 2.1. Layout of a typical ballasted track (Selig and Waters, 1994)

The vertical force can be subdivided into the downward and upward force. In reaction to the downward force, the upward force is induced by the rail as

shown in Figure 2.2. The downward force is a combination of a static load and a dynamic component. The static component is the weight of the train while the dynamic component is a function of track conditions, train characteristics, operating conditions, train speed, and environmental conditions. It is the dynamic component that usually causes an adverse effect to the track as it can be much larger than the static load. According to Selig and Waters (1994), the magnitude of the dynamic component can be up to 2.4 times the static load.

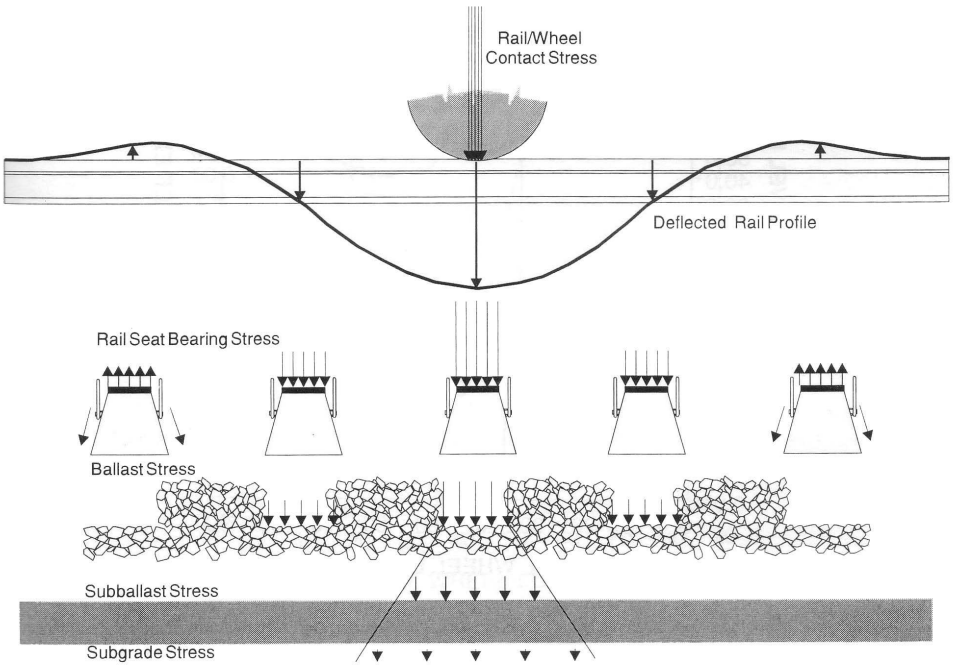

Figure 2.2. Typical wheel load distribution into the track structure (Selig and Waters, 1994)

2.2.3. Track geometry maintenance

Settlement occurs in a railway subjected to long-term traffic loading. In the UK, normal maintenance intervals for main line and branch line tracks are one to two years and three to four years, respectively. There are two methods of

track geometry maintenance; tamping and stoneblowing. Tamping is used to correct long wavelength faults caused by repeated traffic (Selig and Waters, 1994). The tamping wagon, shown in Figure 2.3, contains several tamping tines as shown in Figure 2.4.

Figure 2.3. Self-propelled tamping machine (Selig and Waters, 1994)

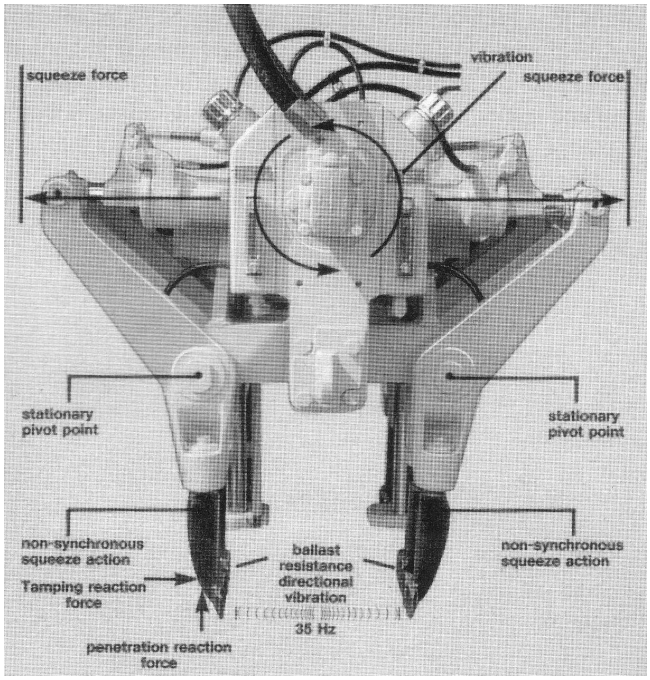

Figure 2.4. Tamping tines (Selig and Waters, 1994)

Figure 2.5 shows the operating sequence of the tamping machine, where:

(A) The track and sleeper are in an arbitrary position before tamping begins.

(B) The track and sleeper are raised by the machine to the target level. As a result, there is an empty space under the sleeper.

(C) The tamping tines are inserted into the ballast on both sides of the sleeper. This step can cause ballast breakage.

(D) The tamping tines squeeze the ballast into the empty space under the sleeper. Therefore, the correct position of the rail and sleeper is recovered. This might also cause ballast breakage.

(E) The tamping tines are lifted from the ballast. They will then move on to tamp around the next sleeper.

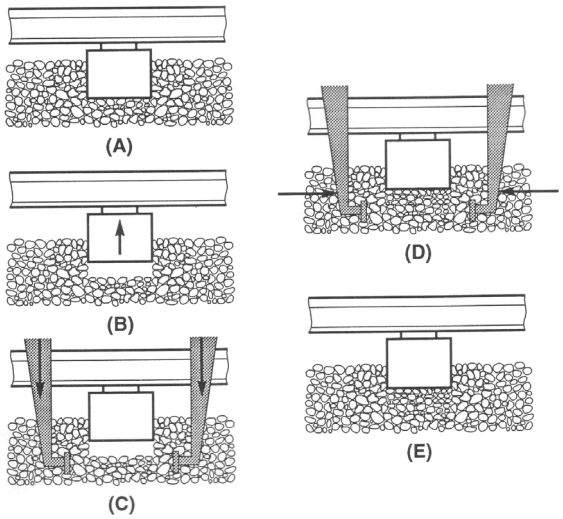

Figure 2.5. Tamping sequence (Selig and Waters, 1994)

Ballast should be pushed into the void under the sleepers to support the sleepers at the required profile. However, the ballast will soon return to its pre-maintenance profile. This phenomenon is called “ballast memory” and is shown in Figure 2.6. The tamping process disturbs and dilates the compacted ballast. Therefore, the ballast that fills the space under the sleeper is loose and hence under trafficking, the settlement increases at a faster rate and the ballast will soon return to its previous compacted profile.

The ballast memory effect can be reduced by changing the amount of sleeper lift (Selig and Waters, 1994). Figure 2.7 shows a plot between the sleeper lift given by the tamper and the settlement in the subsequent 66 weeks of trafficking. It can be seen that for relatively small lifts, the settlement is approximately equal to the lift. Therefore, there is no lasting change in the inherent track shape. On the other hand, the settlement corresponding to the higher lifts are not as large as the lift i.e. this indicates more lasting improvement in the inherent track shape. Selig and Waters (1994) define a high lift as a lift which exceeds the D_{50} size of the ballast, i.e. the sieve size that will retain 50% of a representative sample of the ballast.

According to Selig and Waters (1994), the tamping tines squeeze the ballast which in turn expands upwards to fill the void for low lifts. On the other hand, high lifts allow maximum dilation to occur as the squeezed ballast expands upwards, additional ballast particles will also be added to the ballast skeleton underneath the sleeper as there is now sufficient room for them. The new

ballast skeleton will then be compacted by the subsequent traffic loading and will adopt a new geometry.

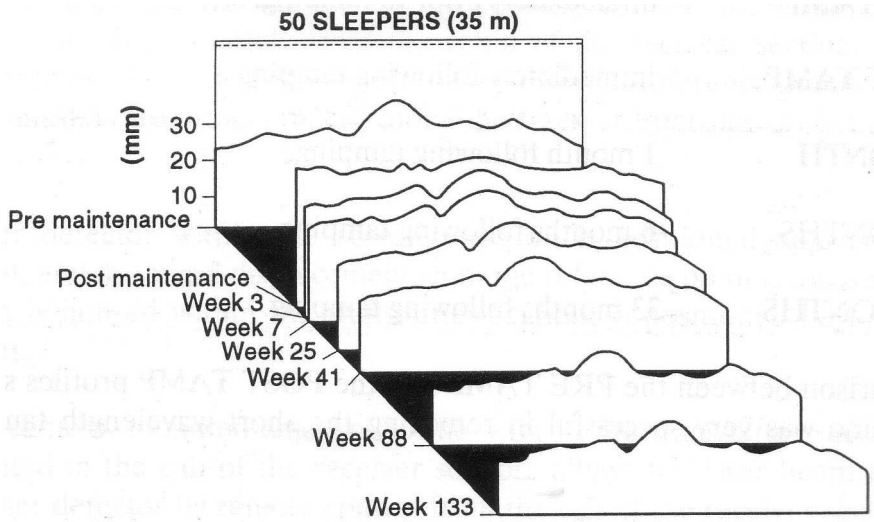

Figure 2.6. Effect of ballast memory (Selig and Waters, 1994)

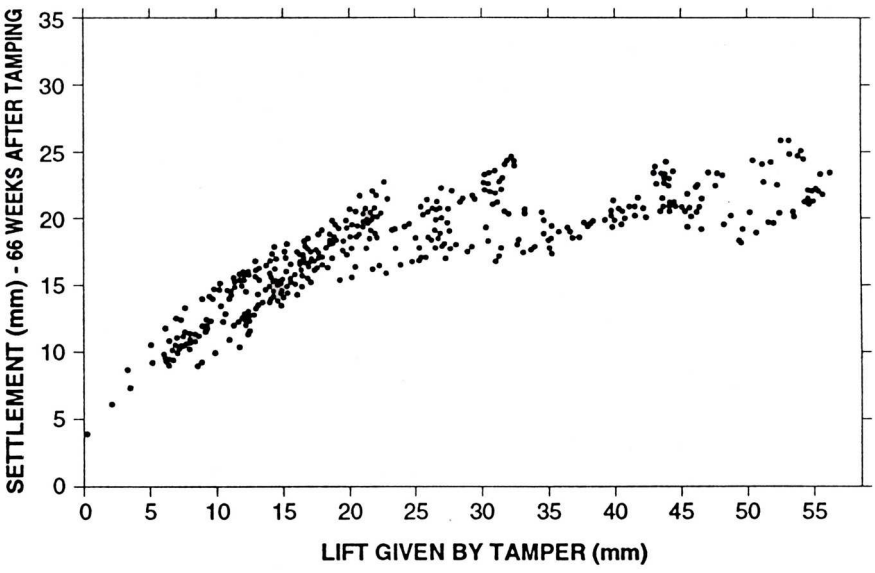

Figure 2.7. Sleeper settlement as a function of tamping lift (Selig and Waters, 1994)

For short wavelength geometric faults, the stoneblowing maintenance is more suitable (Selig and Waters, 1994). According to the current normal practice in

the UK, stoneblowing is used only on the section of track with high tamping frequency as it causes less damage to the ballast. Test results of Wright (1983) showed that both tamping and stoneblowing caused ballast breakage during the insertion into the ballast layer. However, stoneblowing produced up to eight times fewer particles smaller than 14 mm than tamping. A stoneblowing wagon is shown in Figure 2.8.

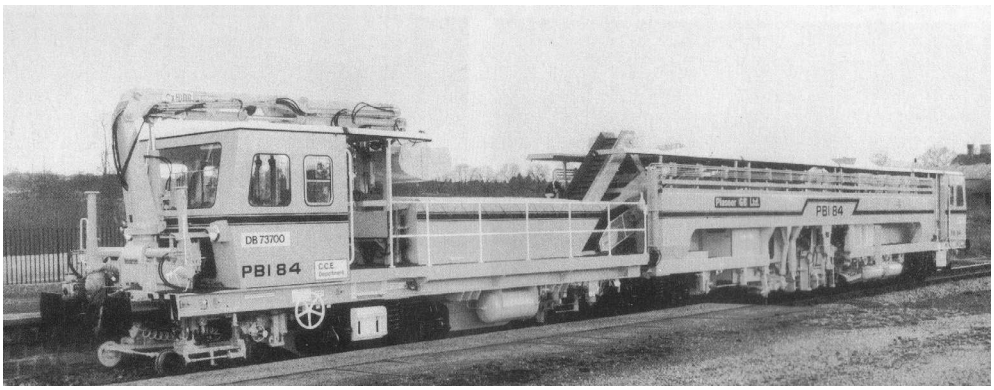

Figure 2.8. Stoneblowing wagon (Selig and Waters, 1994)

The operating sequence of stoneblowing maintenance is shown in Figure 2.9, where:

(A) The track and sleeper are in an arbitrary position before tamping begins.

(B) The track and sleeper are raised by the machine to the target level. As a result, there is an empty space under the sleeper.

(C) The stoneblowing tubes are inserted into the ballast layer.

(D) A measured quantity of stone is blown by compressed air into the space between the sleeper and the ballast.

(E) The tubes are withdrawn from the ballast layer.

(F) The sleeper is lowered onto the top of the blown stone which will be compacted by subsequent traffic.

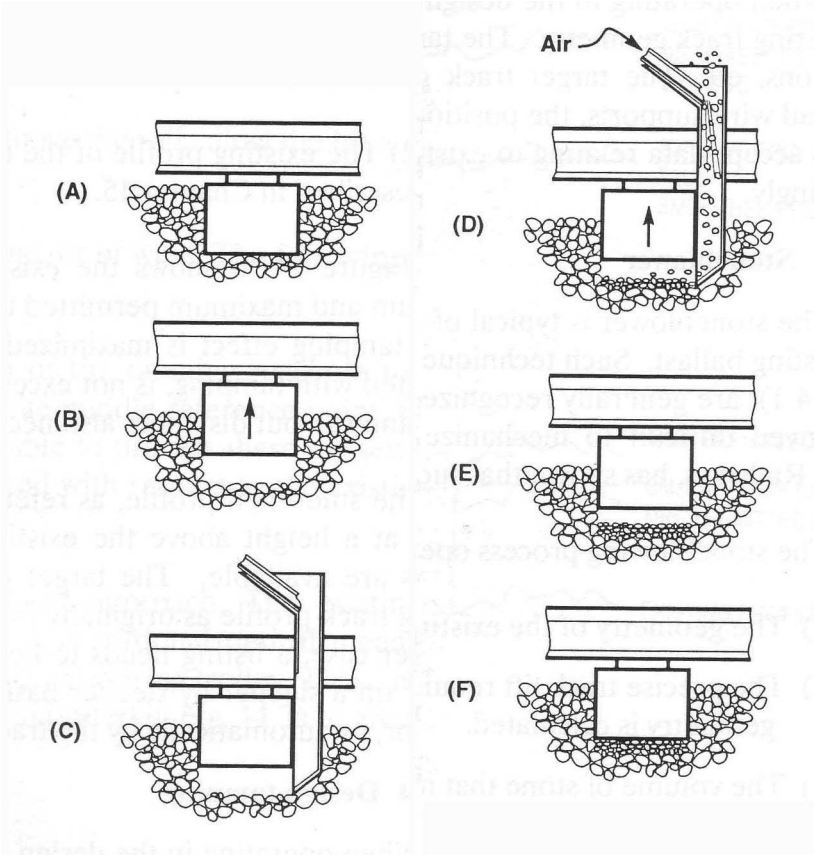

Figure 2.9. The stoneblowing process (Selig and Waters, 1994)

2.3. Ballast

2.3.1. Ballast specification and testing

To ensure that ballast is of good quality, ballast needs to be tested after the manufacturing process at the quarry. Railway engineers are mainly interested in mechanical and dimensional properties. RT/CE/S/006 Issue 3 (2000) specifies the recommended properties of ballast to be used from the 1st April 2005. It follows the European railway ballast specification BS EN 13450 (2002). This specification focuses on five ballast properties: ballast grading,

Los Angeles Abrasion (LAA) value, micro-Deval attrition (MDA) value, flakiness index, and particle length. The specification requires ballast to conform the particle size distribution shown in Figure 2.10.

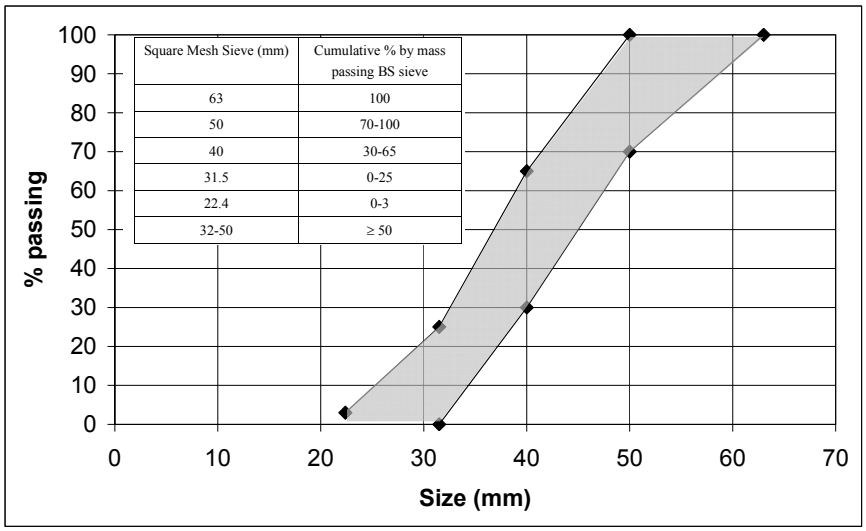

Figure 2.10. Specification for ballast particle size distribution (RT/CE/S/006 Issue 3, 2000)

The procedure of the LAA test is described in BS EN 1097-2 (1998). This procedure is modified by Annex C of BS EN 13450 (2002) to suit the size of ballast as the usual test sample for the LAA test is 10 – 14 mm i.e. much smaller than the ballast. The test involves rotating five kilograms of 31.5 – 40 mm ballast and five kilograms of 40 – 50 mm ballast with twelve spherical steel balls weighing 5.2 kilograms in total in a steel drum. The drum rotates on a horizontal axis at 31 to 33 revolutions per minute for 1,000 revolutions. The LAA value is the percentage by mass of particles passing 1.6 mm sieve after the test. The specification requires the LAA values to be below or equal to 20 %.

The micro-Deval test is carried out as specified in BS EN 1097-1 (1996) with modification specified in Annex E of BS EN 13450 (2002). This test involves rotating five kilograms of 31.5 – 40 mm ballast and five kilograms of 40 – 50 mm ballast with two litres of water in a steel drum. The drum rotates at 100 revolutions per minute for 14,000 revolutions. The MDA value is the percentage by mass of particles passing 1.6 mm sieve after the test. The specification limits the MDA value to 7 %.

BS EN 933-3 (1997) describes a procedure of the flakiness index test. The test consists of two sieving operations. The first operation is to sieve the test sample into various particle size fractions. The second is to sieve each fraction by bar sieves with parallel slots. The width of each slot is half the larger sieve size of each fraction. The flakiness is the percentage by mass of the particles passing the bar sieves. The specification limits the flakiness index to 35 %.

The particle length index test is performed by measuring each ballast particle from a ballast sample of mass exceeding 40 kg with a gauge or callipers. The length index is the percentage by mass of ballast particles with length larger than or equal to 100 mm. The specification requires the particle length index to be less than or equal to 4 %.

2.3.2. Ballast fouling

After long term service, ballast becomes damaged and contaminated and its gradation changes. As a result, its performance reduces. This process is called

"fouling". According to Selig and Waters (1994), there are five causes of ballast fouling. They are:

- Ballast breakdown
- Infiltration from ballast surface
- Sleeper wear
- Infiltration from underlying granular layers
- Subgrade infiltration

Table 2.1 shows the percentage of fouling component according to the estimates of British Railways. According to the table, the biggest source of fouling is external. British Railways has also found that after removing the fouling material, ballast particles are still in good working condition after 15 years of service. This agrees with the estimates in the table that ballast breakdown is not the main source of fouling. On the contrary, the main source of ballast fouling in North America is ballast breakdown as shown in Figure 2.11.

Ballast fouling prevents ballast from fulfilling its functions. The effect of ballast fouling depends on the size and amount of ballast fouling. As the mass of sand and fine-gravel-sized fouling particles (0.075 – 19 mm) increases, the resiliency to vertical deformation of the ballast and void space decreases. This makes surface and lining operations more difficult and drainage decreases. As the voids become filled or nearly filled, ballast becomes denser and tamping then loosens the ballast. This will lead to a higher rate of ballast settlement after tamping.

No.	Source	Degradation	
		kg/sleeper	% of total
1	Delivered with ballast (2 %)	29	7
2	Tamping: 7 insertions during renewal and 1 tamp/yr for 15 years at 4 kg/tamp	88	20
3	Attrition from various causes including traffic and concrete sleeper wear (Traffic loading: 0.2 kg/sleeper/million tons of traffic)	90	21
4	External input at 15 kg/yr (Wagon spillage: 4.0 kg/m^2/yr) (Airborne dirt: 0.8 kg/m^2/yr)	225	52
	Total	432	100

Table 2.1. British railways sources of fouling (Selig and Waters, 1994)

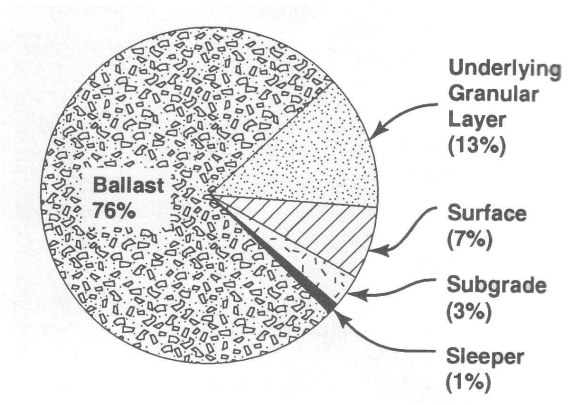

Figure 2.11. Sources of ballast fouling from all sites in North America (Selig and Waters, 1994)

An increase in the mass of clay and silt-sized fouling particles (smaller than 0.075 mm) also reduces drainage which then leads to erosion of ballast and subgrade attrition. Fine particles can also combine with water to form an abrasive slurry. Also, if the content of clay- and silt-sized fouling particles is high, it is difficult for the tamping machine to penetrate and rearrange the ballast.

Different researchers proposed different ballast fouling indices to quantify the foulness of the ballast, shown in Table 2.2.

Fouling index			Classification
$F_I = P_{0.075} + P_{4.75}$ (Selig and Waters, 1994)	$FI_P = P_{0.075} + P_{13.2}$ (Ionescu, 2004)	$FI_D = D_{90} / D_{10}$ (Ionescu, 2004)	
< 1	< 2	< 2.1 and $P_{13.2} \leq 1.5$ %	Clean
1 to < 10	2 to < 10	2.1 to < 4	Moderately clean
10 to < 20	10 to < 20	4 to < 9.5	Moderately fouled
20 to < 40	20 to < 40	9.5 < 40	Fouled
≥ 40	≥ 45	≥ 40, $P_{13.2} \geq 40$ %, $P_{0.075} > 5$ %	Highly fouled
P_x = Percentage passing at x mm / 100 D_y = Particle size at y percentage passing (mm)			

Table 2.2. Fouling indices

Selig and Waters' fouling index (F_I) is used to quantify the foulness of ballast in North America. Ionescu (2004) proposed FI_P as a modification of Selig and Waters' fouling index to suit the condition of the ballast in Australia and FI_D as the field sample in the study showed little variation in D_{90} but a large variation in D_{10}.

In the UK practice, ballast becomes fully fouled when there are about 30 % by weight of particles smaller than 14 mm in the ballast (Selig and Waters, 1994) and ballast is regarded as acceptable if:

1. It retains the geometry such that only a normal level of maintenance is needed (i.e. annual or bi-annual tamping/stone blowing).
2. There are few wet spots, i.e. track sections with trapped water, or the wet spots that exist can be traced to factors other than the ballast.

Even if both criteria are present, the ballast condition is however not acceptable if greater than 30 % of particles smaller than 14 mm are found in the track.

2.4. Particle breakage

2.4.1. Griffith theory

Griffith crack theory is widely used by many materials scientists and engineers to explain and determine the fracture behaviour of solids. Examples of solids containing flaws or cracks are ceramics, glasses, and rocks. When a stress is intensified at a crack, the material will have a little plasticity to resist the crack propagation and fail by fast fracture. According to Griffith theory, the fast fracture criterion is given by the following equation:

$$\sigma\sqrt{\pi a} = \sqrt{EG_C} \qquad (2.1)$$

where σ = applied stress

a = crack length

E = Young's modulus

G_C = Toughness

Toughness (G_C) is the energy required to generate a unit area of crack. Its unit is energy per unit area i.e. J/m^2 and is a material property. From the left hand side of the equation, the fast fracture can occur when either;

a. A crack grows and reaches the critical size a when a material is under stress σ, or

b. A material with a crack of length a is under a stress which increases to the critical stress σ.

The right hand side of the equation is dependent on material properties only. The constant on the right side of the equation is defined as the fracture toughness or K_{IC} ($K_{IC} = \sqrt{EG_C}$). The term in the left hand side of the equation is normally known as the "stress intensity factor" or K ($K = \sigma\sqrt{\pi a}$). Therefore, the critical combination of the stress and the crack length must reach a certain value in order for a fast fracture to occur. In other words, fast fracture will occur when $K = K_{IC}$.

2.4.2. Single particle under compression and Weibull statistics

McDowell and Amon (2000) defined an induced stress (σ) of a particle of size d loaded between two flat platens under a force F as:

$$\sigma = \frac{F}{d^2} \tag{2.2}$$

The strength of a particle can be taken as the force at failure divided by the square size of the particle at failure i.e. the distance between the platens at failure.

Griffith theory states that failure of a brittle solid is caused by the propagation of one or more cracks. Hence, the strength of a ballast particle depends on the size and distribution of cracks and flaws in it. Different particles have different sizes and distributions of crack sizes even though they look alike. Therefore, statistical analysis is necessary to determine the distribution of strengths of ballast particles.

According to Hertzberg (1996), Weibull statistics (Weibull, 1951) gives a more accurate characterisation of property values for brittle materials than the normal distribution. Figure 2.12 shows the difference between the normal probability density function (p.d.f.) and Weibull p.d.f. for the same mean and standard deviation (McDowell, 2001). The value of m in the figure is the Weibull modulus which will be explained below. As the Weibull modulus increases, the similarity between the normal p.d.f. and Weibull p.d.f. increases.

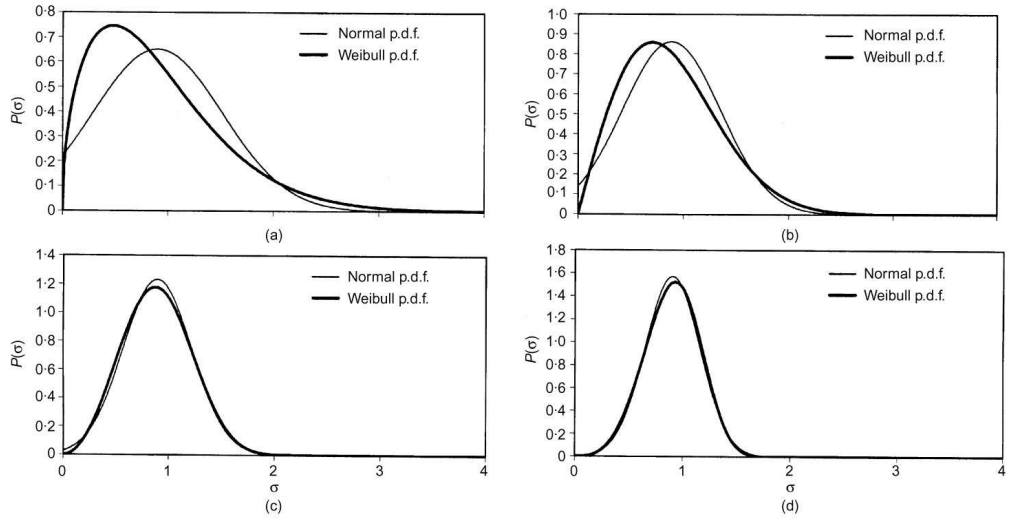

Figure 2.12. Weibull p.d.f. and normal p.d.f with same mean and standard deviation (a) m = 1.5, (b) m = 2, (c) m = 3, (d) m = 4 (McDowell, 2001)

According to McDowell and Amon (2000), a particle of size d loaded between two flat platens under an induced tensile stress σ has a survival probability ($P_s(d)$) given by

$$P_s(d) = \exp\left[-\left(\frac{d}{d_0}\right)^3\left(\frac{\sigma}{\sigma_o}\right)^m\right] = \exp\left[-\left(\frac{\sigma}{\sigma_{o,d}}\right)^m\right] \quad (2.3)$$

where

d_o = Reference particle size

σ_o = Characteristic stress at which 37 % of particles of size d_o survive

$\sigma_{o,d}$ = Characteristic stress at which 37 % of particles of size d survive

m = Weibull modulus

The Weibull modulus (m) decreases with increasing variability in strength. (Ashby and Jones, 1998; McDowell and Bolton, 1998). Figure 2.13 shows the variability in strength for different Weibull modulus. McDowell (2001) showed that m relates to the coefficient of variation (standard deviation / mean).

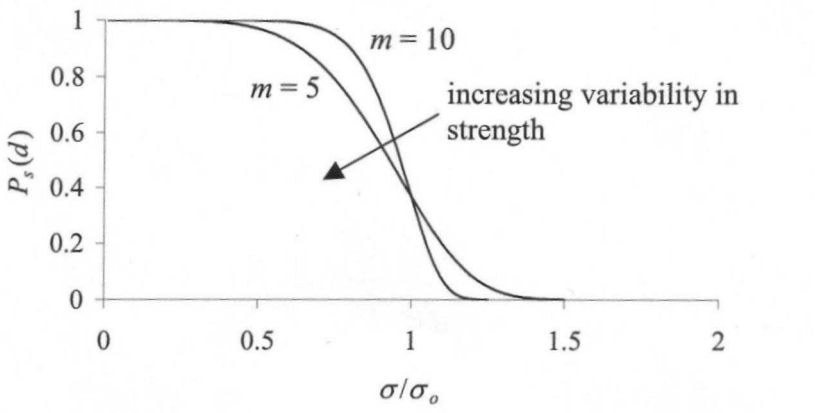

Figure 2.13. Weibull distribution of strengths (Ashby and Jones, 1998)

McDowell and Amon (2000) derived an equation defining average tensile strength (σ_{av}) for particles of size d as shown in Equation 2.4.

$$\sigma_{av} = \Gamma(1+1/m)\sigma_{o,d} \qquad (2.4)$$

Γ is the Gamma function and can be calculated by using GAMMALN and EXP functions in Microsoft Excel or can be found in standard statistics texts. It can be seen that the average tensile strength is proportional to $\sigma_{o,d}$. The value of the gamma function is approximately 1 for a wide range of Weibull modulus values. Therefore, it can also be said that the average tensile strength is

approximately equal to $\sigma_{o,d}$. Moreover, it can be inferred from Equations 2.3 and 2.4 that

$$\sigma_{av} \propto \sigma_{o,d} \propto d^{-3/m} \qquad (2.5)$$

The above equation shows that there is a size effect in single particle crushing tests, i.e. the larger the particle, the lower the strength. It can also be seen that m determines the size effect on σ_o and hence, on σ_{av}. The size effect is small in a material with small variability since m is large.

McDowell and Amon (2000) performed single particle crushing tests on Quiou sand grains of different sizes. The results are shown in Table 2.3 and Figure 2.14. The average Weibull modulus from the table is 1.51. According to the plot in Figure 2.14, -3/m is –1.9647 therefore m is 1.53. This proves that Equation 2.5 is correct for this material.

Nominal size /mm	Average size at failure /mm	Weibull modulus m	37% tensile strength /MPa
1	0.83	1.32	109.3
2	1.72	1.51	41.4
4	3.87	1.16	4.2
8	7.86	1.65	0.73
16	15.51	1.93	0.61

Table 2.3. Weibull modulus and 37% strength for each grain size (McDowell and Amon, 2000)

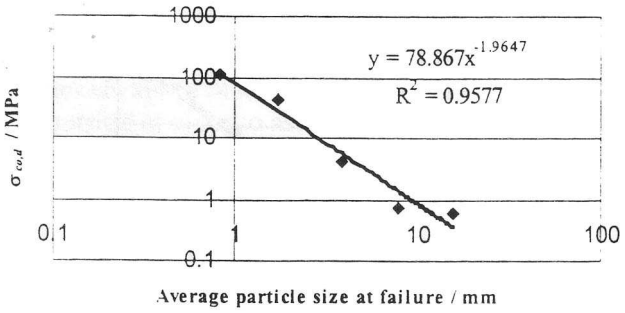

Figure 2.14. 37 % strength against average particle size at failure (McDowell and Amon, 2000)

A sufficient number of tests is necessary for obtaining the mean strength and standard deviation to within a degree of acceptable accuracy. According to McDowell (2001), for a population Weibull modulus of 1.5, the sample mean strength can only be determined to with about 25% of the true mean at 95% confidence level with thirty test particles.

2.4.3. Particle breakage in aggregate

According to McDowell et al. (1996), the probability of particle breakage in an aggregate increases with an increase in applied macroscopic stress, increase in particle size, and reduction in coordination number (number of contacts with neighbouring particles).

According to the size effect, the larger the particle, the lower its strength. Therefore, the probability of particle breakage increases with an increase in particle size. A high coordination number can reduce the induced tensile stress in a particle. This is because loads are distributed through many contact points

on the particle surface and hence reducing the induced tensile stress. However, this also depends on the shape of the particles as shown in Figure 2.15.

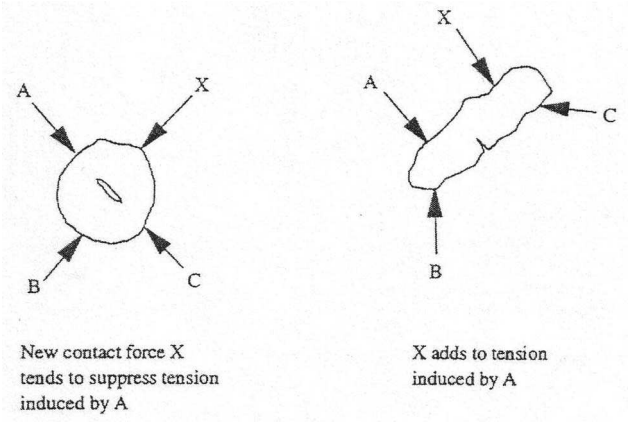

Figure 2.15. Large coordination numbers are less helpful for more angular particles (McDowell et al., 1996)

Therefore, the size and coordination number are two opposing effects on particle survival. Smaller particles are stronger but have fewer contacts than larger particles and vice-versa. If the size effect dominates over the effect of coordination number, large particles are more likely to break, meaning, a uniform matrix of fine particles will be left at the end of any one-dimensional compression test. However, no evidence of this has been found. On the other hand, if the effect of coordination number dominates over the size effect, the small particles are more likely to break. Hence, a distribution of particle sizes evolves, such that some of the initial large particles remain, protected by the many finer particles produced. An example of this behaviour is shown in Figure 2.16. The figure shows the evolution of particle size for Ottawa sand in one-dimensional compression tests under increasing macroscopic stress.

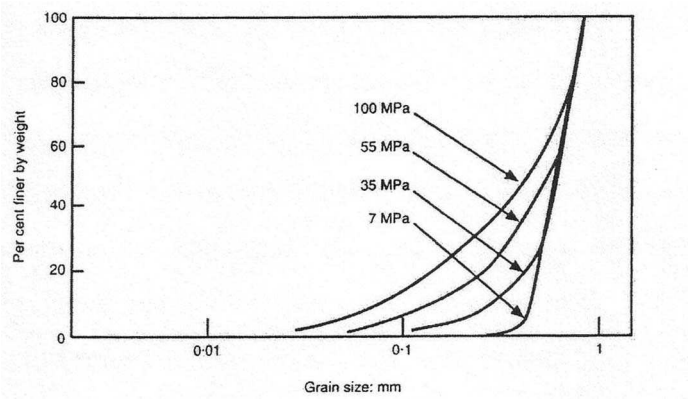

Figure 2.16. Evolving particle size distribution curves for one-dimensionally compressed Ottawa sand (Fukumoto, 1992)

Oda (1977) studied the coordination number in different assemblies of glass balls. He found that as voids ratio decreased, the average coordination number increased as shown in Figure 2.17. He also concluded that this behaviour was independent of the grain size distribution.

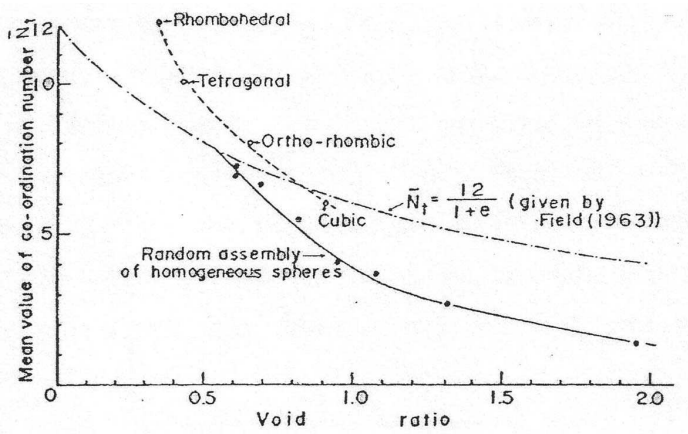

Figure 2.17. Relationship between mean coordination number and voids ratio (Oda, 1977)

2.5. Behaviour of aggregate under monotonic loading

The typical behaviour of granular materials subject to one-dimensional compression is shown by the plot of voids ratio against the logarithm of vertical effective stress in Figure 2.18.

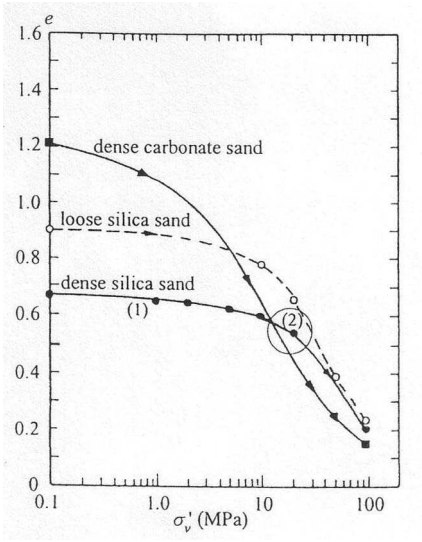

Figure 2.18. One-dimensional compression plots for carbonate and silica sands (Golightly, 1990)

The behaviour in region 1 of the dense silica sand is quasi-elastic with some irrecoverable deformation due to particle rearrangement. The sand yields in region 2 where the behaviour is plastic and forms a straight line beyond region 2, known as the normal compression line. Since the material has undergone all possible rearrangement at the end of region 1, particle breakage must then occur to achieve further compaction. It is clear that all particles are not loaded in the same direction or orientation. However, it can be assumed that many particles will eventually be in the paths of the columns of strong force that carry the applied macroscopic stress. Cundall and Strack (1979) studied the

paths of strong force using discrete element simulations as shown in Figure 2.19.

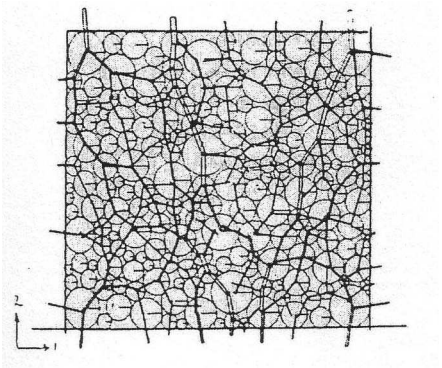

Figure 2.19. Discrete element simulation of an array of photoelastic discs $F_H/F_V = 0.43$ (Cundall and Strack, 1979)

The columns of strong force change as breakage and/or rearrangement of particles occur. The loading geometry of the particles in the force columns is similar to the loading geometry of the single particle crushing test (i.e. a particle is loaded between two flat platens) but there are also some smaller force chains in other directions acting on the particles from the neighbouring particles. McDowell and Bolton (1998) suggested that the yield stress must be proportional to the average tensile strength of particles and defined yield stress as macroscopic stress that causes the maximum rate of grain fracture under increasing stress. McDowell (2002) analysed single particle crushing tests on various grain sizes of Leighton Buzzard sand and one-dimensional compression tests on the same type of sand of various uniform gradings. Figure 2.20 shows the one-dimensional compression test results. It can be seen that the larger the grain size, the smaller the yield stress. From Figure 2.19, McDowell (2002) noted that the array is approximately 12 particles wide and

approximately three columns of strong force are formed to pass on the stress. Hence, the stress induced in the particles in the paths of the strong force should be approximately four times the macroscopic stress. He then predicted that the yield stress equalled ¼ of 37% tensile strength of the grain (σ_o). The comparison of the predicted and true yield stress found in one-dimensional compression tests is shown in Figure 2.21.

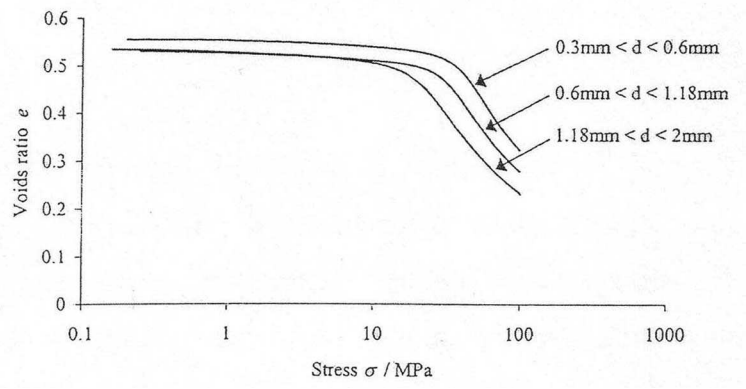

Figure 2.20. Compression plots for different uniform gradings of sand (McDowell, 2002)

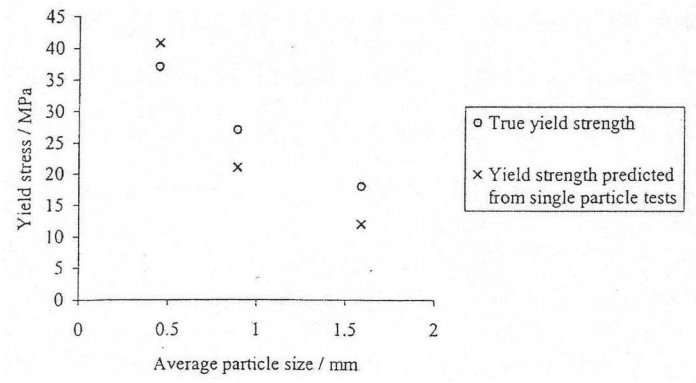

Figure 2.21. Yield stress predicted from single particle crushing tests, assuming yield stress = (37% tensile strength)/4 (McDowell, 2002)

It can be seen from Figure 2.21 that the prediction gives a good approximation of yield stress. This also confirms the suggestion by McDowell and Bolton (1998) that yield stress should be proportional to the average tensile strength of the constituent particles.

2.6. Behaviour of aggregate under cyclic loading

2.6.1. Resilient behaviour

Under cyclic loading, the deformation of granular materials is divided into resilient deformation and permanent deformation. Figure 2.22 (Lekarp et al., 2000a) shows the stress-strain curve of granular material during one cycle.

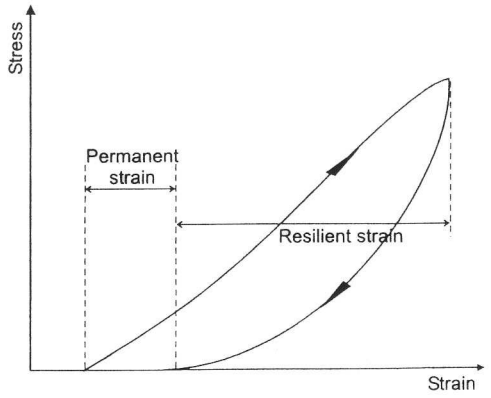

Figure 2.22. Strains in granular materials during one cycle of load application (Lekarp et al., 2000a)

The resilient behaviour of granular material is characterised by the resilient modulus (M_r) and Poisson's ratio (ν) defined in Equations 2.6 and 2.7.

$$M_r = \frac{\Delta(\sigma_1 - \sigma_3)}{\varepsilon_{1,r}} \tag{2.6}$$

$$\upsilon = -\frac{\varepsilon_{3,r}}{\varepsilon_{1,r}} \tag{2.7}$$

where σ_1 = Major principal stress (axial stress)

σ_3 = Minor principal stress (horizontal stress)

$\varepsilon_{1,r}$ = Resilient axial strain

$\varepsilon_{3,r}$ = Resilient horizontal strain

Under the same repeated load, the resilient strains become approximately constant after a certain number of load cycles. Hence, the resilient modulus will also become approximately constant.

Both resilient and plastic behaviour of granular material under cyclic loading are normally studied using cyclic triaxial testing. According to Lekarp et al. (2000a) the resilient behaviour of granular material is affected by many factors such as:

- Stress level
- Density
- Maximum grain size
- Grading
- Fines content
- Moisture content
- Stress history
- Number of load cycles
- Aggregate type
- Particle shape
- Load duration
- Loading frequency
- Load sequence

The effect of each parameter will now be discussed.

2.6.1.1.Effect of stress level

According to Lekarp et al. (2000a), many researchers accepted that stress level had the most significant effect on the resilient behaviour of granular materials. Monismith et al. (1967) and Uzan (1985) both found that the resilient modulus increased considerably with confining pressure. On the other hand, the resilient modulus is affected to a much smaller extent by the magnitude of deviatoric stress. Uzan (1985) stated that the resilient modulus slightly decreased as the deviatoric stress increased. Meanwhile, Hicks and Monismith (1971) found that resilient modulus slightly increased with the deviatoric stress. Ping and Yang (1998) concluded that the resilient modulus of Panama sand either did not change, or slightly increased with the deviatoric stress but found the opposite result on Alachua sand.

Very few studies have concentrated on characterisation of Poisson's ratio compared to the resilient modulus (Lekarp et al., 2000a). However, some researchers found that the effect of the stress level on the value of Poisson's ratio is the opposite to the resilient modulus. Hicks and Monismith (1971) and Brown and Hyde (1975) both showed that the Poisson's ratio increased with decreasing confining pressure and increasing deviatoric stress.

Granular materials in pavements are normally subjected to a variety of cyclic principal stresses as a result of moving traffic. Therefore, it is reasonable to mutually cycle both the axial and confining stresses in a triaxial test. However,

Brown and Hyde (1975) suggested that it was not necessary to cycle both axial and confining stresses as they obtained similar values of resilient modulus from cyclic and constant confining stress when the constant stress was equal to the mean of the cyclic value.

Since applied stress level has the most significant effect on resilient modulus, it is therefore necessary to model it as correctly as possible. According to the review of Lekarp et al. (2000a), many researchers have been developing the resilient modulus model based on curve fitting procedure of the results from their experiments. Even though it has been generally agreed that the effect of deviatoric stress is not as pronounced as the confining stress, some researchers found that the effect of deviatoric stress should be included in the model as shown in Equation 2.8. The equation however contradicts the findings of Hick and Monismith (1971) and Ping and Yang (1998) who said that the resilient modulus slightly increased with the deviatoric stress.

$$M_r = k_1 \left(\frac{p}{q} \right)^{k_2} \qquad (2.8)$$

where M_r = Resilient modulus

k_1 and k_2 = Empirical constants

p = Mean principal stress

q = Deviatoric stress

However, the simplest model which is widely accepted for analysis of stress dependence of material stiffness is commonly known as the K-θ model as

shown in Equation 2.9 where θ is the sum of principle stresses. Furthermore, this model is also used with the triaxial test results in this project (see Section 5.7.3).

$$M_r = k_1 \theta^{k_2} \tag{2.9}$$

2.6.1.2.Effect of density

According to the experiments of Thom and Brown (1988), density has almost no influence on the properties of the aggregate. However, Hicks and Monismith (1971) and Kolisoja (1997) found that the resilient modulus increased with increasing density. This might be because an increase in density results in an increase in the co-ordination number (the average number of contacts per particle) and a decrease in the average contact stress between particles. This then leads to a decrease in the total deformation and, hence, an increase in resilient modulus.

Hicks and Monismith (1971) concluded from their experiments that the effect of density was more significant in partially crushed gravel than crushed rock. The particle size distributions of both aggregate are shown in Figure 2.23. The resilient modulus was found to increase with the relative density in partially crushed gravel. The effect of the density on the resilient modulus in fully crushed rock was negligible. This is probably because the partially crushed gravel is less angular than the crushed rock.

Unlike the behaviour of granular materials under monotonic loading where density plays an important role, it can be seen from the above findings that the effect of density of the resilient properties of granular material is still unclear. This agrees with the conclusion from Lekarp et al. (2000a).

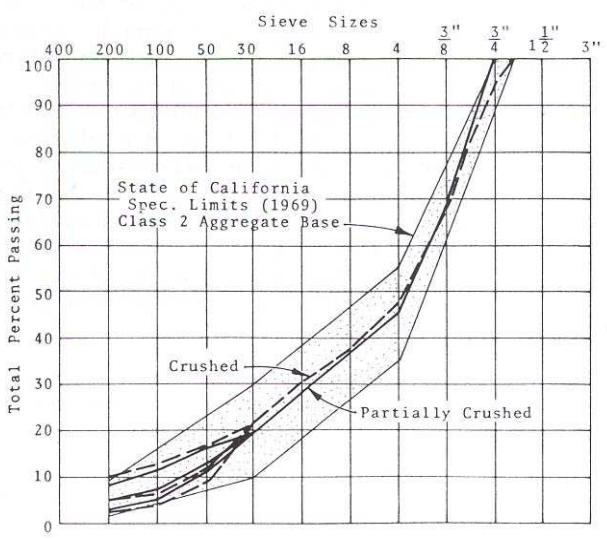

Figure 2.23. Partially crushed gravel and crushed rock in Hicks and Monismith (1971)

2.6.1.3.Effect of maximum particle size, grading, and fines content

For aggregates with the same amount of fines and similar particle size distribution, the resilient modulus increases with the maximum particle size. Kolisoja (1997) explained that the load was transmitted through fewer particles in the aggregates with larger material grains. This leads to smaller deformation between the particles and hence an increase in the resilient modulus.

The grading of granular materials has a minor effect on resilient modulus. Thom and Brown (1988) found that for aggregates with the same maximum

particle size, uniformly graded aggregate had slightly larger resilient modulus than well graded aggregate. Heydinger et al. (1996) also found that the poorly-graded limestone showed higher resilient modulus than the well-graded one.

According to Lekarp et al. (2000a), the effect of the fines content on the resilient modulus is still unclear. According to Hicks and Monismith (1971), the influence of amount of particles passing 0.075 mm sieve (sieve number 200) was not very well defined as shown in Figure 2.24.

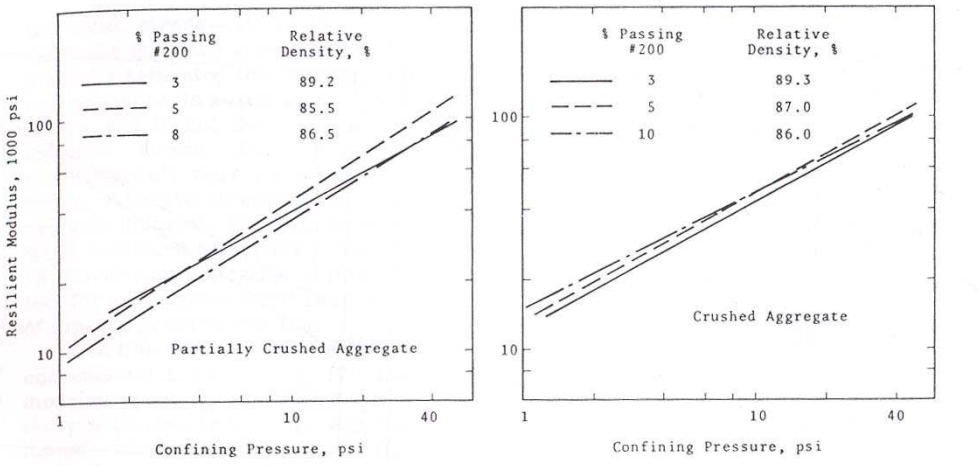

Figure 2.24. Effect of particles passing 0.075 mm sieve (sieve number 200) on resilient modulus (Hicks and Monismith, 1971)

2.6.1.4.Effect of moisture content

According to the literature review of Lekarp et al. (2000a), the resilient behaviours of dry and most partially saturated granular materials are similar. But as complete saturation is approached, the resilient behaviours are significantly affected. Many researchers, such as Hicks and Monismith (1971), Ping and Yang (1998), and Heydinger et al. (1996), agreed that the resilient

modulus decreases with increasing saturation level because excess pore-water pressure is developed under repeated loading. The effective stress in the material decreases as the pore-water pressure is developed. As a result, the strength, stiffness, and hence resilient modulus decreases.

2.6.1.5.Effect of stress history and number of load cycles

The effect of stress history is mainly compaction, rearrangement and breakage of particles. The previous number of load cycles also affects the resilient behaviour. To eliminate the effect of stress history, Hicks and Monismith (1971) suggested that specimens should be loaded for 1,000 cycles prior to repeated load resilient test to condition them into the same level of compaction. However, Brown and Hyde (1975) concluded that the resilient properties of granular materials were unaffected by stress history provided that the applied stress did not cause failure.

With increasing number of load applications, the material gets stiffer and hence, the resilient modulus increases. However, after a certain number of load applications, it becomes approximately constant. According to the triaxial tests on railway ballast of Shenton (1974) where applied maximum deviatoric stress levels were closed to the failure level, the resilient modulus increased rapidly during the first 10 cycles and became approximately constant after 100 cycles. Similarly, Hicks and Monismith (1971) reported that the resilient modulus of partially crushed gravel and crushed rock becomes constant after 50 to 100 load cycles provided that the ratio between maximum axial stress and confining stress does not exceed 6 or 7.

Collins and Boulbibane (2000) explained the concept of shakedown in four stages as shown in Figure 2.25. At first, when the cyclic loading is sufficiently small, there are no permanent strains. If the load then exceeds the elastic load, the permanent strains will be induced (Stage 2 in Figure 2.25). After the finite number of cycles, the behaviour becomes purely elastic, i.e. no further permanent strain. At this point, the material structure is said to have "shakedown" and the resilient strain becomes constant resulting in constant resilient modulus.

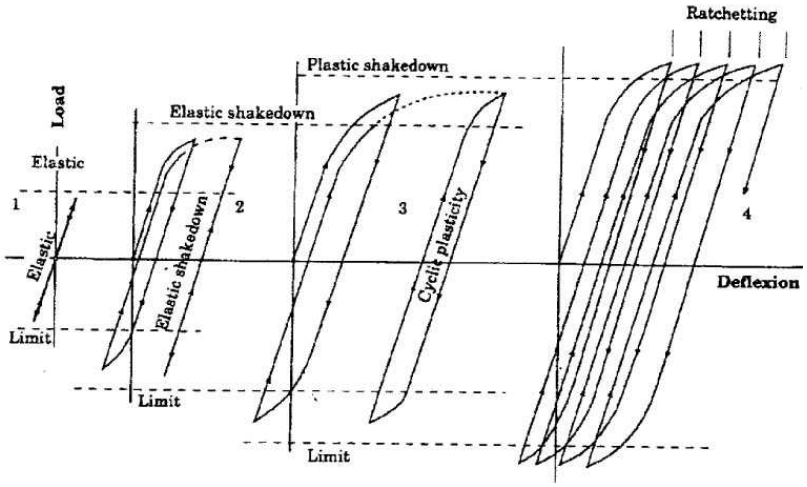

Figure 2.25. Four types of response of elastic/plastic structure to repeated loading cycles (Collins and Boulbibane, 2000)

At higher loads, shakedown does not occur and the behaviour will be either "cyclic plasticity" where a closed cycle of permanent strain is formed (Stage 3 in Figure 2.25) or "ratchetting" where permanent strain increases indefinitely (Stage 4 in Figure 2.25). If either of these situation occurs, the structure will

fail. The critical load below which the structure shakes down and above which can cause failure is called the shakedown load.

2.6.1.6.Effect of aggregate type and particle shape

Different granular materials give different resilient responses to cyclic loading. Heydinger et al. (1996) found that gravel had a higher resilient modulus than crushed limestone and slag.

Hicks and Monismith (1971) and Thom and Brown (1989) showed that the resilient modulus increased with surface roughness and angularity of the material. This is because angular particles have better load spreading properties, i.e. better interlock than the rounded particles. Hicks and Monismith (1971) also showed that the Poisson's ratio increased under the same conditions.

2.6.1.7.Effect of load duration, frequency and load sequence

Many researchers, such as Boyce et al. (1976), Shenton (1974), and Thom and Brown (1987), agreed that the load duration and frequency had little or no significant effect on the resilient properties of granular materials. However, Lekarp et al. (2000a) stated that an increase in the frequency could result in the reduction of resilient modulus when the moisture content was close to saturation. This is because as the pore pressure increases, the effective stress decreases. The literature review of Lekarp et al. (2000a) also showed that the

order in which the stresses were applied to a specimen had minimal effect on the resilient properties of granular materials.

2.6.2. Permanent deformation of cyclically loaded aggregate

Permanent deformation of granular materials in a rail track is normally in the form of settlement. Unlike resilient behaviour, not enough research has been focused on permanent deformation of granular materials. This is due to the fact that it takes a long time to perform thousands of cycles of load. However, it is known that permanent deformation of granular materials under cyclic loading is affected by many factors, such as:

- Stress level
- Principal stress rotation
- Number of load cycles
- Moisture content
- Stress history
- Loading sequence
- Density
- Grading
- Loading frequency

The effect of each factor is reviewed below.

2.6.2.1.Effect of stress level

Similar to resilient properties, stress level is one of the most important factors that affect the amount of permanent deformation of granular materials. Morgan (1966) concluded that permanent deformation increased with increasing deviatoric stress or decreasing confining stress. Since then, several researchers have been using some form of stress ratio that consists of both deviatoric and

confining stresses (Lekarp et al, 2000b). Brown and Hyde (1975) found that the permanent strain was directly proportional to the ratio of deviatoric stress to confining pressure. However, the same stress ratio can result in a different permanent strain if the deviatoric stress is larger. Figure 2.26 (Knutson, 1976) shows that stress ratio 60/15 causes larger permanent strain than 20/5 while both correspond to the ratio of 4.

2.6.2.2.Effect of principal stress rotation

Principal stress rotation occurs in pavements under moving traffic as shown in Figure 2.27. According to the literature review of Lekarp et al. (2000b), the effect of principal stress rotation is still unclear. However, test samples subjected to principal stress rotation showed larger permanent strain than the samples without principal stress rotation.

Lim (2004) noted that there was no principal stress rotation for ballast near sleepers. The traffic load is transferred through the sleeper onto the ballast with the load being more concentrated near the sleeper. Therefore, the major principal stress of the ballast near the sleepers suddenly increases as the wheels are directly on top and rapidly decreases as the wheels move away. However, deeper ballast or subgrade will be subjected to principal stress rotation depending on the load spreading capability of the ballast.

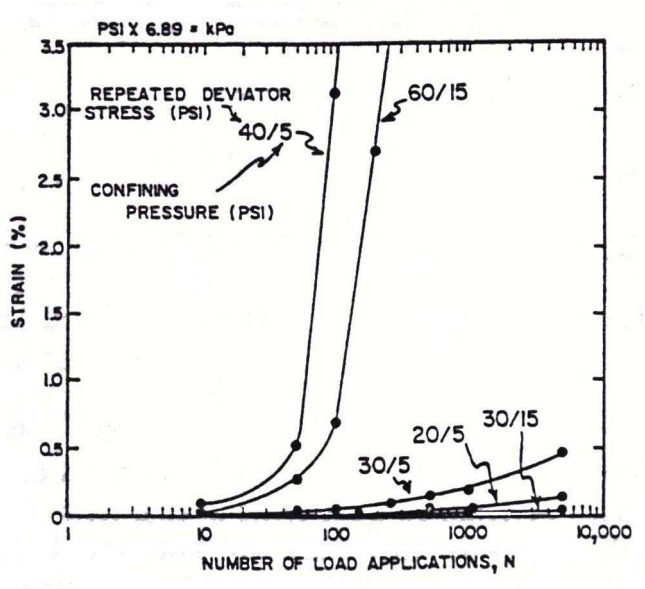

Figure 2.26. Effect of stress ratio on permanent strain (Knutson, 1976)

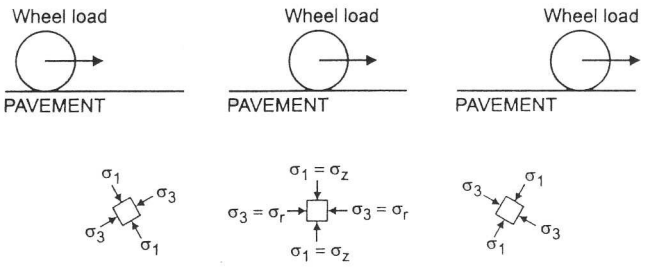

Figure 2.27. Stress rotation beneath moving wheel load (Lekarp et al., 2000a)

2.6.2.3.Effect of number of load cycles

Each load application, in a series of cyclic loading, contributes a small amount of accumulative permanent deformation. Figure 2.26 shows that permanent strain increases with the number of load cycles. According to Morgan (1966), the permanent strain can still increase after 2,000,000 load cycles. Barksdale (1972) and Shenton (1974) both found that permanent deformation is a linear function of logarithm of the number of load cycles as shown in Figure 2.28.

The figure also shows that the rate of permanent deformation accumulation decreases with increasing number of load cycles. However, Lekarp and Dawson (1998) stated that this could happen when the applied stresses were low. High stresses will result in an increasing rate of permanent strain accumulation according to the ratchetting period of the shakedown theory explained in Section 2.6.1.5 (Stage 4 in Figure 2.25).

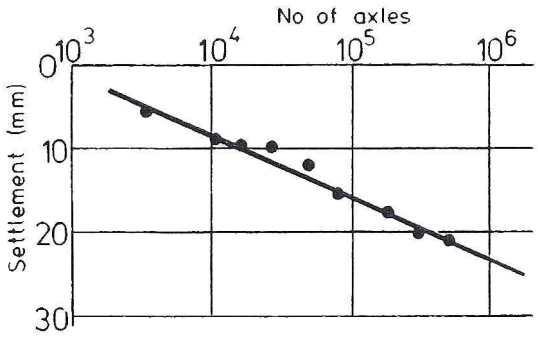

Figure 2.28. Permanent deformation as a linear function of logarithm of number of load cycle (Shenton, 1974)

2.6.2.4.Effect of moisture content

It is widely known that as moisture content increases and saturation is approached, the deformation resistance in granular materials decreases. This is because it leads to the development of excessive pore water pressure under rapid loading. As a consequence, it reduces the effective stress, stiffness and permanent deformation resistance. Researchers, such as Barksdale (1972) and Thom and Brown (1987) have confirmed this finding.

However, this is not generally true. For truly dynamic events e.g. very high speed triaxial test, the material strength can increase dramatically. This then might compensate for the reduction in deformation resistance from the increased moisture content.

2.6.2.5.Effect of stress history and loading sequence

Limited research focused on the effect of stress history on the permanent deformation of granular materials under repeated loading. However, the widely accepted finding is that each load application stiffens the material and results in more deformation resistance in subsequent loading applications. Brown and Hyde (1975) studied this effect by applying cyclic loading with maximum deviatoric stress of 650 kPa on two specimens. However, one specimen was subjected to the maximum deviatoric stress of 650 kPa immediately while in the other specimens, the maximum deviatoric stress successively increased from 250, 350, 450, 550, to 650 kPa. The permanent strain from a successive increase in the stress level was significantly smaller than the strain that occurred when the highest stress level was applied immediately as shown in Figure 2.29.

According to Selig and Waters (1994), the loading sequence has no effect on permanent strain accumulation. Figure 2.30 shows the permanent strain of different samples under different loading sequences where the deviator stresses were changed after every 1,000 cycles. It can be seen that the final permanent strains are approximately equal.

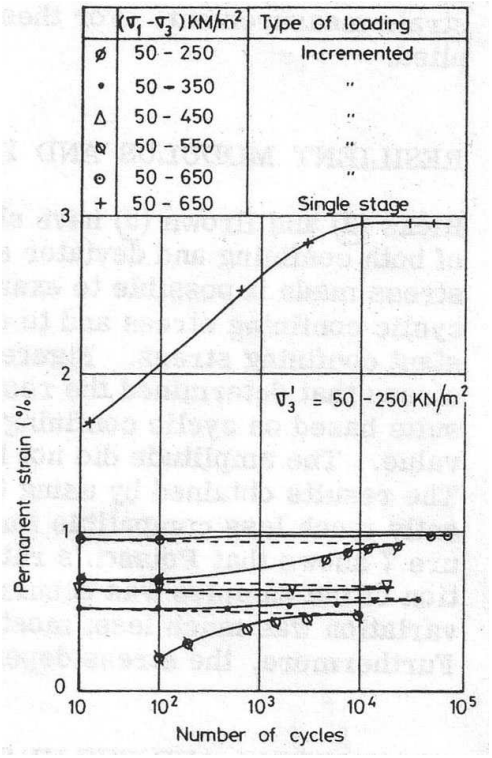

Figure 2.29. Effect of stress history on permanent strain (Brown and Hyde, 1975)

2.6.2.6.Effect of density and grading

Many researchers such as, Barksdale (1972), Thom and Brown (1988), and Knutson and Thompson (1978) agree that permanent deformation decreases with increasing density of granular materials.

Thom and Brown (1988) also found that the effect of density was more significant than the effect of grading as shown in Figure 2.31. The grading parameter in Figure 2.31 was used in their experiment to define the particle size distribution of each sample as shown in Figure 2.32. Furthermore, the sample compaction in their tests was performed by tamping in five layers each of 30 mm thickness with a 38-mm diameter rod. The compactive effort was controlled manually.

However, Dawson et al. (1996) found that the effect of grading was more significant but this may be material dependent.

2.6.2.7.Effect of loading frequency

Very limited research focused on the effect of loading frequency on permanent deformation. However, Shenton (1974) found that loading frequency has no effect on permanent deformation of ballast as shown in Figure 2.33.

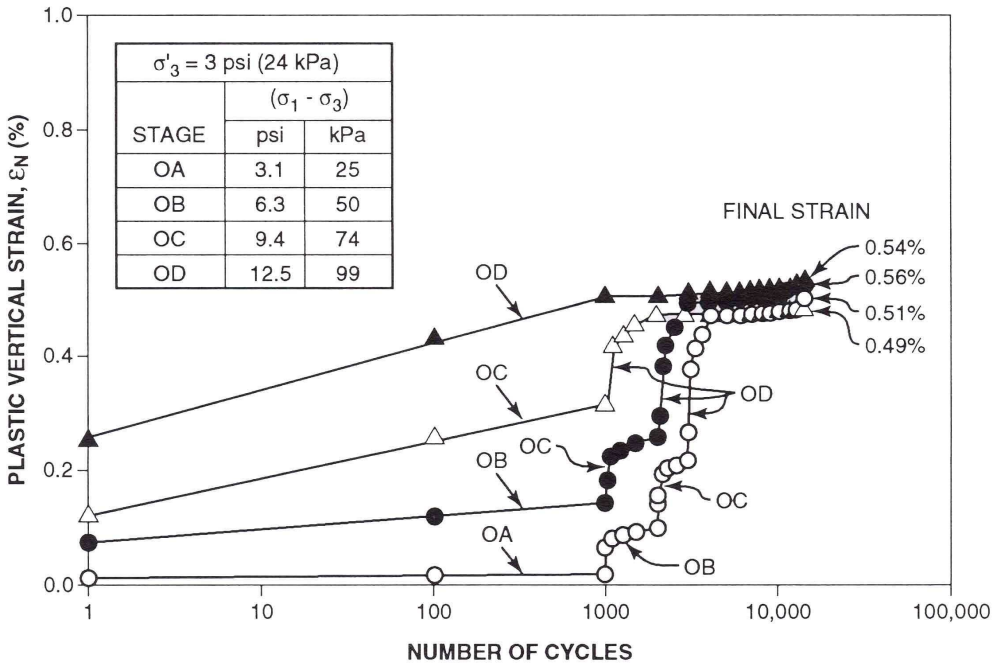

Figure 2.30. Effect of loading sequence on permanent strain (Selig & Waters, 1994)

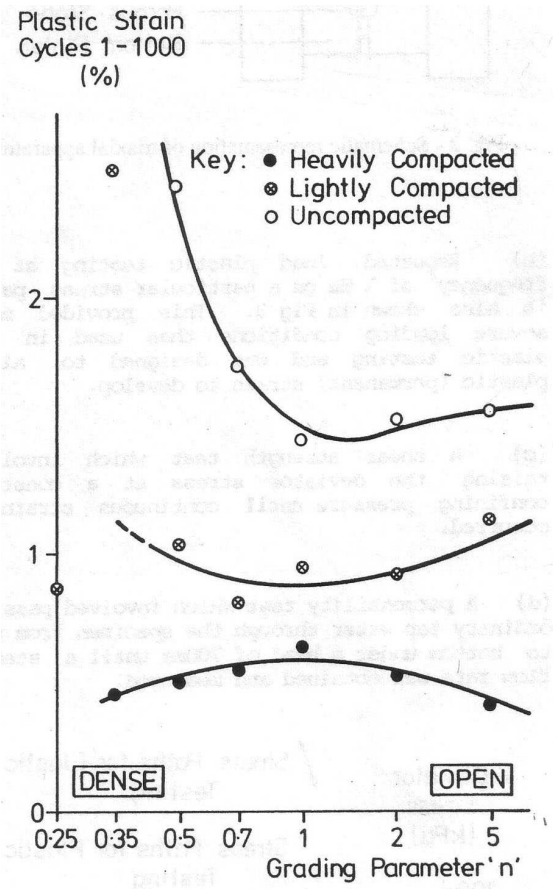

Figure 2.31. Effect of density and grading on permanent strain (Thom and Brown, 1988)

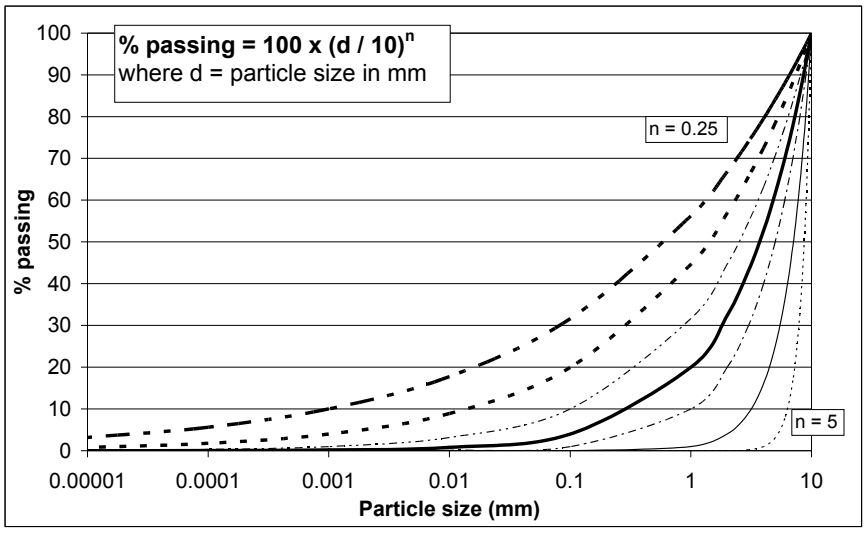

Figure 2.32: Particle size distribution of different samples in Thom and Brown (1988)

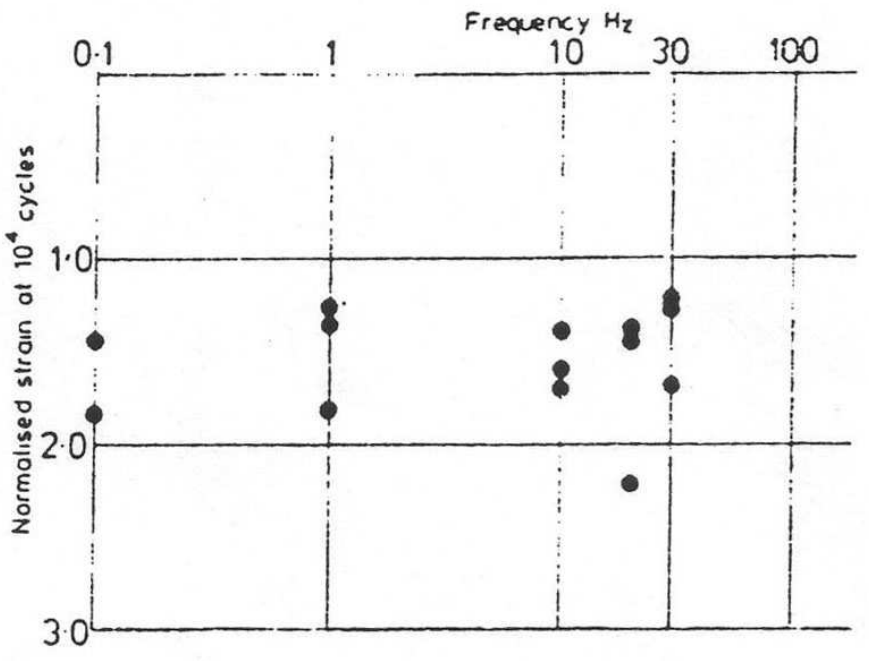

Figure 2.33. Effect of loading frequency on permanent strain (Shenton, 1974)

2.7. Laboratory tests on ballast

2.7.1. Box test

A box test simulates ballast behaviour and performance under field conditions. Ballast is placed in a box with a sleeper segment shown in Figure 2.34. The test can simulate traffic loading on the rail section shown in Figure 2.35. It is also versatile as various types of results can be measured form the test such as, sleeper settlement, horizontal stress in the ballast, and ballast stiffness and density for a range of different ballasts.

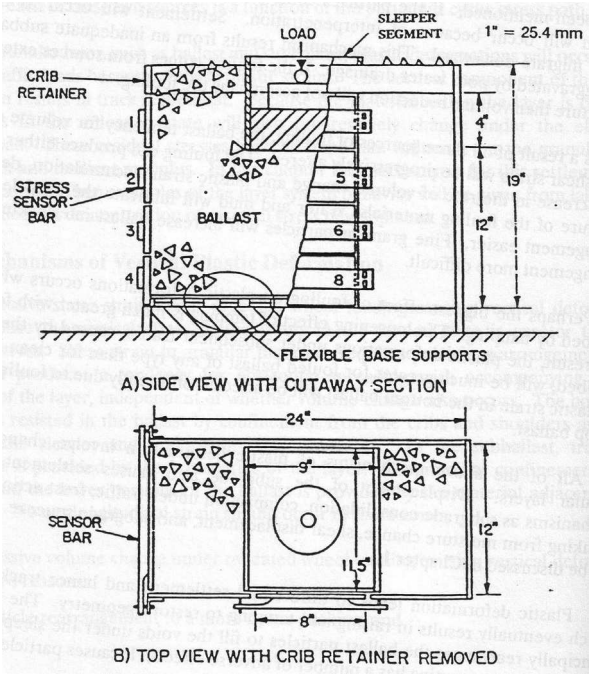

Figure 2.34. Diagram of a box test (Selig and Waters, 1994)

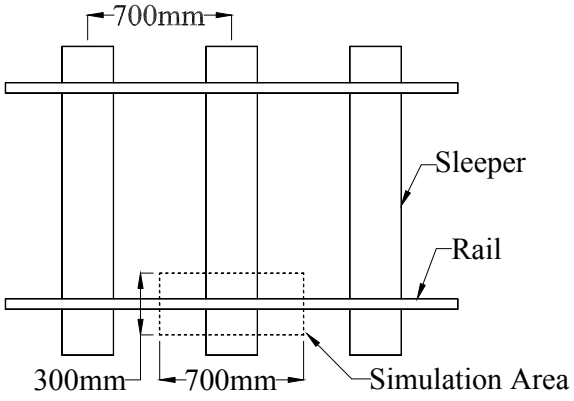

Figure 2.35. Plan of rail and sleepers showing section represented by the box test (Lim, 2005)

The sleeper settlement can be measured by attaching an LVDT (Linear variable differential transformer) displacement transducer to the sleeper. Selig and Waters (1994) measured the horizontal stress in the ballast by installing stress sensors on the wall. Figure 2.36 shows the horizontal stress from one of the

sensors in their test. It can be seen from the figure that both horizontal stresses of ballast at loaded and unloaded states (at maximum and minimum load of the cyclic loading, respectively) eventually reached 30 kPa. The ballast stiffness from the box test is very similar to the resilient modulus. The stiffness can be calculated by dividing the applied deviatoric stress by the resilient displacement of ballast in a cycle.

The breakage of the ballast in the box test usually occurs in the area under the sleeper segment as the ballast in this area is vertically loaded. Lim (2004) observed the ballast degradation of the whole box and confirmed that the ballast degradation in the other areas was negligible. Selig and Waters (1994) dyed the ballast under the sleeper to aid breakage observation.

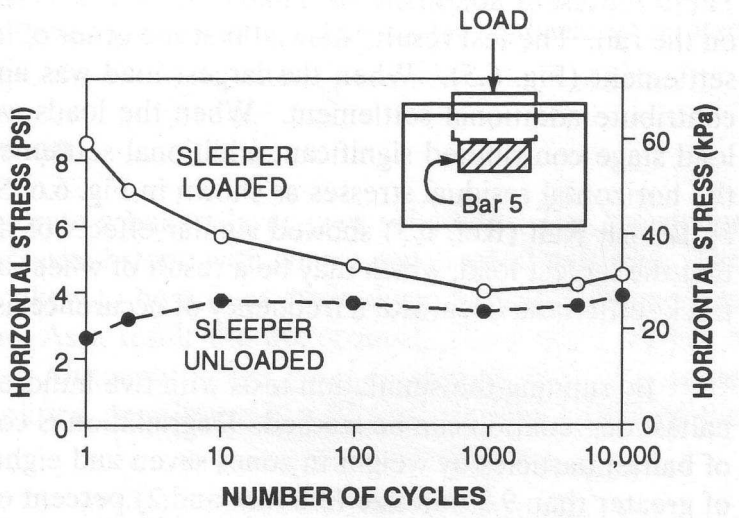

Figure 2.36. Effect of repeated load on horizontal stress in box test (Selig and Waters, 1994)

The effect of track maintenance can also be observed in the box test. Lim (2004) simulated tamping maintenance by lifting the sleeper level with the top

of the box. Then, a one-inch-wide chisel was inserted into the ballast using a Kango hammer. This was only to rearrange and loosen the ballast under the sleeper as it usually happens after tamping. However, it could not simulate the impact of tamping tines and the squeezing operation.

2.7.2. Triaxial test

Many researchers such as Shenton (1974), Raymond and Buthusrt (1994), Skoklund (2002), Key (1998) and Fair (2003) performed triaxial tests on ballast to study its properties. Monotonic (static) triaxial tests on ballast determine its angle of friction and strength. Cyclic (repeated loading) triaxial tests on ballast simulate traffic loading in a controlled manner. Different aspects of triaxial tests on ballast are discussed below.

2.7.2.1.Specimen compaction

Many researchers compacted triaxial test specimens in layers. Shenton (1974) compacted his ballast specimens by tamping it in four layers. However, Kolisoja (1997) commented that this compaction method was not recommended even with other types of granular material. This is because the compaction effort may cause particle crushing and the result of compaction depends on the operator.

Skoglund (2002) pressed a vibrating compaction plate against each layer of his specimen. Key (1998) and Fair (2003) are the only researchers who compacted their specimens by dropping ballast particles into a mould which is on a vibrating table. This is because they thought that compaction in layers was not

suitable for a ballast sample, because with material of this size, compaction in layers will cause unusual levelling and orientation of the particles with the flat face against the compaction tool. This perhaps creates artificial planes of weakness in the sample and alters the sample's behaviour.

2.7.2.2.Specimen size

According to Skoglund (2002), the typical value of D/d_{max} ratio is 5-7 (where D = specimen diameter and d_{max} = maximum particle size). The reason behind is that the diameter must be sufficiently large so that there are enough particles across the diameter to give a sufficiently representative sample. According to the literature review of Fair (2003), the D/d_{max} ratios from different researchers varied from 4.7 to 10.

The recommended H/D (height to diameter) ratio of a sample by Bishop and Green (1965) was 2. This is to eliminate the effect of friction at both ends of the sample. Duncan and Dunlop (1968) concluded that end friction caused an insignificant increase in the angle of shearing resistance in their drained triaxial tests on sand. Furthermore, they added that lubrication at both ends was necessary when volumetric strain needed to be calculated because end friction usually causes the triaxial specimen to bulge into a barrel shape. This means the diameter of the specimen is not uniform through the whole height of the sample and therefore affects the calculation of volumetric strain.

According to the review of Key (1998), the most successful method of reducing end friction is to sandwich layers of silicone grease between thin

rubber membranes. However, end lubrication also has some drawbacks. In a sample with coarse particles, the particles could penetrate through the cushion and bear on the platen. Furthermore, the grease might be squeezed from the ends under the load.

2.7.2.3.Instrumentation

According to Key (1998), load and deformation of the sample should be monitored inside the triaxial cell to reduce errors. Measuring load with a load cell inside the triaxial cell will measure the force applied on the sample directly while the reading from a load cell outside the triaxial cell can be affected by friction between the loading ram and its bearing. Skoglund (2002) measured axial deformation between both ends of his samples while Key (1998) used an LVDT to read the deformation against the cell top. Many researchers such as Shenton (1974), Key (1998) and Skoglund (2002) used on-sample instrumentations to measure radial strain. However, they may cause an error in ballast triaxial testing as they may measure grain movement instead of radial strain. This is due to the large grain size of ballast.

2.7.2.4.Cyclic loading

According to Shenton (1975), the maximum vertical stress in the ballast at the sleeper contact varied between 200 and 250 kPa under a 100 kN load on the sleeper as shown in Figure 2.37. This is in agreement with Raymond and Buthurst (1994) who reported that the average vertical stress at the sleeper-

ballast interface was 140 kPa. Key (1998) varied the deviator stress between 12.5 kPa and 250 kPa.

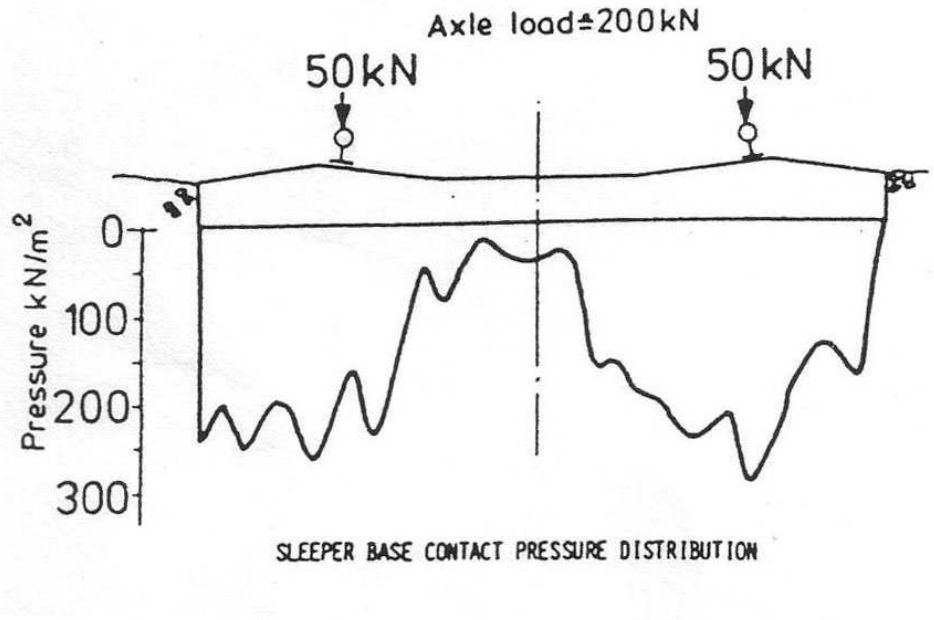

Figure 2.37. Vertical stress at the sleeper base contact

According to Selig and Alva-Hurtado (1982), in-situ confining pressure of self standing ballast perpendicular to the rail was approximately 5 – 40 kPa based on assumed ballast coefficients of lateral earth pressure. Furthermore, the box tests of Selig and Waters (1994) showed that the horizontal stress at the loaded and unloaded states would eventually reach approximately 30 kPa as previously shown in Figure 2.36.

Loading frequency varies between different researchers. Key (1998) applied 0.16 Hz for the first 50 cycles and then used 0.5 Hz for the rest of the test. Shenton (1974) varied the loading frequency from 0.1 to 30 Hz. However, he used 0.1 Hz for the first eight cycles in all of his tests. The reason for applying

low frequency during the beginning of the test is that the deformations during the first few cycles are generally large and they might exceed the capacity of a testing machine in terms of the hydraulic oil flow required to give the required deformation rate.

However, the typical loading frequency of traffic loading in the track is normally around 8 – 10 Hz for normal train and may reach 30 Hz for high speed train. It can be seen that the frequency that Key (1998) used in his experiment (0.5 Hz) was much smaller than typical frequency. This was because his volume change measurement would not work with higher frequency.

2.7.2.5.Membrane correction

Thick rubber membrane can provide extra confining pressure to a triaxial test sample. However, both Indraratna et al. (1998) and Key (1998) agreed that the confinement provided by the membrane was negligible compared to the confining stress. Indraratna et al. (1998) stated that with their 4-mm-thick membranes, they found that the membrane correction was negligible. In their tests with 1 kPa confining pressure, the maximum correction was below 8 %, i.e. negligible. The membrane correction can be calculated according to the derivation by Kuerbis and Vaid (1990) and is shown in Equations 2.10 and 2.11.

$$\sigma'_{rm} = \sigma'_{r} - \frac{4E_m t_0 (2 + \varepsilon_v + \varepsilon_{Ma})\varepsilon_v}{3D_0 (2 - \varepsilon_v + \varepsilon_{Ma})} \quad (2.10)$$

$$\sigma'_{am} = \sigma'_{a} - \frac{4E_m t_0 (2 + \varepsilon_v + \varepsilon_{Ma})(3\varepsilon_{Ma} + \varepsilon_v)}{3D_0 (2 - \varepsilon_v + \varepsilon_{Ma})} \quad (2.11)$$

where σ'_{rm} and σ'_{am} = Corrected radial and axial stresses

σ'_{r} and σ'_{a} = Uncorrected radial and axial stresses

E_m = Young's modulus of the rubber membrane

t_0 = Initial thickness of the membrane

ε_v and ε_{Ma} = Volumetric and axial strains in the specimen

D_0 = Initial diameter of the membrane

2.8. Summary

Ballast is a crushed granular material placed as the top layer of substructure in a rail track. The properties of ballast in the UK are specified in RT/CE/S/006 Issue 3 (2000) which follows the European standard BS EN 13450 (2002). The main functions of ballast are to resist vertical, lateral, and longitudinal forces in the track. Ballast also has to provide resiliency and energy absorption for the track from vertical traffic loading. After long-term service, track settlement occurs and can be restored in the ballast layer. This is done by first lifting the sleeper to create the void between the sleeper and the ballast. Tamping tines or a stoneblowing tube are then inserted into the ballast layer to squeeze the ballast or blow stones into the void. However, ballast can become fouled by small particles after subjecting the ballast to long-term traffic loading and track geometry maintenance. The fouling materials can reduce ballast performance

and cause severe track deterioration if the degree of fouling is high and water is presented.

The strength of a soil particle can be found by compressing the particle between two flat platens. The strength is the applied force divided by the square of the size of the particle at failure. Different literature suggests that particle strengths follow Weibull statistics (Weibull, 1951). According to Weibull statistics, the particle survival probability is a function of applied stress, characteristic strength at which 37 % of tested particles survive, and the Weibull modulus. The characteristic strength is approximately equal to the particle average strength and the Weibull modulus indicates the variability of strength i.e. it increases as the variability decreases. Weibull statistics can also explain the size effect on strength of particles i.e. larger particles have lower strengths. McDowell (2001) suggested that to use Weibull statistics in a single particle crushing test, at least thirty test particles are needed.

McDowell et al. (1996) suggested that the probability of particle breakage in an aggregate increases with an increase in applied stress, increase in particle size, and a decrease in the coordination number (average number of contact per particle). The size and coordination number are two opposing effects as small particles are stronger but have fewer contacts than large particles. However, it has usually been found in literature that the effect of coordination number dominates over the size effect as small particles are more likely to break.

When an aggregate is subject to one-dimensional compression, the void ratio decreases with increasing applied stress. During the early stage of compression, the behaviour is quasi-elastic where there is some irrecoverable deformation due to particle rearrangement. After the quasi-elastic period, the behaviour changes to plastic where both particle breakage and rearrangement occur to achieve further compaction. During compression, the columns of strong force pass through different particles but change direction when the particles break and rearrange.

Under cyclic loading, the behaviour of the granular material can be divided into resilient and permanent behaviour. The resilient behaviour is characterised by the resilient modulus and Poisson's ratio and the permanent behaviour is characterised by permanent deformation. Both types of behaviour are affected by various factors. The factor that has the most significant effect is stress level. It has been found that the resilient modulus increases considerably with confining pressure but is almost unaffected by deviatoric stress. On the other hand, Poisson's ratio increases with decreasing confining stress and increasing deviatoric stress. The permanent deformation also increases with decreasing confining stress and increasing deviatoric stress.

Box tests and triaxial tests have been used by many researchers to observe mechanical properties of ballast. For the box test, ballast is placed in a box with a sleeper segment and cyclically loaded to simulate a loaded section of a sleeper in a rail track. For the triaxial test, researchers have generally agreed that the sample has to be sufficiently large. The ratio of the sample diameter to

the maximum particle size varies between 4.7 and 10. The recommended ratio of height to diameter of a sample is 2 as this eliminates the effect of friction at both ends for the bulk of the sample. The maximum vertical stress at the sleeper contact and the confining pressure of ballast perpendicular to the rail in a track were approximated to be 200 – 250 kPa and 5 – 40 kPa, respectively (Shenton, 1975 and Selig and Alva-Hurtado, 1982). Hence, the stress level in triaxial tests should be comparable to these values. Lastly, different researchers agree that the extra confinement provided by rubber membrane is negligible compared to the applied confining stress in triaxial tests.

Different researchers have performed cycling loading in a box test which is a reduced scale traffic loading simulation. It would be interesting to observe ballast behaviour under both simulated traffic loading and tamping maintenance at the full scale. Furthermore, the triaxial testing of ballast has not been widely studied compared to other types of granular materials. Therefore, more triaxial tests on ballast and comparisons with the full-scale simulated traffic loading test would shed some light in this field of research. However, particle strength analysis and other ballast index properties such as LAA and MDA values should be studied prior to those tests as the strength or the index properties are the fundamental properties of ballast particles and might explain the behaviours of ballast in those tests.

3. Ballast properties and strength

3.1. Introduction

This chapter focuses on the properties and strength of the three types of ballast used in this project namely; granites A and B and limestone. Granite A is the only ballast among the three that is still in use on the UK rail network. Granite B and limestone were used in the past but can no longer pass the specification. The properties that were of interest are particle size distribution, Los Angeles abrasion (LAA), micro-Deval attrition (MDA), flakiness index, and water absorption. These properties except water absorption are used to define the specification for track ballast as explained in the previous chapter. The ballast strength was tested by single particle crushing tests following Lim (2004). Some of ballast strengths in this project are compared with the ones in Lim (2004). Furthermore, the strength of painted ballast used in the Railway Test Facility (RTF) was tested and compared to the strength of normal ballast i.e., unpainted. The ballast strength was analysed by Weibull statistics and two-sample unpaired t-test.

3.2. Ballast properties

When the ballast first arrived in the laboratory, the physical appearance of ballast was observed. Most granite A particles were rounded and had rough surface. Granite B was relatively smooth but was flat and long. Limestone was angular compared to the other two types of ballast. The broken pieces of limestone were usually sharp.

After that, the ballast was then sieved to find its grading and then compared to the grading specification (RT/CE/S/006 Issue 3, 2000). This is shown in Figure 3.1. It can be seen from the figure that the all three types of ballast are within the specification. Furthermore, Table 3.1 shows the coefficient of uniformity and D_{50} of each ballast.

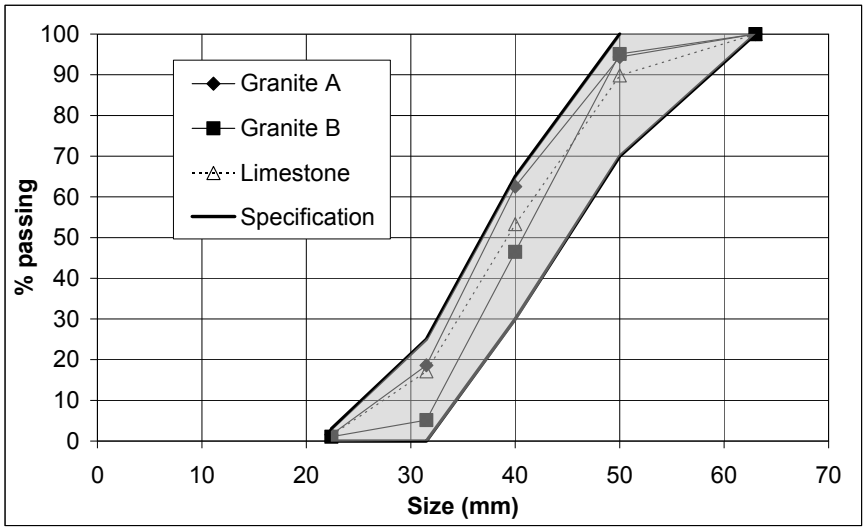

Figure 3.1. Ballast grading and specification

Ballast type	Coefficient of uniformity (D_{60}/D_{10})	D_{50} (mm)
Granite A	1.47	37.6
Granite B	1.32	40.7
Limestone	1.53	39.2

Table 3.1. Coefficient of uniformity and D_{50} of each ballast type in this project

The ballast was also sent to Lafarge Aggregates Ltd. which is an industrial partner of the School of Civil Engineering, University of Nottingham for Los

Angleles abrasion, micro-Deval attrition, flakiness index, and water absorption tests. The procedures of these tests except the water absorption test were explained in Section 2.3.1.

For water absorption test, the test ballast is soaked in water for 24 hours. After that, it is wiped and heated until all visible films of water are removed but the test ballast still has a damp appearance. The test ballast is then dried in an oven until a constant mass is reached. The water absorption is the percentage of water mass that is removed from the test ballast by the oven relative to the mass of the oven-dried ballast (BS EN 1097-6, 2000).

The results from those tests are presented in Table 3.2. The table also shows if each property of the ballast passes the specification.

	LAA	MDA	Water absorption	Flakiness index
Specification	Not exceed 20 %	Not exceed 7 %	N/A	Not exceed 35 %
Granite A	9 % (pass)	6 % (pass)	0.5 %	5 % (pass)
Granite B	13 % (pass)	8 % (fail)	0.5 %	35 % (pass)
Limestone	22 % (fail)	12 % (fail)	1.0 %	6 % (pass)

Table 3.2. LAA, MDA, water absorption, and flakiness index

3.3. Ballast strength

3.3.1. Test procedure

The tensile strength of a ballast particle can be measured by the single particle crushing test. In this test, a ballast particle is compressed between two flat platens until it reaches failure. The particle fails by fast fracture and breaks into two or more pieces. This test has four main assumptions. They are:

i) Fracture of testing particles was caused by the induced tensile stress, i.e., the fracture initiates within the bulk of the material.

ii) Testing particles are homogeneous and isotropic. McDowell and Amon (2000) and McDowell (2002) showed that inhomogeneous and anisotropic material did not follow Weibull statistics.

iii) All loading geometries are similar. This is the assumption of Weibull analysis for soil particles (McDowell and Amon, 2000).

iv) The contact areas between the testing particles and the platens are small. Shipway and Hutchings (1993) concluded that bulk fracture was more likely to occur than the surface fracture if the contact areas were small.

The ballast was sieved to obtain particles of the required size (10 – 14 mm and 37.5 – 50 mm in this project). Then, thirty ballast particles had to be chosen for each test. The criteria for the chosen particles were:

i. The particles must be quasi-spherical. This is to minimise the contact areas.

ii. The contact area between the particle and the top plate should be approximately at the centre of the particle and should be small. It is ideal for the same to apply to the contact area

between the particle and the bottom platen. However, this is very difficult because the particle must remain in equilibrium, and this necessitates a larger contact area.

iii. The particle must not have two or more obvious contact points on the bottom platen i.e. no arches formed by contact points at the bottom. This is to avoid failure in bending.

In some tests, ballast particles needed to be painted (see Section 3.3.2 and Table 3.3 for more details). Painting was performed by dipping ballast particles into a mixture of emulsion paint and water with ratio of 1: 3 (paint: water). The particles were then placed on a sieve to drain the paint for a few minutes. They were then put in a metal tray and dried in an oven overnight to ensure that they were completely dried.

Figure 3.2 shows the test configuration. The particle stands on the bottom platen which is fixed in position. The top platen is attached to a Zwick testing machine. Both platens are made from case-hardened mild steel to avoid plastic deformation of the platens and minimise the contact areas. They have diameters of 140 mm. A hollow Perspex cylinder which has a slightly larger diameter is used to confine both platens and broken fragments. As the particle is loaded, load and displacement are recorded by a computer and can be plotted in real time on the computer monitor.

Figure 3.2. Configuration of a single particle crushing test

The loading rate of the test is 1 mm/min. The loading rate of 1 mm/min was chosen because at high loading rates, the broken fragments might still be attached to the bulk particle and loaded (Lim, 2004). This means that two or more particles are crushed. However, the loading rate of 1 mm/min does not guarantee that the broken fragments will fall away from the bulk particle. Therefore, if there is a drop in the load, the test should be stopped (if failure is suspected to have occurred) and the particle taken out and checked to see if failure has occurred. Failure of a particle is defined such that the total size of broken fragments is at least one-third of the original size of the particle (Lim, 2004). If the particle has not reached failure yet, small broken fragments will be removed before the particle is put back in the same configuration and then loaded until it reaches failure. The results of the tests were analysed by Weibull statistics following McDowell and Amon (2000). The governing equation of Weibull statistics is shown in Equation 3.1

$$P_s = \exp\left[-\left(\frac{\sigma}{\sigma_o}\right)^m\right] \quad (3.1)$$

where

P_s = Survival probability

σ = Tensile stress at failure

σ_o = Characteristic stress at which 37% of tested particles

m = Weibull modulus

It should be noted that σ_0 is approximately equal to the average particle strength. Weibull modulus relates to variability of stress. It reduces as variability increases. The characteristic stress at failure for each particle was obtained by dividing the failure force (peak force) by the square of the particle size at failure i.e., the distance between both platens at failure. To compute the survival probability of each tensile stress at failure, the tensile stresses at failure from each set of tests were ranked in ascending order. According to Davidge (1979), the survival probability can be calculated by Equation 3.2.

$$P_s = 1 - \frac{i}{N+1} \quad (3.2)$$

where i = ith ranked sample

N = Total number of samples

Therefore, for a test with thirty particles, the smallest stress gave a survival probability of 30/31 and the largest gave a survival probability of 1/31.

To use Equation 3.1 in the test, it must be re-written as shown in Equation 3.3.

$$\ln\left(\ln\left(\frac{1}{P_s}\right)\right) = m\ln\sigma - m\ln\sigma_o \qquad (3.3)$$

By plotting $\ln(\ln(1/P_s))$ against $\ln\sigma$, the Weibulll modulus can be determined from the slope of the line of best fit and σ_o is the value of σ when $\ln(\ln(1/P_s)) = 0$. The plots from different tests are shown in Section 3.3.3.

3.3.2. Test Programme

Eight single particle crushing tests were performed in this project. The details of the tests are shown in Table 3.3. Each test contained thirty particles. The ballast in tests 4, 6, and 8 were painted like the ballast in the Railway Test Facility (Chapter 4). This is to check if painting affects ballast strength.

3.3.3. Weilbull probability plots

The Weibull probability plots are shown in Figure 3.3. As Lim (2004) performed the test on 10-14 mm and 37.5-50 mm granite A, the results of tests 1, 2, and 3 are plotted together with his results. Furthermore, the results of normal and painted ballasts of the same type are also plotted together for comparative purposes.

Test	Ballast type	Colour	Size
1	Granite A	Normal	10 – 14 mm
2	Granite A	Normal	37.5 – 50 mm
3	Granite A	Normal	37.5 – 50 mm
4	Granite A	Painted	37.5 – 50 mm
5	Granite B	Normal	37.5 – 50 mm
6	Granite B	Painted	37.5 – 50 mm
7	Limestone	Normal	37.5 – 50 mm
8	Limestone	Painted	37.5 – 50 mm

Table 3.3. Programme of single particle crushing test

It can be seen that most plots have downward curvature at low survival probabilities. This suggests that the ballast particles have a minimum strength. According to Lim (2004), this is due to the grinding process of ballast in the manufacturing phase. The particles that survived the grinding process are statistically strong as the weak ballast could not have survived the process i.e., the grinding process is also a proof test for ballast. Furthermore, the plots in each graph are comparable to each other. However, this does not imply that they are statistically equal. As a result, two-sample unpaired t-test is used to compare the results.

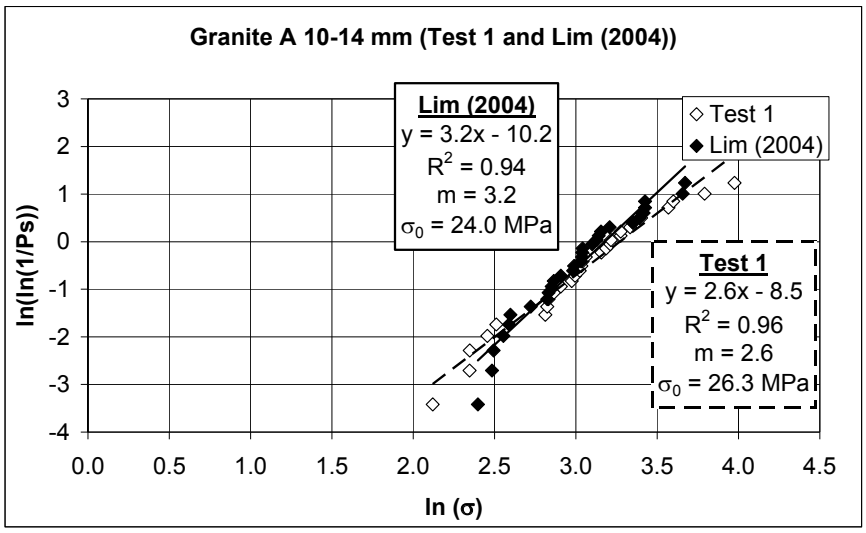

Figure 3.3a. Weibull probability plots for 10 – 14 mm granite A

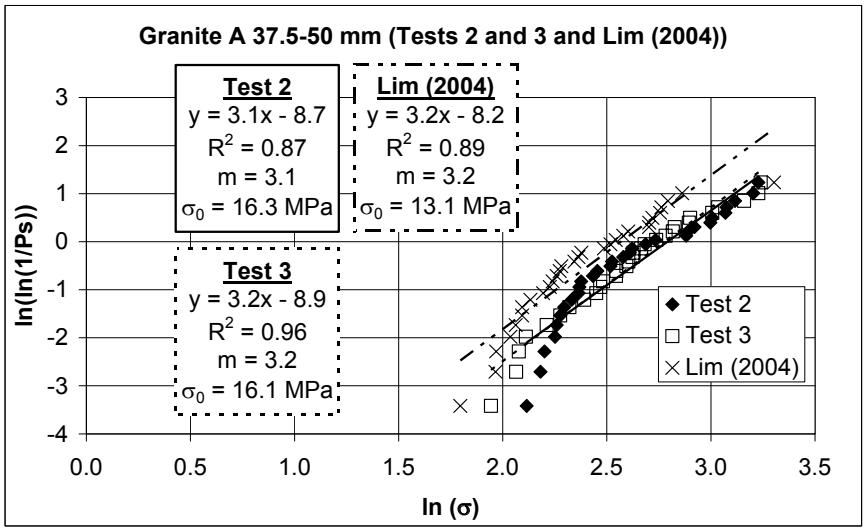

Figure 3.3b. Weibull probability plots for 37.5 – 50 mm granite A

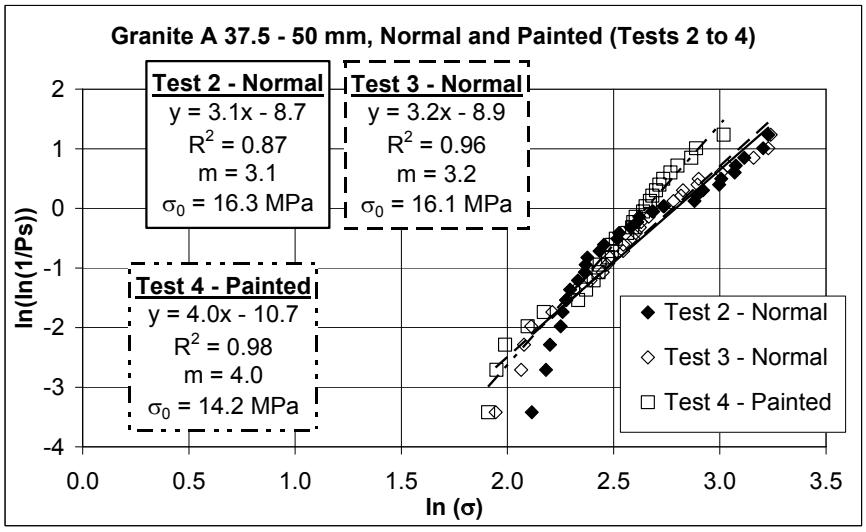

Figure 3.3c. Weibull probability plots for 37.5 – 50 mm normal and painted granite A

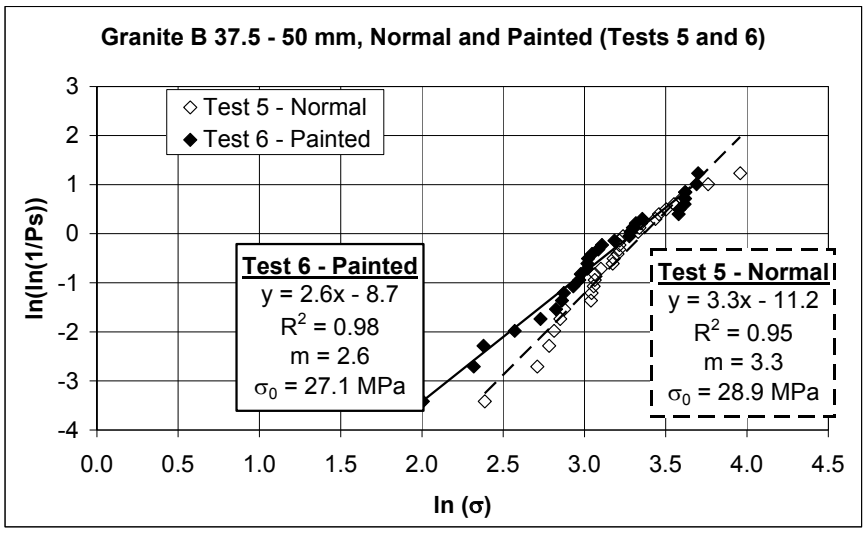

Figure 3.3d. Weibull probability plots for 37.5 – 50 mm normal and painted granite B

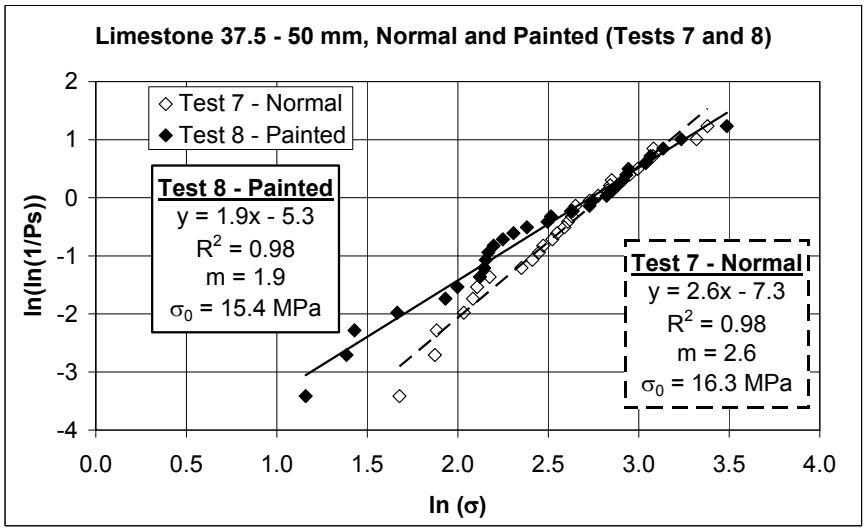

Figure 3.3e. Weibull probability plots for 37.5 – 50 mm normal and painted limestone

Figure 3.3. Weibull probability plots for different types and sizes of ballast (a) – (e)

3.3.4. Strength comparison by two-sample unpaired t-test

According to McDowell (2001), the confidence limit for a sample mean of particle strength can be deduced from the Student's t-distribution. In this project, the t-distribution is also used for comparing ballast strengths of two different samples with confidence interval of 95%. The main assumption of this method is that the samples are taken from a normal population. Normal and Weibull probability density functions (p.d.f.) with different Weibull

moduli were previously shown in Figure 2.13. It can be seen from the figure that the Weibull p.d.f. is very similar to normal p.d.f. when the Weibull modulus is close to three which reflects the values of Weibull moduli from the tests. Further details of the two-sample unpaired t-test can be found in most statistics textbook such as Devore and Farnum (1999).

This test can be easily performed by the TTEST function in Microsoft Excel. An example of the analysis by TTEST function is shown in Figure 3.4. With the confidence interval of 95%, it can be concluded that both samples are equal if the number that the function returns is larger than 0.05 (Aitken, 2006). In the figure, the returned value is 0.424. Therefore, it can be concluded that both samples has the same strength. All strength comparisons by TTEST function with 95% confidence interval are summarised in Table 3.4.

It can be concluded from Table 3.4 that painting does not affect the strength of the particles and the strengths of 37.5-50 mm granite A from this project (tests 2 and 3) are not statistically equal to that of Lim (2004). The discrepancy may be because the ballast from both tests came from a different production batch. However, tests 2 and 3 gave statistically equal results at the 95% confidence level. In addition, it must be remembered that for the t-test, it must be assumed that the strengths are normally distributed which might not be true for every test.

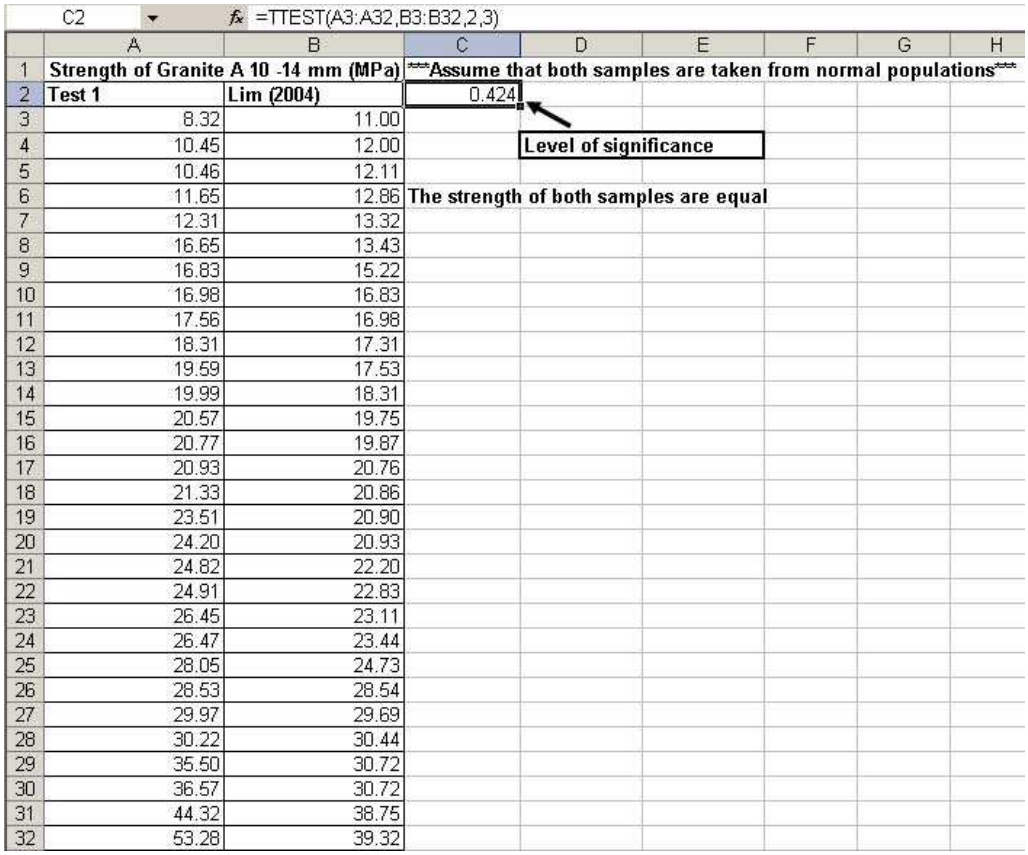

C2 =TTEST(A3:A32,B3:B32,2,3)

	A	B	C	D	E	F	G	H
1	Strength of Granite A 10 -14 mm (MPa)		***Assume that both samples are taken from normal populations***					
2	Test 1	Lim (2004)	0.424					
3	8.32	11.00						
4	10.45	12.00		Level of significance				
5	10.46	12.11						
6	11.65	12.86	The strength of both samples are equal					
7	12.31	13.32						
8	16.65	13.43						
9	16.83	15.22						
10	16.98	16.83						
11	17.56	16.98						
12	18.31	17.31						
13	19.59	17.53						
14	19.99	18.31						
15	20.57	19.75						
16	20.77	19.87						
17	20.93	20.76						
18	21.33	20.86						
19	23.51	20.90						
20	24.20	20.93						
21	24.82	22.20						
22	24.91	22.83						
23	26.45	23.11						
24	26.47	23.44						
25	28.05	24.73						
26	28.53	28.54						
27	29.97	29.69						
28	30.22	30.44						
29	35.50	30.72						
30	36.57	30.72						
31	44.32	38.75						
32	53.28	39.32						

Figure 3.4. Example of TTEST function

Tests to compare	Description	Strength comparison (with 95% confidence interval)
Test 1 and Lim (2004)	10 – 14 mm granite A	Equal
Test 2 and Lim (2004)	37.5 – 50 mm granite A	Not equal
Test 3 and Lim (2004)	37.5 – 50 mm granite A	Not equal
Tests 2 and 3	37.5 – 50 mm granite A	Equal
Tests 2 and 4	37.5 – 50 mm granite A (normal and painted)	Equal
Tests 3 and 4	37.5 – 50 mm granite A (normal and painted)	Equal
Tests 5 and 6	37.5 – 50 mm granite B (normal and painted)	Equal
Tests 7 and 8	37.5 – 50 mm Limestone (normal and painted)	Equal

Table 3.4. Summary of strength comparison

4. Railway Test Facility

4.1. Introduction

Performing experiments on ballast in a railway track is desirable since results can be obtained for real site conditions. However, it is very difficult to control test variables and to collect data on site. The Railway Test Facility (RTF) was designed to produce dynamic loading and tamping cycles in the laboratory at a realistic level and could be related to site conditions. It is located over a pit filled with a subgrade material and railway ballast. The main purpose of this facility in this project is to study ballast deformation from traffic loading and degradation resulting from both traffic loading and tamping. Three actuators were used to supply traffic loading through three sleepers onto the ballast. A tamping bank, which was modified from a real tamper, was used for tamping. Seven tests were performed on this facility in this project. This facility was also used in another project which investigated the effect of geogrid on ballast settlement under traffic loading (Kwan, 2006).

4.2. Test facilities

The whole test facility was housed in a concrete pit with dimensions of 2.1 m (width) x 4.1 m (length) x 1.9 m (depth). An end view of the facility is shown in Figure 4.1. The geogrid in the figure is optional. The reaction test frame was placed in the pit as shown in Figure 4.2. The upper half of the frame was removable to give access to the pit during placement of track bed material and tamping. Four 150-mm-deep hollow core concrete slabs were positioned on the base of the frame to provide support for the subgrade. Polythene sheets were used to waterproof the floor and the walls. Water could be added to the pit via

vertical perforated tubes placed at each corner of the pit to lower the subgrade stiffness if necessary.

Three servo hydraulic actuators were bolted to cross plates under the top two beams in the upper part of the reaction test frame. Each actuator had a built-in displacement transducer to measure its vertical shaft movement. A 100-kN load cell was screwed to the end of each actuator shaft. A three-channel controller and computer in an adjacent room controlled the actuators and collected the data from the displacement transducers and load cells as shown in Figure 4.3. The assembled test facility is shown in Figure 4.4 and loading is transmitted to the sleepers by means of spreader beams (the three steel beams on top of the sleepers in Figure 4.4) located on rollers on the rail seatings. The axial alignment of the actuators is maintained through shallow spherical bearings (mated horizontal curved surfaces) placed at the centre of the spreader beams.

The simulated traffic loading on the sleepers was achieved by applying sinusoidal loading up to 94 kN with a 90° phase lag between each actuator. This is shown in Figure 4.5. This loading pattern was suggested by Awoleye (1993). It simulated a train running over three sleepers with 50% of the wheel load on the middle sleeper and 25% of the wheel load on the outer sleepers. With this load magnitude and distribution, the test in the RTF simulated an axle load of approximately 20 tonnes which is comparable to a typical heavy axle load. However, the finite-element analysis of Watanabe (see Profillidis, 2000, p.81) showed that the sleeper under the loading wheel took 40% of the load,

the adjacent sleepers each took 23% of the load, and the next sleepers each took 7% of the load. Both loading distributions are shown in Figure 4.6 but distribution (b) could not be adopted for the current arrangement of the RTF.

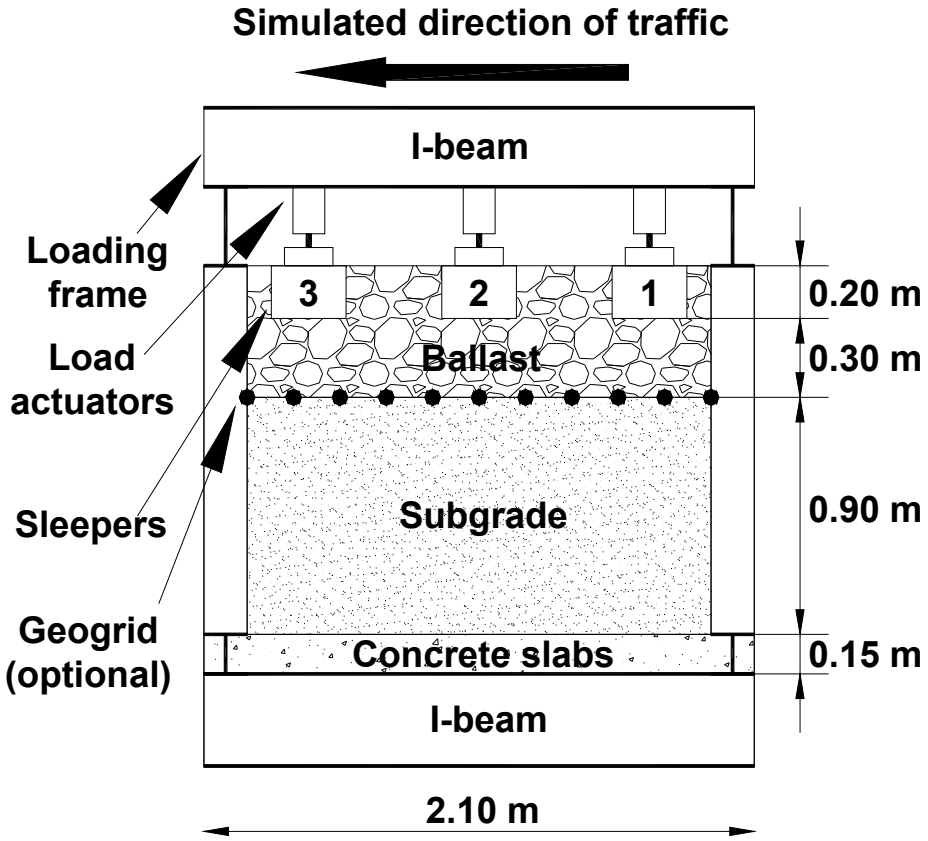

Figure 4.1. End view diagram of the facility

Figure 4.2. Testing frame in the pit

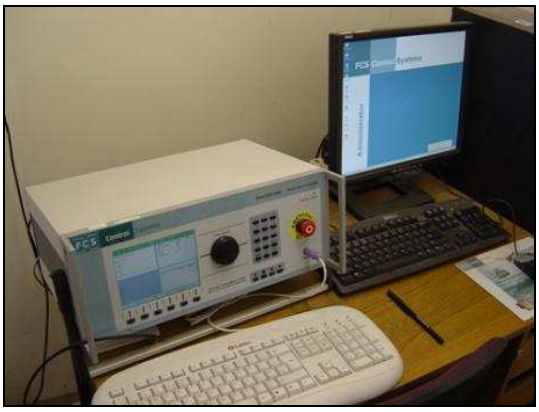

Figure 4.3. RTF control system

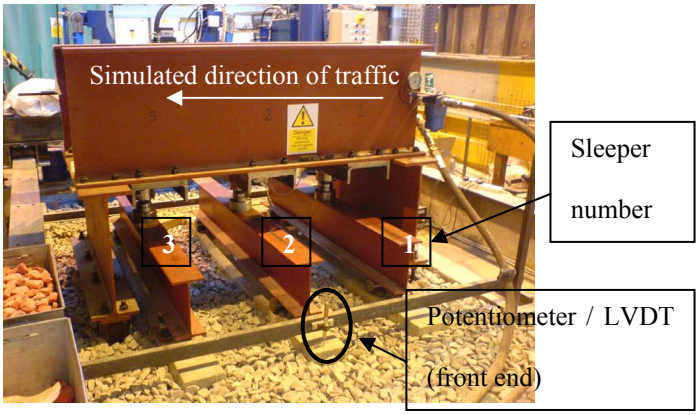

Figure 4.4. RTF loading arrangement

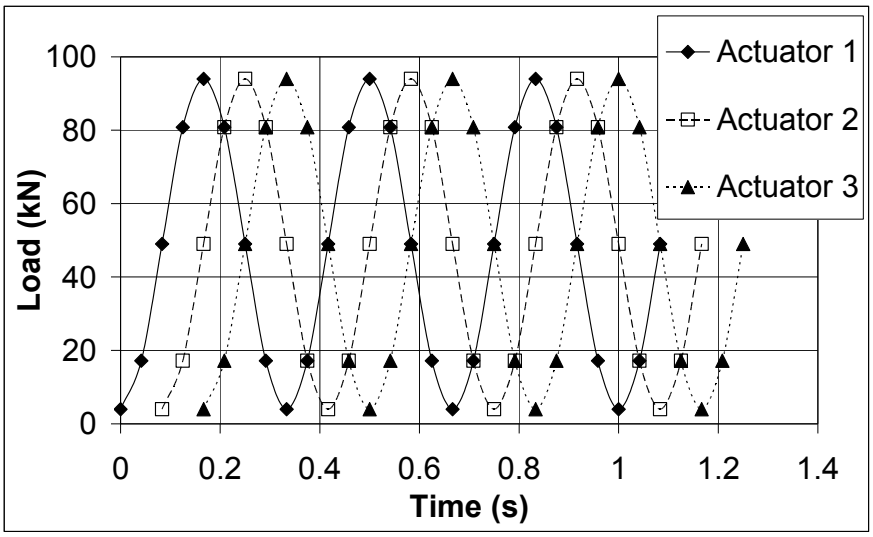

Figure 4.5. Loading pattern used in this project

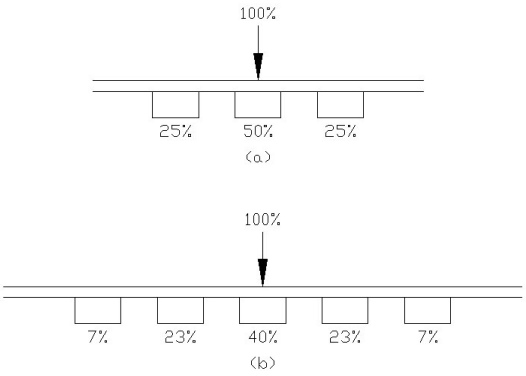

Figure 4.6. Load distributions along successive sleepers (a) suggested by Awoleye (1993) and used in this project and (b) suggested by Watanabe (see Profillidis, 2000)

The seating load of the cyclic loading was originally 2 kN but it was later changed to 4 kN. This was to accommodate any electrical drift of the feedback load cells. If this occurred in the tensile direction, it could cause the actuator to lose contact with the packing on the spreader beam. The safety trip for all actuators was set to 97 kN.

The loading frequency of each test was 3 Hz. This frequency is very low compared to the usual frequency in the track of approximately 8 – 10 Hz. This frequency was however dictated by the pressure and flow capacity of the hydraulic pump. With the above loading pattern and 3-Hz loading frequency, actuator 2 started loading 1/12 seconds after actuator 1 started loading. This simulated a wheel moving from one sleeper to another in 1/12 of a second. The sleeper spacing in the RTF was 0.65 m. Therefore, the test simulated a train speed of 7.8 m/s (0.65 m ÷ 1/12 s) or 28 km/h. The loading frequency of 3-Hz also implied that the time taken for the maximum load to be repeated again on the same sleeper was 1/3 of a second. This indicated that the next wheel would

be on top of the same sleeper in 1/3 of a second. With 7.8 m/s train speed, this meant that the test simulated a 2.6 m axle spacing (7.8 m/s × 1/3 s). Unlike the frequency, this axle spacing is realistic. The spacing of the front pair of axle of a Bombardier BiLevel passenger rail vehicle in Montreal, Canada is also 2.6 m as shown in Figure 4.7 (Bombardier Inc., 2007).

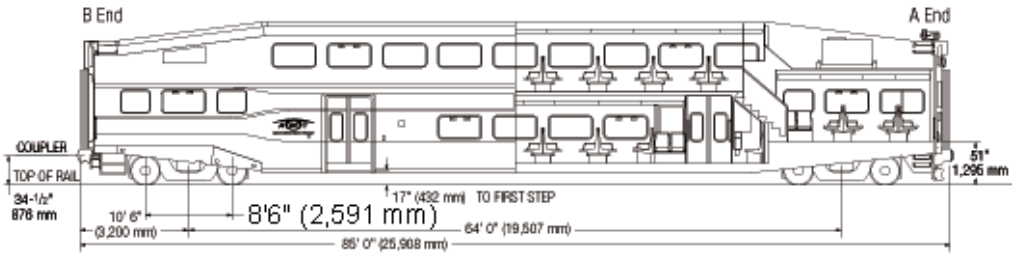

Figure 4.7. Bombardier BiLevel passenger rail vehicle (Bombardier Inc., 2007)

Another part of this facility is the tamping bank which is used to simulate tamping maintenance in a real track (Figure 4.8). When in use, the upper part of the test frame must be removed. It incorporated a refurbished Plasser tamping bank with a vibrating hydraulic cylinder replacing the standard vibrator. The tamping bank was fitted to a frame which spans the pit and runs along longitudinal beams so that it can be located and clamped into position above the location of the rail seating.

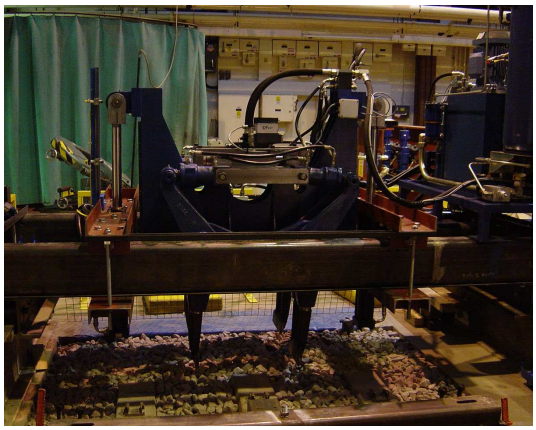

Figure 4.8. Tamping bank

The tamping bank was used to simulate tamping maintenance in a real track. The tamping procedures can be found in Section 2.2.3. The 35-Hz tamping tine vibration of the real system can be achieved in this tamping bank by a hydraulic actuator which could be controlled by a waveform generator to simulate the same vibration. The pressure and oil flow required for this frequency of displacement was maintained by a large accumulator which was connected to the actuator and would partially discharge during the tamping cycle. Another accumulator was used for the lowering, squeezing, and lifting of the tines. These measures were necessary because there was insufficient flow capacity in the laboratory ring main. The system then automatically recharged the accumulators ready for the next cycle. There was also a manual facility which could raise, lower, squeeze and vibrate the tamping tines as individual operations. The vertical movement of the tamping tines could be controlled by proximity detectors on the lowering and lifting cylinders.

Tamping was only performed about the middle sleeper as the tamping bank could not be moved laterally. The middle sleeper was lifted by 20 mm to create

a space between it and the ballast and held at this height by clamping it to a cross beam. The 20-mm lift was chosen because a lift greater than 20 mm results in little additional improvement of ballast settlement as previously shown in Figure 2.7 (Selig and Waters, 1994). After that, the tamping tines were plunged into the ballast so that the bottom part of the tines was about 20 mm below the sleeper as shown in Figure 4.9. Then, the tines squeezed the ballast into the void by rotating around pivot points in the body of the tamping bank shown in Figure 4.10. This tamping process takes approximately 5 seconds starting from tine insertion until the tines are completely lifted off from the ballast layer.

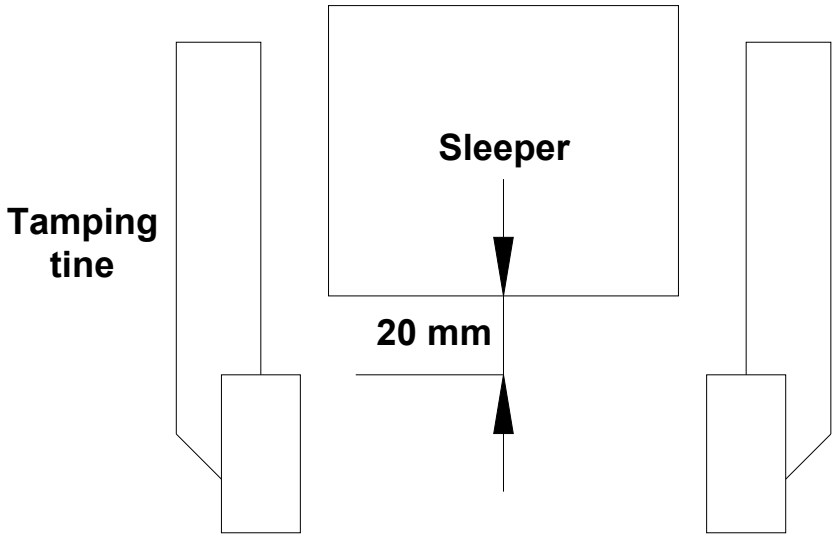

Figure 4.9. Tamping tine insertion

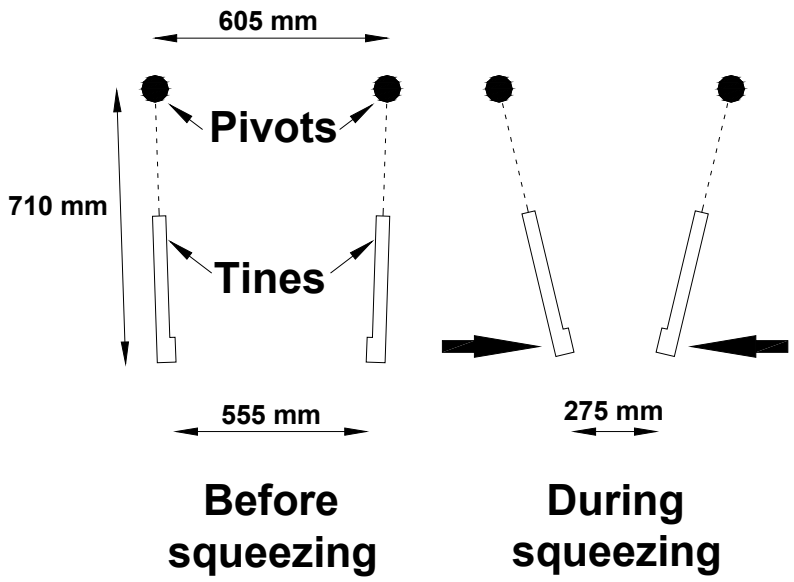

Figure 4.10. Tamping tine movement before and during squeezing

4.3. Instrumentation

The primary instruments used in the RTF were the three actuator load cells and integral stroke transducers to measure the load applied to the sleepers and average sleeper deflection respectively, displacement transducers to measure sleeper settlement and pressure cells to measure stresses near the top of the subgrade.

A secondary exercise was carried out to look at the feasibility of using an accelerometer to measure subgrade movement just below the ballast and to try and develop a means of collecting fines at the bottom of the ballast layer during a test. This will be described later.

The load cells and stroke transducers were fitted to the shafts of the actuators and were connected to the control system. Additionally, their outputs were

connected to an external data acquisition system with 100-Hz logging rate. It was also used to read the pressure cells and displacement transducers because there were insufficient channels on the control system for this purpose. The accelerometer output was monitored on a digital storage oscilloscope so that any extraneous high frequency signals could be seen but it could also be fed to the data acquisition system.

The pressure cells consist of a recessed disc with 65-mm diameter and 11-mm thickness. The bottom of the disc forms a 2-mm-thick diaphragm which has strain gauge in a Wheatstone bridge configuration. A voltage is applied across the bridge and pressure on the diaphragm causes a change in resistance of the gauge which can be used to give a voltage output proportional to the pressure. The cell is buried with the diaphragm upwards in the subgrade taking care that there are no stones in contact with the diaphragm and its cable run out of the surrounding material for accessibility as shown in Figure 4.11. The cells were installed 25 mm below the subgrade surface to measure vertical stress under the centre of the middle sleeper, under one loading point of the middle sleeper and between the sleepers as shown in Figure 4.12.

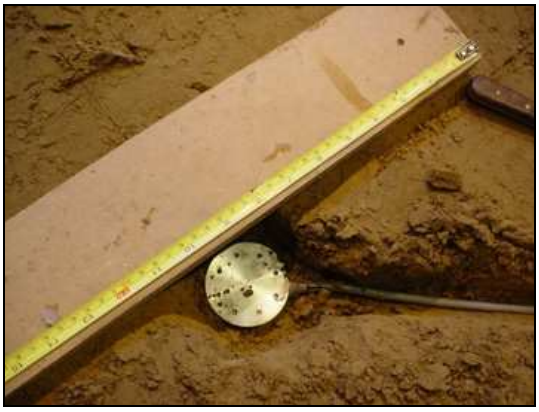

Figure 4.11. Pressure cell

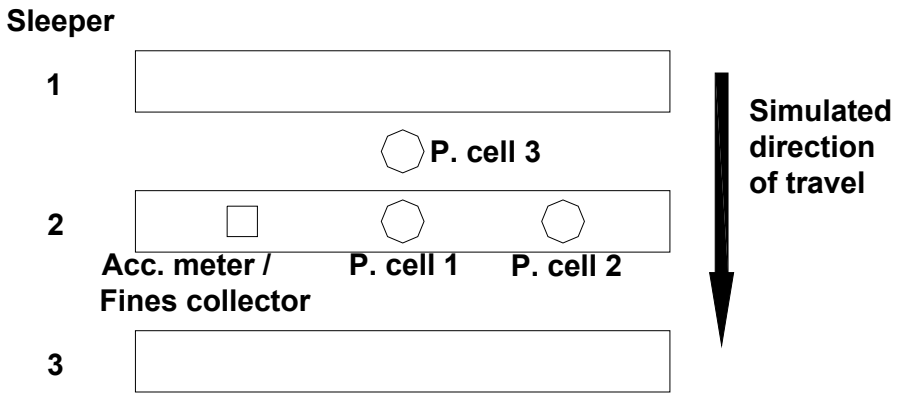

Figure 4.12. Positions of pressure cells, accelerometer, and fines collector

The central sleeper settlement for the first test was measured with a linear potentiometer placed at approximately 20 – 40 mm from the end of the middle sleeper by mounting onto a steel beam spanning over the pit so that the measured settlement was not affected by the movement of the loading system as shown in Figure 4.4. The potentiometer comprises a rod moving in and out of a case containing a resistor. The rod is connected to a wiper on the resistor which has a D.C. voltage applied to each end. As the rod moves the wiper along the resistor an output is obtained between the wiper and one end of the resistor which is proportional to the rod movement. This transducer was

replaced after the first test with two LVDTs (Linear variable differential transformer) displacement transducers, one at each end of the middle sleeper, which were more accurate. Each consists of a case containing primary and secondary windings with a ferrite core moving between the windings. The primary winding is powered with an A.C. voltage and when the core moves a voltage is induced into the secondary windings to give an output proportional to the position of the core.

An accelerometer, which had been used in another project for measuring the response of a pavement surface to an impact, was tried as a means of measuring dynamic subgrade deflection. This small device contains a quartz crystal under a small weight. When it moves, a force is exerted on the crystal which produces a charge. This can be converted to a voltage which is proportional to acceleration and when double intergrated should give a deflection reading. It is important that this type of device makes a solid mechanical contact with the material under the test so that it was fitted to a disc prior to compacting it into the subgrade. It was placed at the same level as the pressure cells but under the other end of the middle sleeper as shown in Figure 4.12 for the first two tests. However, the deflection reading obtained from the tests was many times higher than expected. On removal, the accelerometer was checked. It was noted that during handling of the connecting cable, a large signal occurred which was independent of the movement of the accelerometer. This may have been the problem as the signal obtained during testing was the correct frequency so it was possible that the cable was disturbed in phase with the loading by the actuator.

The accelerometer was replaced by a fines collector in the third test. It was a device that can weigh fines as the test was progressing, i.e. its function is different from the accelerometer. Figure 4.13 shows the top and side views of the fines collector. It was a 150 mm x 150 mm x 55 mm box buried in the subgrade. There was an 80 mm x 80 mm opening on the top lid of the box. A steel mesh with 5 mm x 5 mm aperture was bolted on to the top lid. Ballast fines could fall onto a rectangular tray inside the box through the mesh. The tray was supported by four springs at the four corners of the tray. An LVDT was attached to the middle of the tray and was connected to a multimeter outside the pit. As the fines fell into the tray, the multimeter could read the movement of the LVDT which then could be converted to the mass of the fines using a calibration factor based on this movement. However, it was found that it did not give realistic results probably due to electrical instability. It is recommended that the weighing tray needs to be guided in linear bearings to prevent tilt if the fines fall unevenly on the tray. Furthermore, the electrical supply and monitoring equipment for the fines collector needs to be very stable and the alignment of the cone in the LVDT must be effectively perfect. Both the accelerometer and fines collector required further development and this was not possible within the timescale of the project.

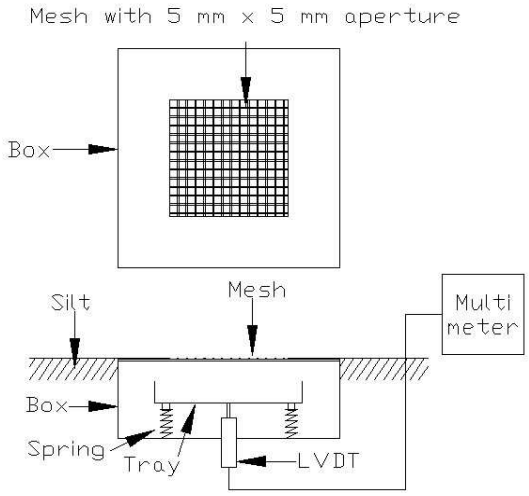

Figure 4.13. Fines collector

4.4. Installation of materials

4.4.1. Subgrade

Silt was chosen as the subgrade material because of its availability and ease of placing and compaction. It was obtained from a local gravel pit and was placed in the pit in the same condition when it arrived the laboratory. It was compacted in 180-mm layers using a plate vibrator to a depth of 900 mm so that there was enough space for ballast thickness of 300 mm under the sleepers which is the minimum ballast depth according to RT/CE/S/102 (2002). After placement, the subgrade was kept in the pit throughout the test programme. After compaction, it had a density of 1,770 kg/m^3 and a moisture content of 15.5 %.

The subgrade stiffness was measured by a Zorn ZGF-01 (also known in the UK as the 'German Dynamic Plate' or 'GDP') at several positions. The GDP is shown in Figure 4.14. It has an accelerometer at the centre of a loading plate.

The load is dropped three times onto a 300-mm diameter steel base sitting on the surface of the subgrade. The acceleration of the loading plate is measured and converted to the stiffness of the subgrade which is an approximation of the surface stiffness of the subgrade (Rahimzadeh et al., 2004). The stiffness was measured at twenty points on the subgrade as shown in Figure 4.15.

Next, the subgrade profile was measured with a rule up to a straight edge using the top of the pit as a datum as shown in Figure 4.16. Although it was difficult to obtain repeatable results due to some disturbance of subgrade between tests, it was concluded that the maximum settlement of the subgrade was about 0.4 mm and was negligible compared to the ballast settlement. Hence, the settlement from each test was predominantly in the ballast.

Figure 4.14. German Dynamic Plate measuring subgrade stiffness

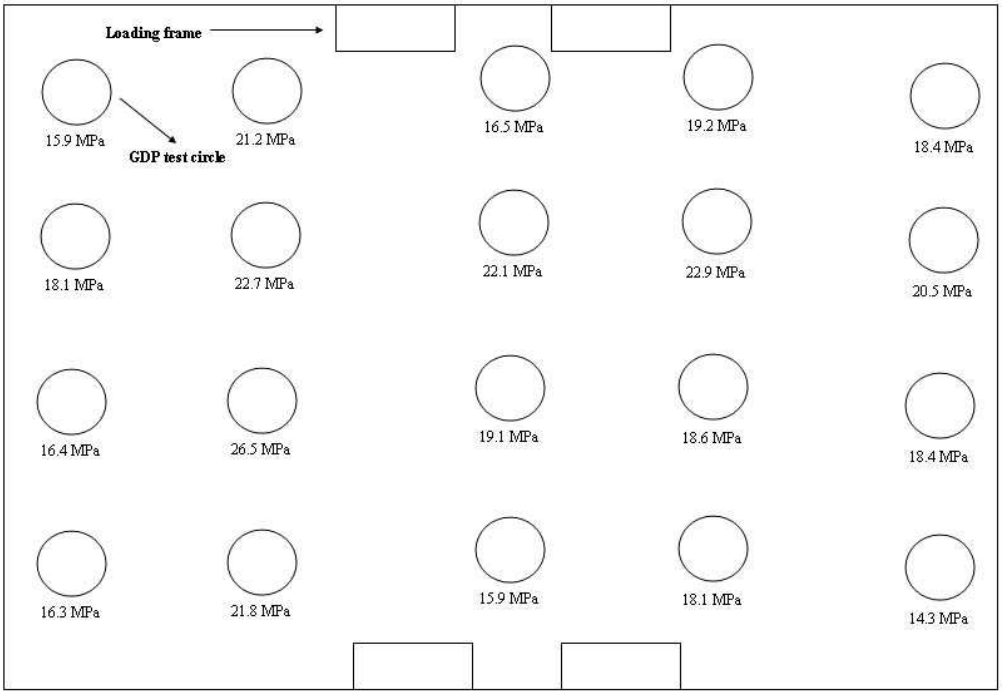

Figure 4.15. GDP sampling points

Moisture content of the subgrade at different depths was obtained by driving a 30 mm diameter, 900 mm long steel tube into the subgrade at two positions, one at each end of the pit, for confirmation. The subgrade from different depths was taken from the tube to find the moisture content. If the moisture content was different from the previous test, it would be restored by pouring the required amount of water, calculated from the known mass of subgrade, into the subgrade. A non-woven fabric, also known as geosynthetic, was placed on top of the subgrade to separate the subgrade and the ballast and to retain the fines from the ballast. This geosynthetic can also be used in the real track to separate the ballast and the underlying layer and prevent upward migration of particles into the ballast layer (GC/RT5014, 2003).

Figure 4.16. Measurement of subgrade profile

4.4.2. Ballast

The pit was then filled with ballast. From test 4 onwards, ballast particles at four critical positions were painted to ease the observation of degradation and sample collection. This is similar to the dyed ballast approach in the box tests in Selig and Waters (1994). The strengths of the painted ballast are statistically equal to the normal ballast according to the single particle crushing test (Section 3.3.4). These sampling points are called Traffic, Squeezed, T1 and T2. Their positions are shown in Figure 4.17. The traffic sampling point was underneath the right rail seat of the middle sleeper. T1 and T2 sampling points were located under one pair of tamping tines. The squeezed sampling point was where the other pair of tamping tines squeezed. The particles were placed in the sampling points using 100 mm deep by 300 mm diameter tubes. To fill the other places in the pit with ballast, large bags of ballast, hoisted over the pit by

a crane, were cut in the form of a flap to let the ballast fall into the pit. The ballast was placed and compacted in 100-mm layers by the same plate vibrator to a depth of 300 mm. The tubes were removed before each compaction. The approximate amount of ballast was 4,500 kg for all tests resulting in ballast density of 1,742 kg/m^3.

Care was taken to ensure that the ballast under the rail seats was slightly higher than under the centre of the sleeper. A straight edge was used to get the ballast as level as possible before placing the three sleepers. They were placed lengthways with 650-mm spacing centre-to-centre. If the sleepers were rocking, they were then lifted and the ballast high spots were levelled. The sleepers were repositioned and checked for stability. A vibrating chisel was then used to settle the ballast material under the sleeper by working it in from the sides and ends of the sleepers. The depth of the ballast and the sleeper spacing were chosen to reflect the current UK practice (RT/CE/S/102 Issue 5, 2002). The sleepers used in the RTF were G44 sleepers. This type of sleeper is used in the mainline track nowadays. The dimensions of the sleeper are shown in Figure 4.18.

Then, more ballast was added to fill up the pit as shown in Figure 4.19. Two thin wire ropes were used to prevent tilting of the sleepers and link the sleepers and the frame together. This was to maintain the positions of the sleepers during installation and testing. The ropes had sufficient slack to allow vertical movement so that they would not restrain the settlement of the sleepers during

the test. However, it was found in the first test that they could not prevent tilting of the sleepers so they were not used in the later tests.

It should be noted that the ballast compaction method in the RTF was different from the normal procedure on site. In a real track, ballast is compacted by a dynamic track stabiliser which applies horizontal vibration and static vertical load to the track while running on the track (Selig and Waters, 1994). This method might break the ballast in the track. The plate vibrator was therefore a preferable choice for compacting the ballast in the RTF as it was much less likely to break the ballast. Furthermore, this method was easy and convenient and did not require any sophisticated equipment.

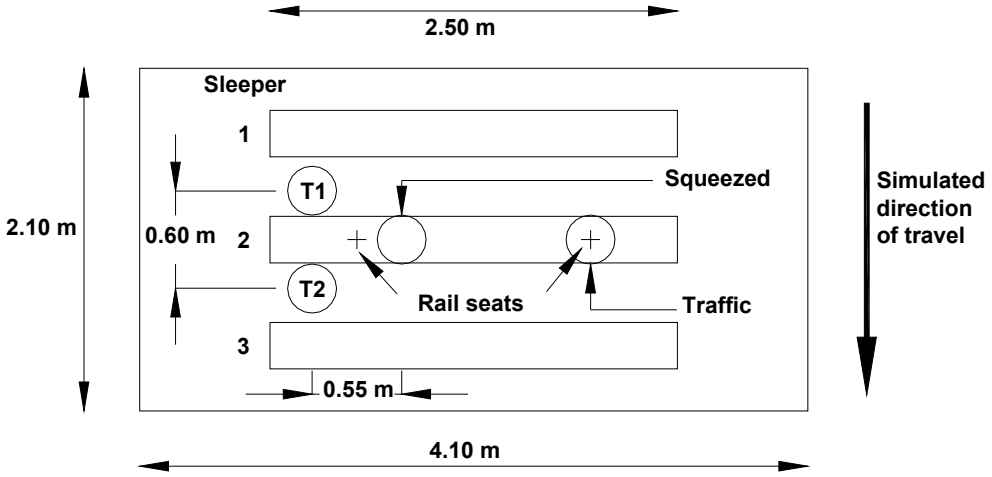

Figure 4.17. Ballast sampling points

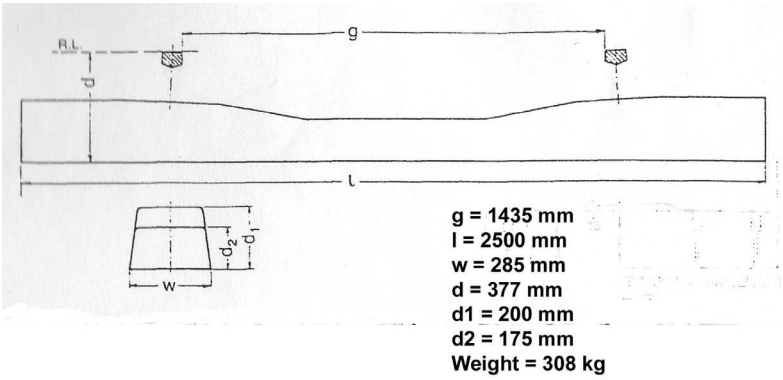

Figure 4.18. Dimensions of a G44 sleeper

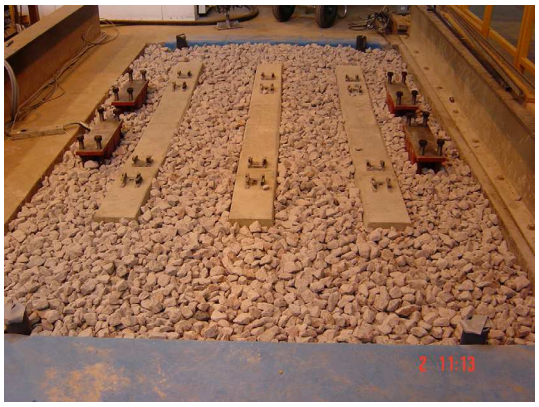

Figure 4.19. Sleeper arrangement in the RTF

The arrangement of the track bed material in test 7 was different from the others in that concrete slabs were placed on the subgrade to provide a stiff support to the ballast. The subgrade surface and sides of the pit were also covered with polythene so that water could be added to the ballast. This was because it was believed that a stiff subgrade and water would increase the amount of breakage from the test. As a result, the ballast thickness under the sleepers was 200 mm in test 7. It should be noted that the use of polythene might affect the ballast settlement in the test.

4.5. Test procedures

After the installation of the ballast and the sleepers, the facility was assembled as shown in Figure 4.4. The sleeper height was such that the actuator stroke had a remaining travel of about 70 mm at the start of loading to ensure sufficient movement to accommodate the expected settlement.

In general, a million cycles of traffic loading were completed and then three tamps were carried out by the tamping bank either side of the rail seating at one end of the middle sleeper. However, in two tests, a tamp around each end of the middle sleeper was performed halfway (after 500,000 cycles) followed by the usual three tamps around one end of the middle sleeper after one million cycles. According to Key (1998), one million cycles of traffic is approximately equivalent to a year of trafficking.

Before the cyclic loading began, each sleeper was held at 1 kN load to ensure that it was in contact with the actuator. Then, the readings from the actuator stroke transducers and the LVDTs at both ends were recorded at this initial position. The test was stopped after cycles 100; 1,000; 2,000; 5,000; 10,000; 20,000; 50,000; 100,000; 150,000; 200,000; 250,000; 300,000; 400,000; 500,000;…; and 1,000,000 to record the readings at 1 kN. These positions readings were then used to calculate the settlement. The pressure cell readings were also taken just before completing the above numbers of cycles. It should be noted that the dynamic movement of the loading frame would not affect the settlement reading because each reading was taken when the sleepers were held at 1 kN.

After each test, the ballast for all sampling points was taken for analysis. The tubes which were used to place the painted ballast were used again during sampling by placing them on top of the sampling points. The painted ballast inside the ring was picked out by hand, and the ring was pushed down as the painted ballast was collected until the bottom was reached. During sampling, some of the ballast outside the ring was disturbed and would fall into the ring. This was not collected as the dyed ballast distinguished between the ballast inside and outside the sampling points.

As the breakage from tamping after traffic loading was not as high as expected, due to a suspected lack of ballast confinement, i.e. too much space for ballast to move around to avoid the damage from tamping and low horizontal stress. Therefore, an additional test with extra confinement on limestone was setup for tamping after test 7. No trafficking was performed in this test. A box was formed at the end of the pit near the tamping bank as shown in Figure 4.20. The steel walls were wedged against both sides of the pit to prevent them from moving. The width and length of the box were 990 and 1,240 mm. The ballast was placed in the box by the same method except that the depth of ballast changed from 300 mm to 445 mm due to the large subgrade settlement in test 7 (see Section 4.7.3 for more details). After that, the sleeper was placed on top of the ballast. One end of the sleeper was supported by the ballast in the box while the other end was placed on a steel beam outside the box. Then, the ballast was added to fill up the box. The tamping bank was then brought into position and the sleeper was held by clamping to the cross beam. There was no space

between the ballast and sleeper in this test. Three tamps were performed and the painted ballast was taken for sieve analysis after the tamping. After the sieve analysis, each sample was placed back in the box with particles smaller than 22.4 mm removed. The same test setup was built again and ten tamps were performed this time. This was to observe the development of breakage under different number of tamps. It should be noted that during the ten tamp test, the tamping bank cannot squeeze the ballast after five tamps. This is because the ballast in the squeezed location became so compacted that it prevented the squeezing operation. The squeezing pressure was then increased to achieve successful squeezing after the fifth tamp.

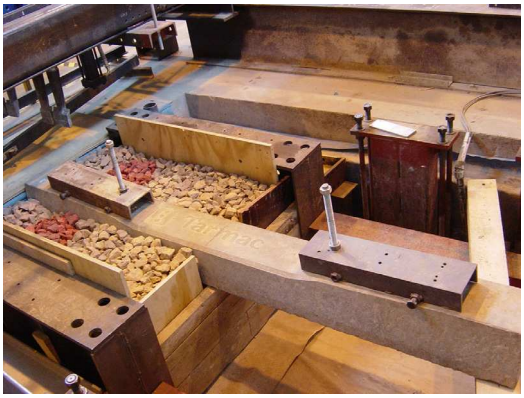

(a)

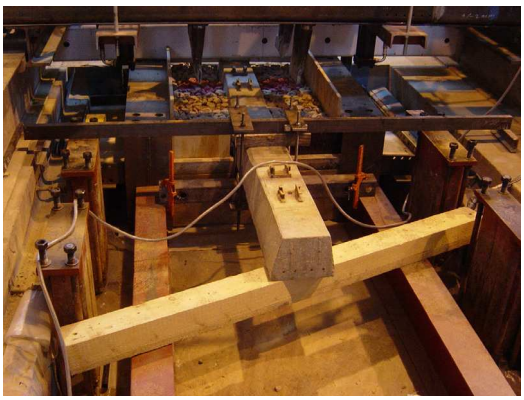

(b)

Figure 4.20. Setup for extra confinement tamping test

4.6. Test Programme

Seven tests were performed in the RTF. The first four were the joint tests with the geogrid project (Kwan, 2006). A geogrid was placed at 50 mm above the bottom of ballast layer in test 2 and at the bottom of ballast layer in test 3 to see the effect of geogrid position on settlement. The tests are listed in Table 4.1.

The effect of ballast type and subgrade stiffness on settlement and degradation would be examined from the tests in the table. Repeatability of the test can be checked during the first 500,000 cycles of tests 1 and 4 (without geogrid) and tests 2 and 3 (with geogrid) as the same procedure was carried out for all of them up to this point.

Test No.	Description	Intermediate tamping after cycle*	Final tamping after cycle**
1	Granite A	N/A	1,000,000
2	Granite A + Geogrid at 50 mm above bottom of ballast	N/A	1,000,000
3	Granite A + Geogrid at bottom of ballast	500,000	1,000,000
4	Granite A	500,000	1,000,000
5	Granite B	600,000***	1,000,000
6	Limestone	N/A	1,000,000
7	Limestone + concrete slab base	N/A	320,000****
T	Tamping with extra confinement but without trafficking+	N/A	N/A

* One tamp at each end of the middle sleeper

** Three tamps at one end of the middle sleeper

*** Hand tamp under the rail seat, see section 4.7.2

**** Test was stopped due to excessive settlement

+ Three tamps followed by ten tamps

Table 4.1. List of tests on the RTF

4.7. Results

4.7.1. Subgrade Stiffness and Moisture Content

Figure 4.21 shows subgrade stiffness values and moisture contents for the tests in the RTF. The subgrade stiffness after test 7 could not be measured because concrete slabs were used as the base.

The increase in moisture content for test 7 was associated with water which was added to the ballast finding a way through the polythene above the subgrade. This is discussed in Section 4.7.3.

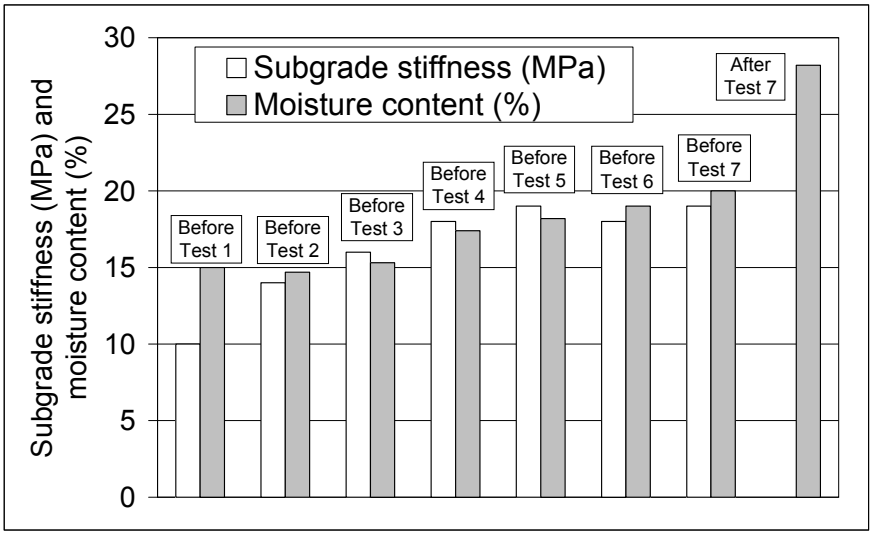

Figure 4.21. Subgrade stiffness and moisture content

4.7.2. Vertical stress on subgrade

Figure 4.22 shows the average vertical stress reading from the pressure cells for tests 1 to 6 for the first and last 500,000 cycles. There were no results from test 7 because the pressure cells could not read the vertical stress due to the presence of the concrete slabs under the ballast. The distribution of the vertical

stresses due to the loading depends on the way in which the sleeper is seated on the ballast and the compaction of the ballast. The procedure for placing the sleepers is described in Section 4.4.2 and this method was used for consistency. However, from analysis of the subgrade stress readings, it can be seen that the location of the highest stress varied from test to test. To be representative of the site condition, the highest stress should be below the rail seating as the ballast will be raised at the position during sleeper installation and tamping. It can be seen that this is not the case for tests 2, 4, and 5.

The vertical stress under the rail seat for test 5 was found to be particularly low. After 600,000 cycles, the middle sleeper was lifted and the ballast under both rail seats was re-compacted by using a vibrating chisel to push it under the sleeper. This was to increase the vertical stress under the rail seat as this should increase the degradation due to traffic loading. The effect of the ballast compaction is shown in Figure 4.23. It can be seen that the stresses under the centre and between sleepers drop after the compaction and quickly rise afterwards. On the contrary, the stress under the rail seat rises and drops below the stress under the centre. This shows that the re-compaction by this method only gave short term benefit and the sleeper resettled. It would be recommended in future work that the ballast under the sleeper at the rail seating should be at a slightly higher level than under the middle portion of the sleeper.

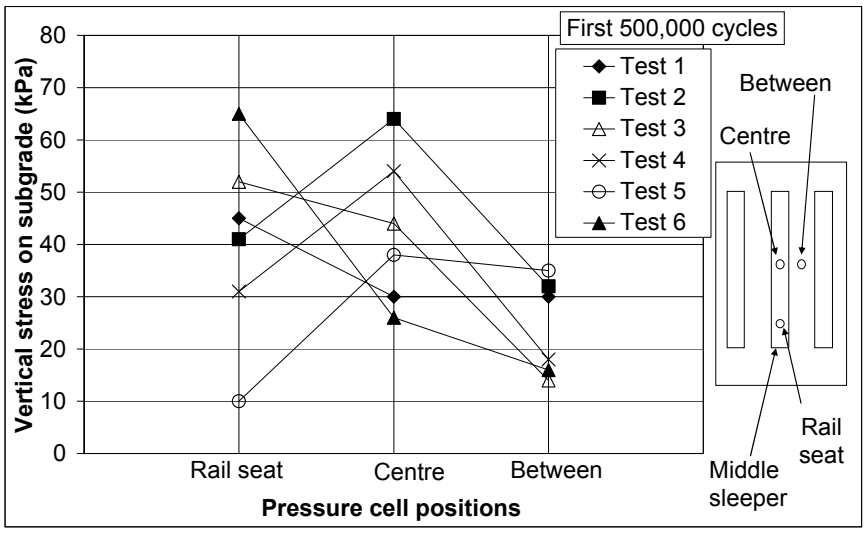

Figure 4.22(a). Average vertical stresses on subgrade for the first 500,000 cycles

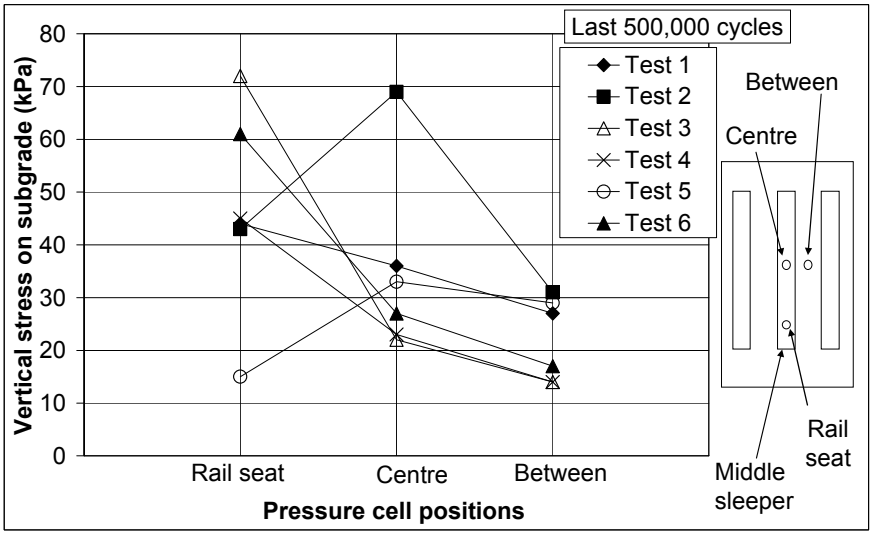

Figure 4.22(a). Average vertical stresses on subgrade for the last 500,000 cycles

Figure 4.22. Average vertical stresses on subgrade at different positions for the first 500,000 cycles (a) and last 500,000 cycles (b)

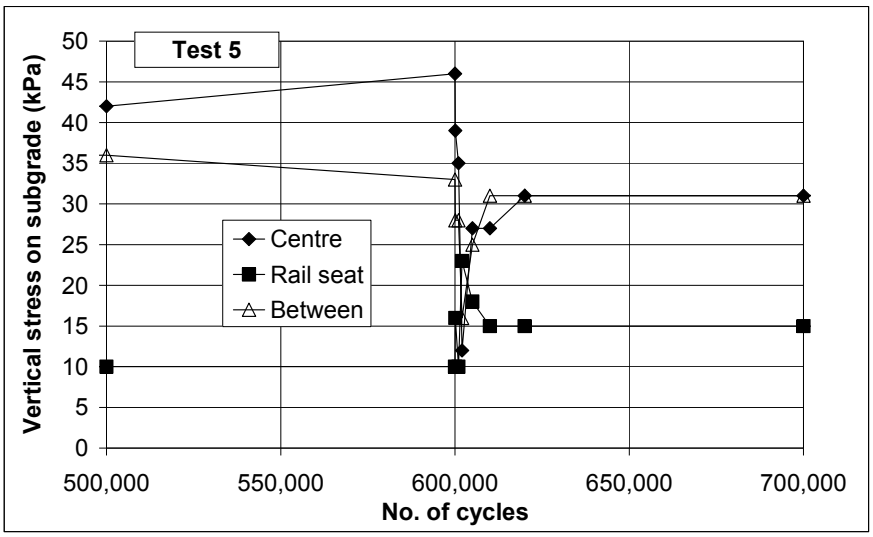

Figure 4.23. Effect of ballast compaction after 600,000 cycles in test 5

4.7.3. Settlement

Figure 4.24 shows the settlement from tests 1 to 7. The potentiometer was used to measure settlement of the middle sleeper in test 1 and was replaced by the two LVDTs in the other tests as mentioned earlier. The settlements of the middle sleeper of tests 1 to 6 are plotted together in Figure 4.25.

The small variations in the accumulated settlements were usually due to an occasional adjustment of the spreader beams or the packing to compensate from some tilting of the sleepers during the tests. However, the major downward shifts in settlement of tests 3 and 4 were because the middle sleeper was lifted by 20 mm to allow for tamping at the halfway stage of the tests. Consequently, when loading was recommenced, there would be a large settlement as the ballast had been loosened by the tamping. It was not planned to tamp at the midpoint of test 5 but as mentioned in Section 4.7.2, a hand tamp was carried out at 600,000 cycles. In this case, the sleeper was lifted by the

hand tamping by 8 mm and a large settlement reading was obtained when loading was restarted.

In test 6, a fault on the load cell from actuator 3 prevented this component from working from 400,000 cycles onwards so there was no data from Pos 3 after this point. In test 7, the settlement readings were progressing as expected up until approximately 150,000 cycles. As water had been added to the ballast and the foundation was rigid, it was expected that degradation and settlement would increase and this appeared to be the case. However, the settlement rate increased rapidly to an excessive level and the test was stopped.

It was subsequently found that the water had penetrated the water proofing and washed down silt in the corners of the pit as shown in Figure 4.26. Although not excavated, it was suspected that the silt could migrate into the void below the test frame at the bottom of the pit. The level of the silt beneath the slabs was found to be lower in the loaded area and although the slabs had been cemented at the joints, this was not sufficient to tie them together. It appeared that the silt had squeezed out at the sides and ends so that the central slab settled and the outer slabs tilted down towards the central slab. Figure 4.27 shows the level of the subgrade before and after test 7. The subgrade level was measured along the position of the three sleepers throughout the length of the pit by using the rule as explained in Section 4.4.1. Before the test, the subgrade level was 560 mm below the top of the pit. It can be seen that the subgrade level changed significantly after the test. The big drop in the subgrade level at both ends was a result of the collapsed corners as shown in Figure 4.26.

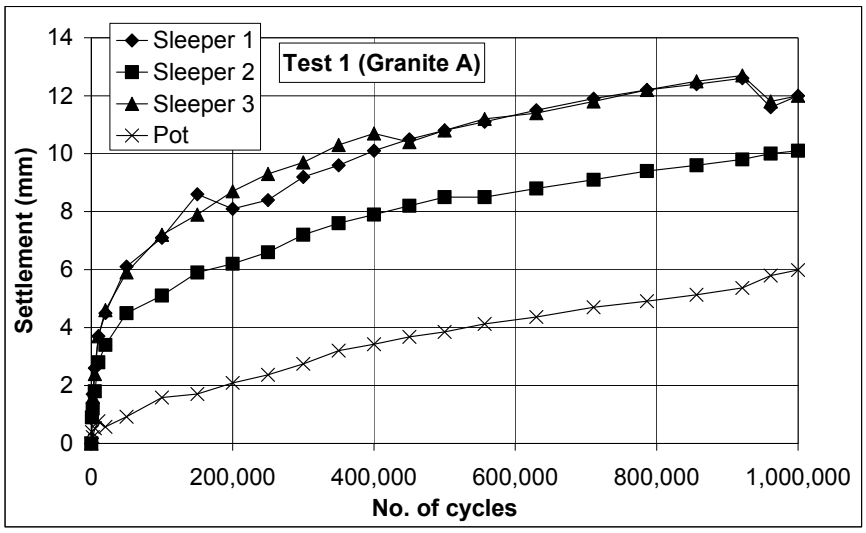

Figure 4.24(a). Settlement from test 1 (granite A)

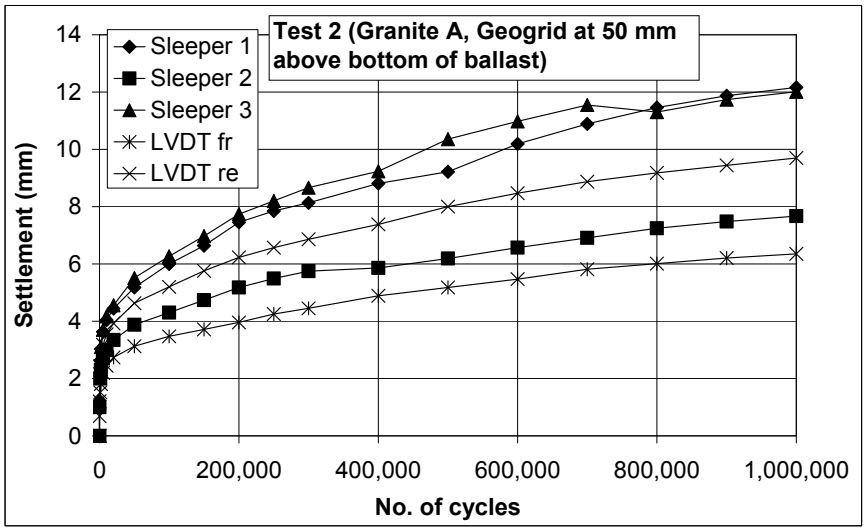

Figure 4.24(b). Settlement from test 2 (granite A, geogrid at 50 mm above bottom of ballast)

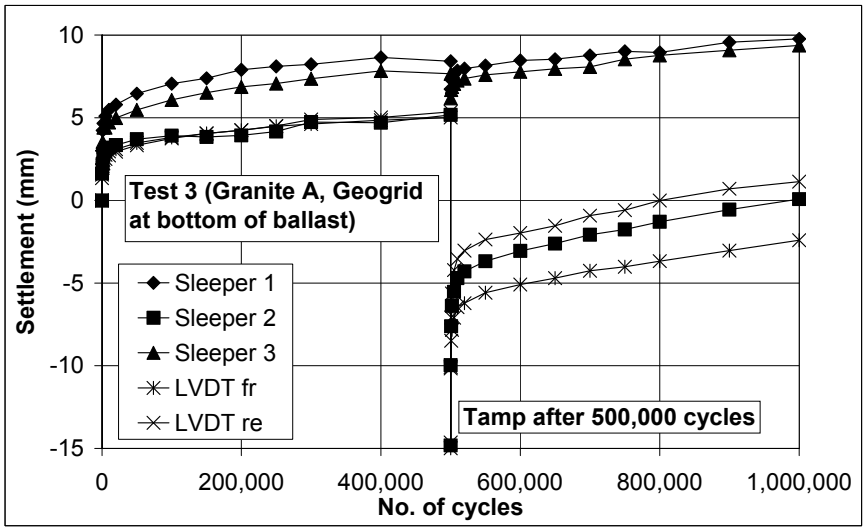

Figure 4.24(c). Settlement from test 3 (granite A, geogrid at bottom of ballast, tamp at halfway)

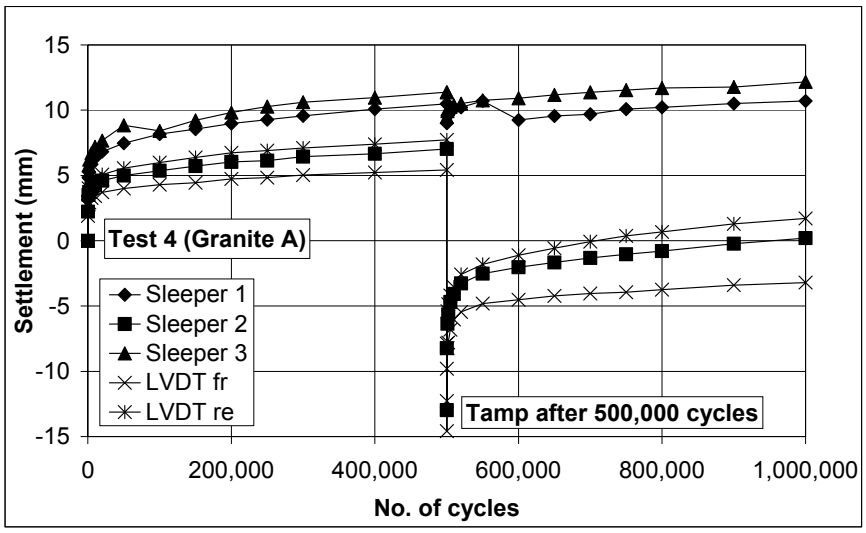

Figure 4.24(d). Settlement from test 4 (granite A, tamp at halfway)

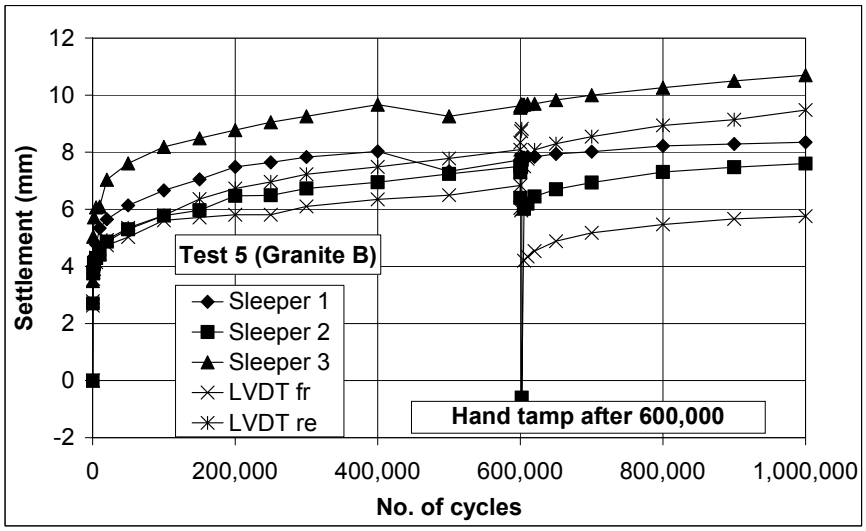

Figure 4.24(e). Settlement from test 5 (granite B)

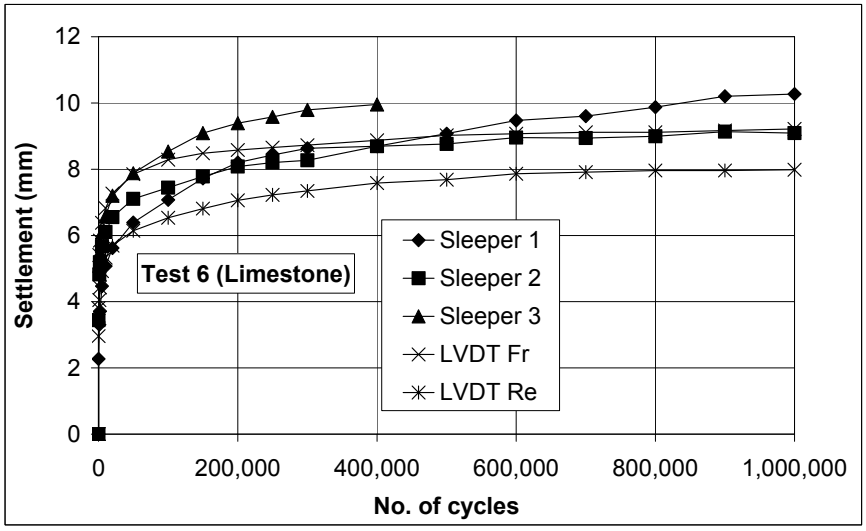

Figure 4.24(f). Settlement from test 6 (limestone)

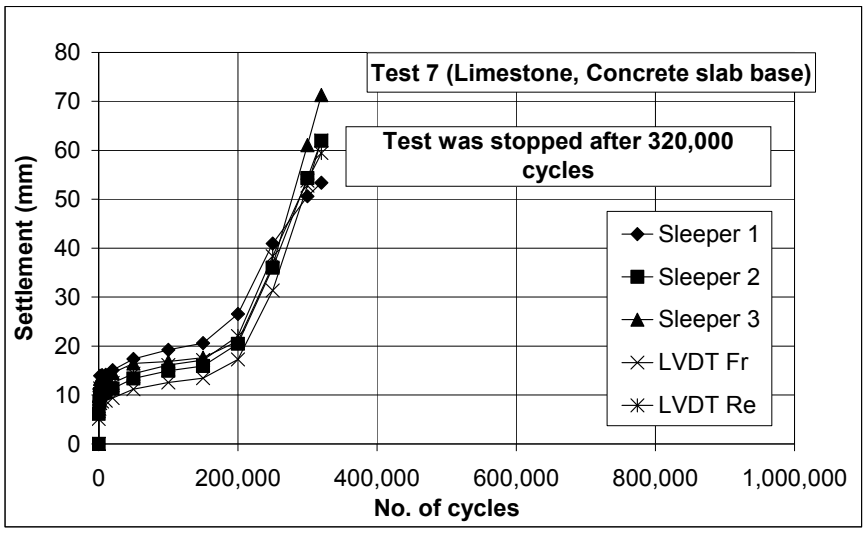

Figure 4.24(g). Settlement from test 7 (limestone, concrete slab base)

Figure 4.24. Settlements from RTF (a) – (g)

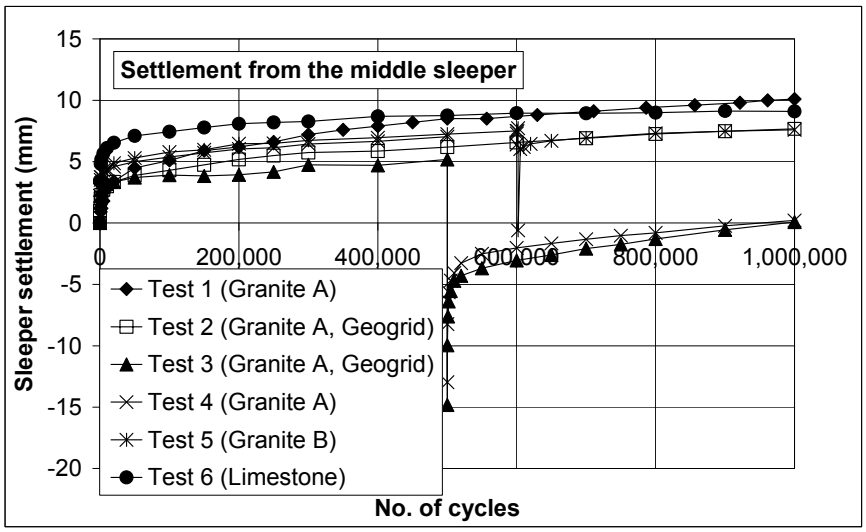

Figure 4.25. Settlements of middle sleeper from tests 1 to 6

As water was added during the testing, the early part of the test (up to 50,000 cycles) should be valid as the washing out process would not occur immediately. By measuring down to the slabs after the test, it was calculated that on average of about 20 mm of settlement had occurred in the ballast at the rail seating location for the central sleeper.

Figure 4.26. Collapsed corner

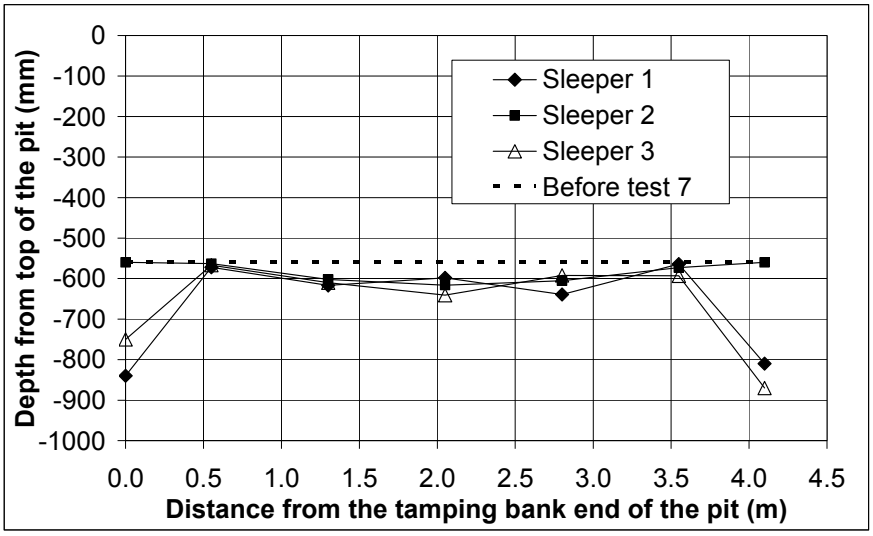

Figure 4.27. Level of subgrade before and after test 7

The following points can be drawn from Figure 4.24.

- The settlement from the middle sleeper is always smaller than the other two. This might be due to the boundary effect between the walls and the ballast i.e., low shearing resistance between the wall and the ballast. However, the middle sleeper should be unaffected as it is adequately far away from the pit walls.

- Tamping causes a faster rate of settlement ((c) and (d)). This matches the findings in Section 2.2.3.
- The settlement from Pos 2 is approximately the average between the settlements from both LVDTs. This is because the middle sleeper tilted during the tests.
- The settlements of different ballast are similar to each other (h).
- Field data from Federal Railroad Administration Research Track (FAST) in Selig and Waters (1994) showed 17 mm of settlement after the same amount of traffic. Therefore, the settlements obtained from the tests were about 60 % of the settlement that would be expected on site. This might be due to the large dynamic load on site. However, it should be noted that Selig and Waters (1994) did not report test parameters such as track condition, train speed, ballast type, or ballast density. Hence, the test results might not be compared on the same basis.
- Tests 1 and 4 (granite A without geogrid) show good repeatability of the first 500,000 cycles. For easier observation, the settlements from the middle sleeper of tests 1 and 4 are shown in Figure 4.28.
- According to Kwan (2006), the geogrid reduced the total settlement of 10.1 mm in test 1 (unreinforced) to 7.7 mm in test 2 (reinforced). However, in tests 3 and 4 where tamping was performed halfway, the post-tamping settlement in test 4 (unreinforced) is smaller than test 3. This is likely to be due to a tilt of the middle sleeper, observed visually during tamping.

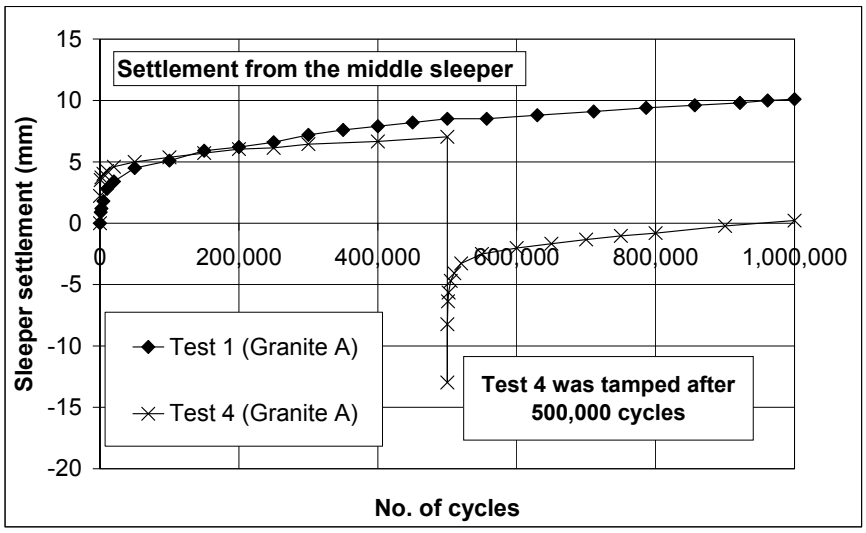

Figure 4.28. Repeatability of settlements

4.7.4. Ballast degradation

It could be seen from each test that more significant damage occurred from plunging the tamping tines into the ballast. Large broken particles were usually found in the sampling points where the tines plunged into ballast (T1 and T2) shown in Figure 4.17. Particle abrasion (scraped or scratched surface) was usually found in the location subject to the squeeze of tamping tines and traffic loading. The breakage is shown in Figure 4.29.

(a) Tine insertion (b) Squeezing and traffic loading

Figure 4.29. Particle breakage from RTF from different types of damage

The ballast degradation from each test is shown by particle size distribution of particles smaller than 22.4 mm in Figure 4.30. Similarly, the breakage from each sampling point is shown in Figure 4.31.

Only the results from test 4 onwards are shown because the system of painted ballast without particles smaller than 22.4 mm was used after the development in the first three tests. Furthermore, the particle size distribution is shown in terms of mass passing instead of the usual percentage passing. This is because not all particles in the sampling points are damaged from trafficking, tine insertion, or squeezing mechanisms. As percentage passing is calculated from the total mass of ballast in each sampling point, the mass of the undamaged ballast would be included in the calculation and the percentage of small particles can be negligibly small. It should be noted that as test 4 was tamped halfway, it had one extra tamp at each end of the middle sleeper.

The following points can be drawn from the degradation results.

- Traffic loading and squeezing action of the tines generally produce similar amount of degradation and cause lower degradation than tine insertion.
- Degradation of granite B in traffic and squeezed samples is greater than the other two ballasts. This is probably because the flat and long shape of granite B.
- Test 7 does not have more fines than test 6. It seems that the increased stiffness from the concrete slab base does not increase the amount of degradation as expected.

- The degradation from T1 and T2 samples is always greater than Traffic sample except test 4 (Figure 4.30a). This might be because of the extra tamp at the trafficked end.
- Even the degradation from ten tamps in test T (extra confinement tamping on limestone) is smaller than test 6 (limestone).

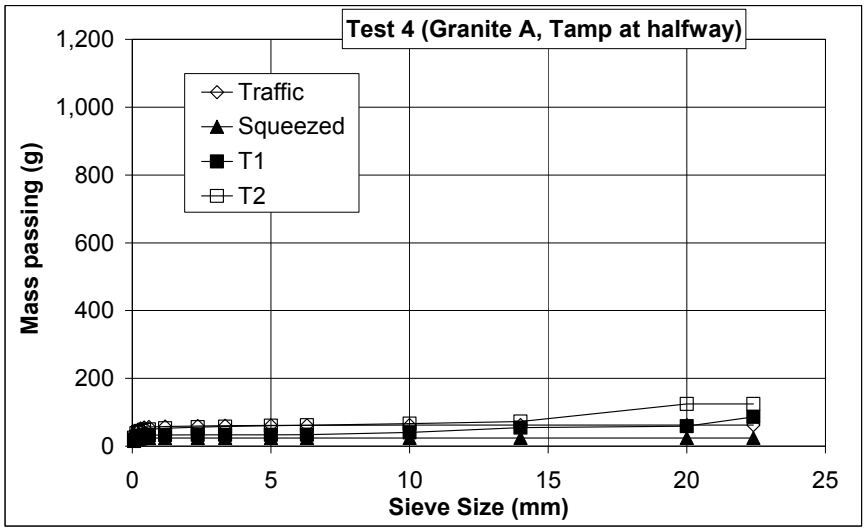

Figure 4.30(a). Particles smaller than 22.4 mm from test 4 (granite A, tamp at halfway)

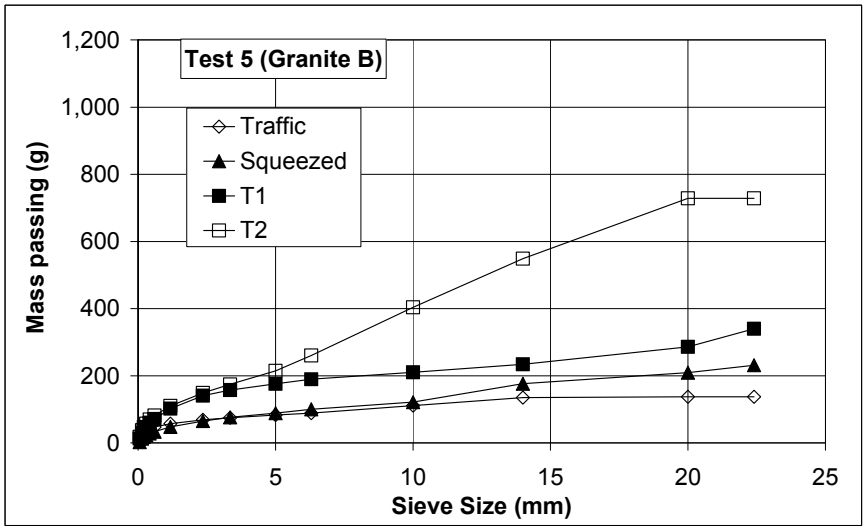

Figure 4.30(b). Particles smaller than 22.4 mm from test 5 (granite B)

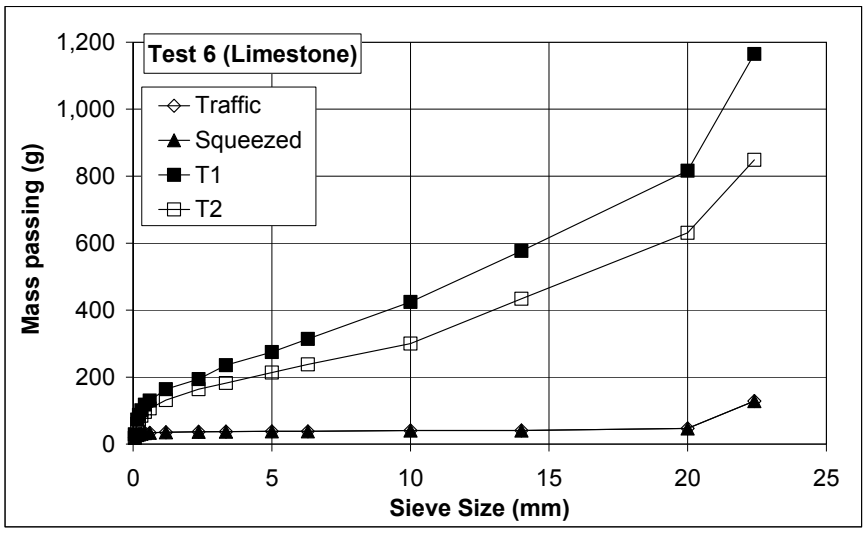

Figure 4.30(c). Particles smaller than 22.4 mm from test 6 (limestone)

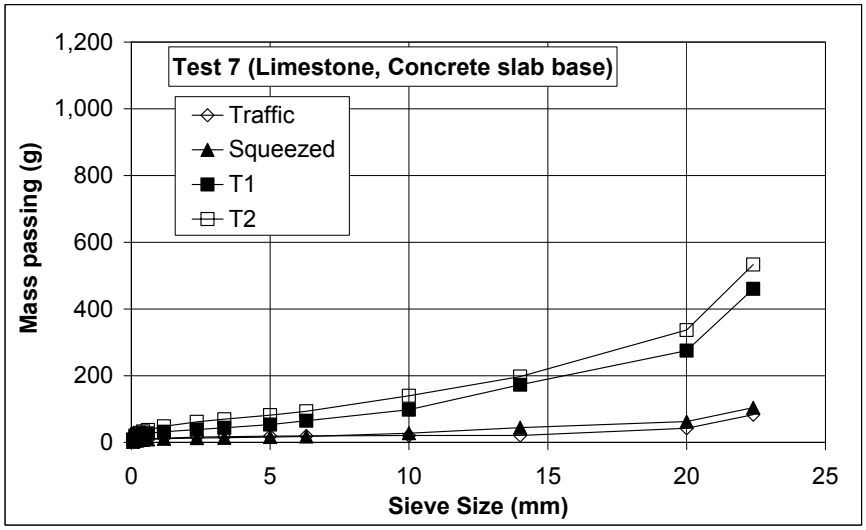

Figure 4.30(d). Particles smaller than 22.4 mm from test 6 (limestone, concrete slab base)

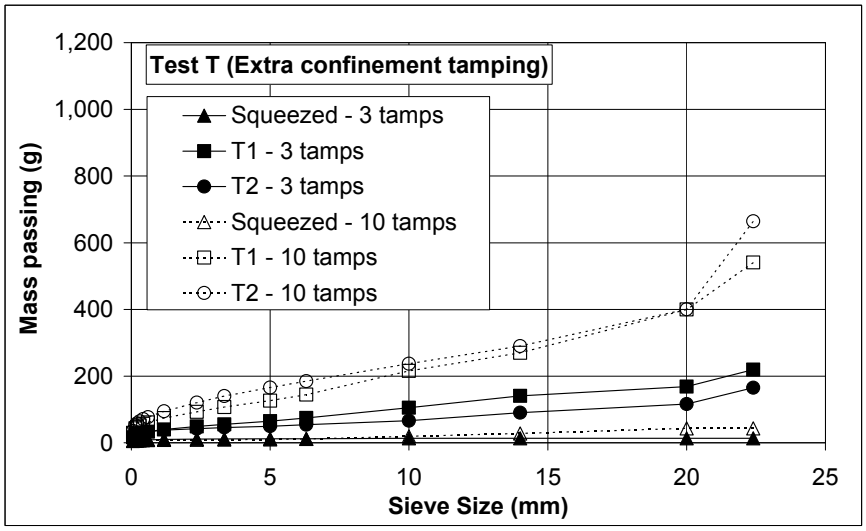

Figure 4.30(e). Particles smaller than 22.4 mm from test T (Extra confinement tamping)

Figure 4.30. Particles smaller than 22.4 mm from tests 4 to 7 and T (a) – (e)

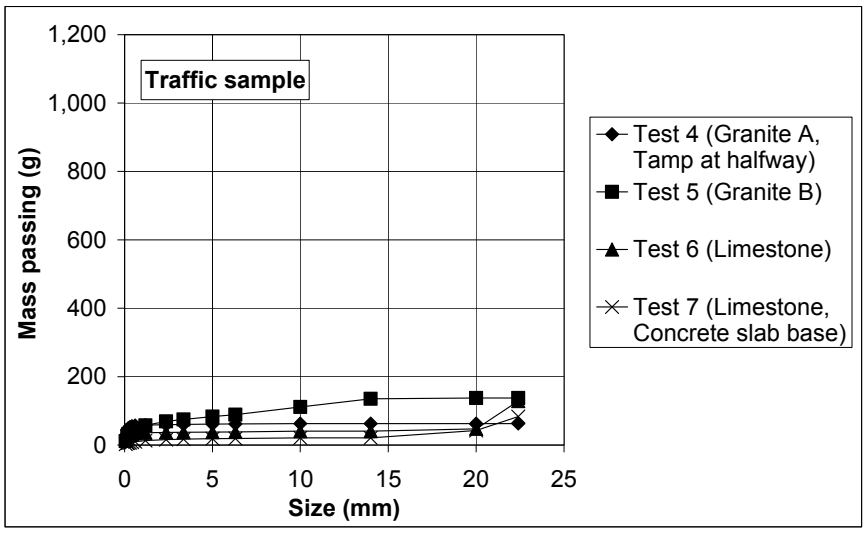

Figure 4.31(a). Particles smaller than 22.4 mm of Traffic sample

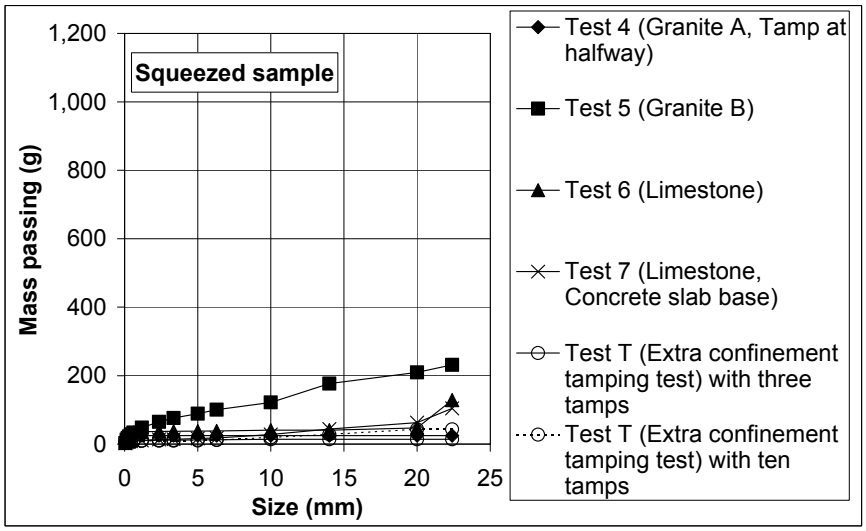

Figure 4.31(b). Particles smaller than 22.4 mm of Squeezed sample

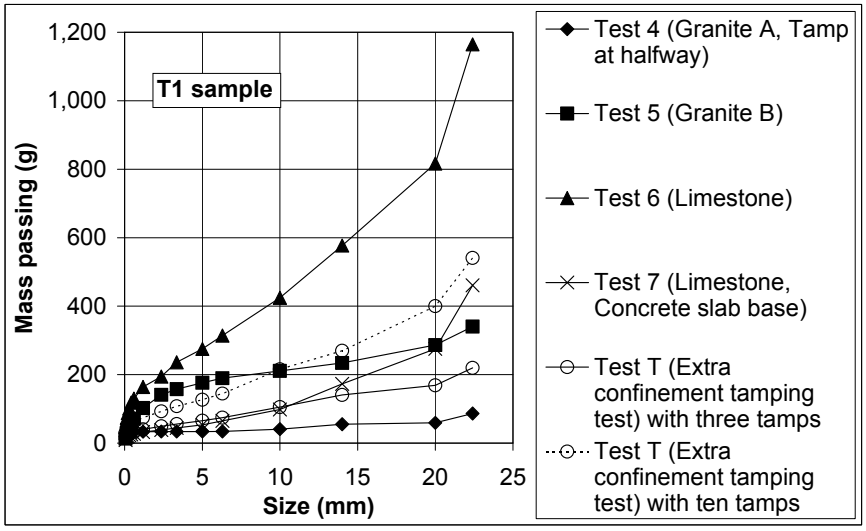

Figure 4.31(c). Particles smaller than 22.4 mm of T1 sample

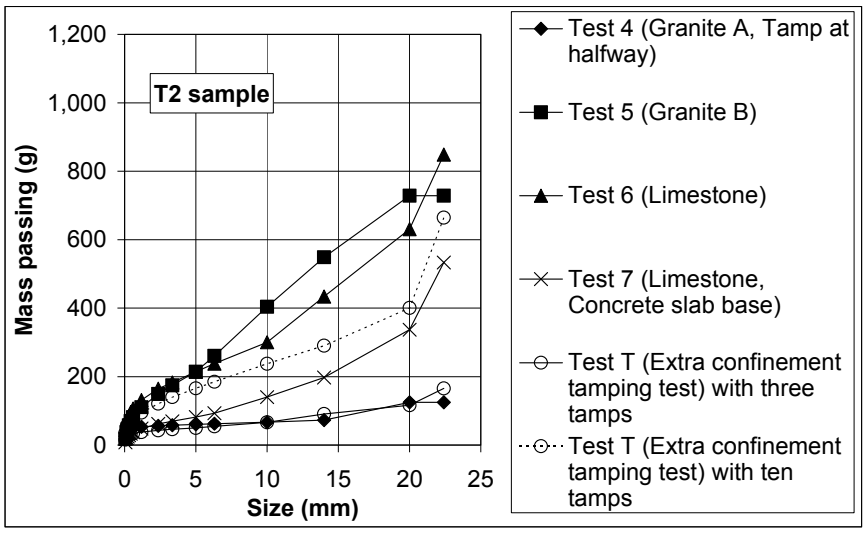

Figure 4.31(d). Particles smaller than 22.4 mm of T2 sample

Figure 4.31. Particles smaller than 22.4 mm from each sampling point (a) – (d)

4.8. Discussion

The actuators in the RTF simulated the axle load of 20 tonnes. Even though the magnitude of this axle load is comparable to a typical heavy axle load, this is just the static component of the vertical load in the track. According to Selig and Waters (1994), the dynamic load in the track can be more than twice the static load. To simulate the worst case scenario, the simulated load in the RTF should be larger. Another point that should be noted regarding the capacity of the actuators is the loading frequency that simulated the train speed. The simulated train speed in the RTF was 28 km/h which was very low and unrealistic. In the real track, higher loading frequency or train speed causes larger dynamic load due to track geometrical irregularities and wheel impact (Selig and Waters, 1994). However, this was not present in the RTF because of the constant magnitude of traffic loading. Furthermore, frequency has no effect on the cyclic triaxial test results of ballast according to Shenton (1974).

Therefore, it can be concluded that the low and unrealistic simulated train speed of the RTF had no effect on the test results as the dynamic components of loading is not presented.

The maximum amounts of particles passing 14 mm produced from traffic loading in the RTF is 135 g. The maximum amount of particles passing 14 mm from traffic loading of Awoleye (1993) was 96 g. This is of comparable magnitude with the amount obtained from the RTF. However, it should be noted that Awoleye (1993) performed the test using a half-sleeper rig in a box measuring 900 mm x 402 mm x 150 mm which is smaller than the size of the RTF. Furthermore, he did not compact the ballast but carefully placed it in the box instead. This resulted in ballast density of approximately 1,400 – 1,470 kg/m^3 which is smaller than the predicted ballast density in the RTF.

The maximum amounts of particles passing 14 mm produced from tamping from all tests is 548.5 g. However, the amount of particles passing 14 mm from tamping contradicts with Wright (1983). The maximum amount of particles passing 14 mm from ten tamps of Wright (1983) was approximately 40 kg. This was approximately 4 kg per tamp. This contradiction was initially thought to be due to the void between the ballast and sleeper and lack of ballast confinement in the RTF. This is because the system in Wright (1983) had no void underneath the tamped sleeper and had a restraint on top of the tamped sleeper provided by the weight of the tamping machine (approximately 35 tonnes) through a pair of rails according to Mr. Eric Hornby (Hornby, 2007) who is the principal technical officer of the company who modified and

maintained the tamping facility for Wright (1983). However, the degradation from the extra confinement tamping test in the RTF was smaller even with ten tamps.

As a result, some more consideration was given to try and understand where the differences between the test in the RTF and the test in Wright (1983) arose. The major differences were the restraint on the tamped sleeper and the mechanical means of generating vibration.

The RTF was supported by a reaction frame which was clamped to the side beams fixed to the laboratory floor. So it was necessary to hold down the sleeper at positions either side of the sleeper with beams which spanned the pit and were held by jacks against the side beams as shown in Figure 4.32. On the contrary, the system in Wright (1983) had a large mass to react against and this may direct the force from the tamping bank more effectively into the ballast compared to the lighter frame for the RTF. Furthermore, the frame arrangement used to the RTF tamping bank is not as heavy as the tamping facility in Wright (1983) so some of the vibration may be transmitted into the lighter frame.

Figure 4.32: Sleeper restraint in the RTF

However, the different ways of producing vibration probably have more significance with regard to the amount of damage to the ballast. The mechanical system which is used in Wright (1983) and the real tamping maintenance is only capable of producing a fixed amplitude of vibration and so will be more damaging to the ballast when the ballast resistance to penetration increases due to ballast compaction (Hornby, 2007). On the other hand, the hydraulic method of developing vibration of the RTF may result in a decrease in amplitude if the tines meet a high level of resistance during insertion and especially during squeezing. This is because the resistance of the ballast can overcome the forces generated by the vibrating cylinder. This reason can also be used to explain the small degradation from the extra confinement test. As the ballast is more confined in a small space, the amplitude of the vibration of the tamping tines may decrease resulting in less breakage. This type of vibrator may be advantageous as it is less likely to damage the ballast than the fixed amplitude mechanical vibrator. This is worth exploring in the future in terms of the damage to the ballast, performance of settlement improvement, and post-tamping settlement rate.

The rate of lowering the tamping tines into ballast is also thought to affect the ballast breakage. If the tines plunge more slowly into the ballast, the breakage should reduce. However, this still needs to be studied in more detail.

Lim (2004) found that the breakage from his box tests correlates well with the Los Angeles Abrasion (LAA) and Micro-Deval Attrition (MDA). Similarly, an attempt was made to correlate the Los Angeles Abrasion (LAA) and Micro-Deval Attrition (MDA) to percentage passing 14 mm and 1.18 mm from the tests as shown in Figure 4.33.

From Figure 4.33, it can be seen that only good correlation can be obtained from T1 ((e) and (f)). The correlation from percentage passing 1.18 mm of T2 ((g) and (h)) is not as good but, similar to T1 correlation, it shows that breakage increases with increasing LAA and MDA values. It also can be seen that the percentage passing 14 mm of test 5 does not follow the trend ((g) and (h)) and is suspected to be an anomaly. This is probably because the tamping tines did not plunge evenly into the ballast. The correlation from Traffic and Squeezed are not as good as T1 and they show an opposite trend. This might be because traffic loading and squeeze action produce minimal amount of damage. As a result, the scatter of degradation results can be large and affect the observed trend.

According to Selig and Waters (1994), ballast becomes fully fouled when the percentage passing 14 mm is about 30%. The ballast degradation from the

RTF, Awoleye (1993), and Wright (1983) is not comparable to the fully fouled ballast. One of the reasons might be because the major source of ballast fouling in the UK is from external input such as wagon spillage and air borne dirt (Selig and Waters, 1994). Furthermore, the tests could not simulate the similar level of dynamic force and degree of attrition and were in a controlled environment.

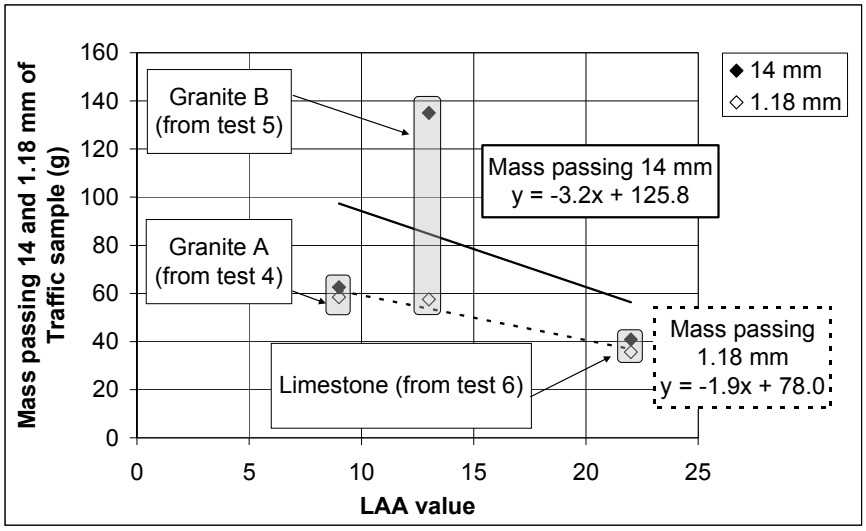

Figure 4.33(a). Correlation between ballast breakage from Traffic sample and LAA value

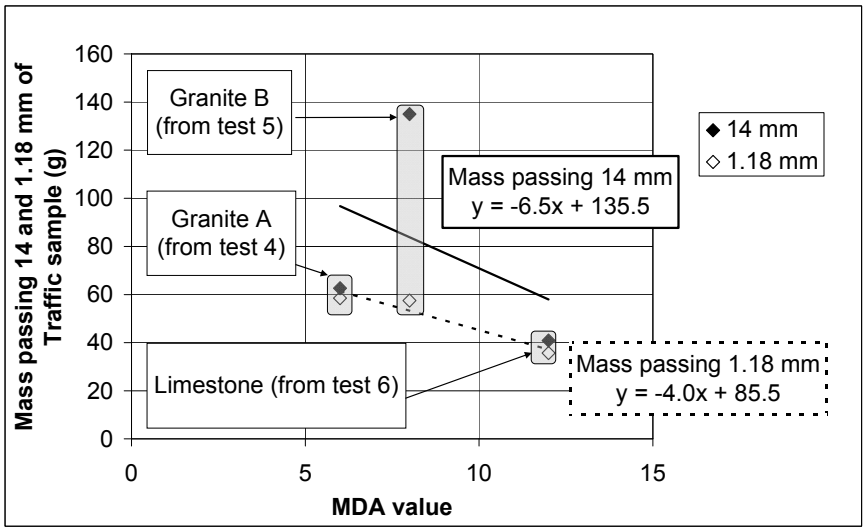

Figure 4.33(b). Correlation between ballast breakage from Traffic sample and MDA value

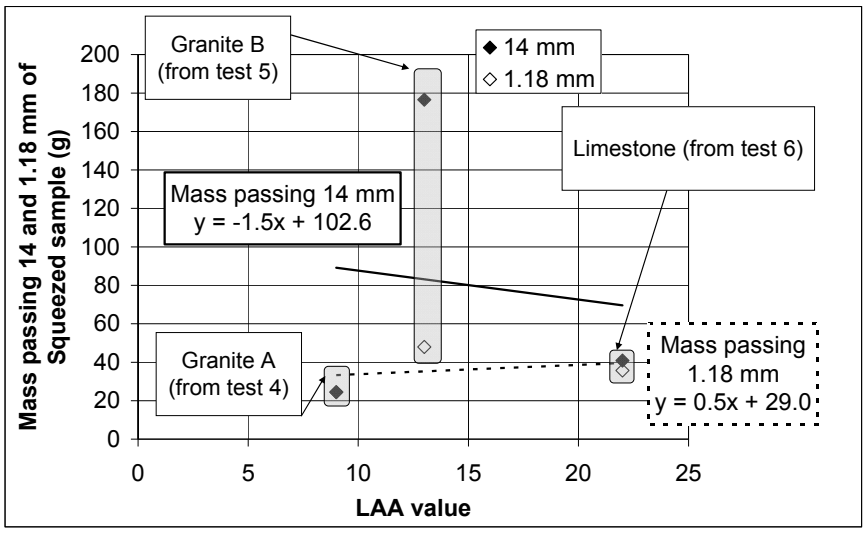

Figure 4.33(c). Correlation between ballast breakage from Squeezed sample and LAA value

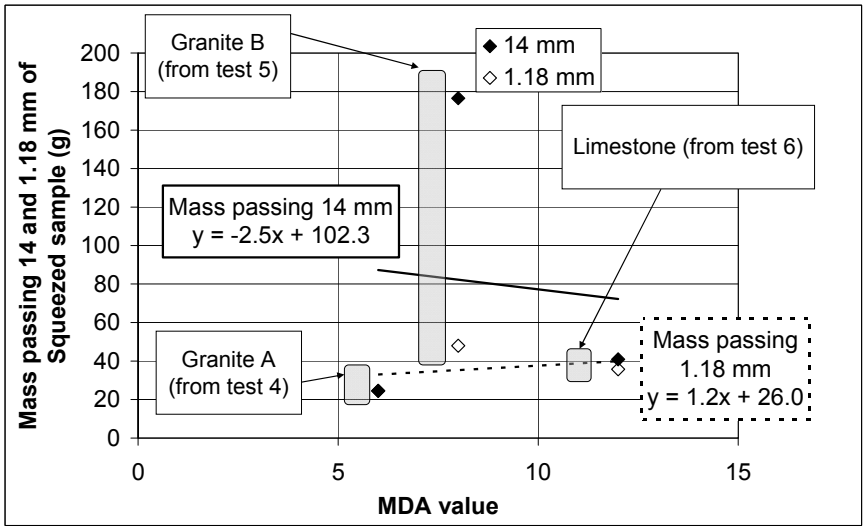

Figure 4.33(d). Correlation between ballast breakage from Squeezed sample and MDA value

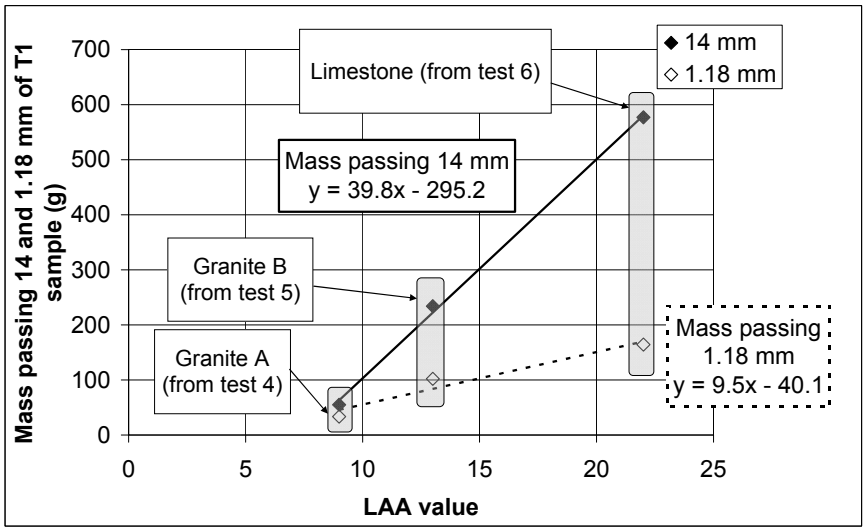

Figure 4.33(e). Correlation between ballast breakage from T1 sample and LAA value

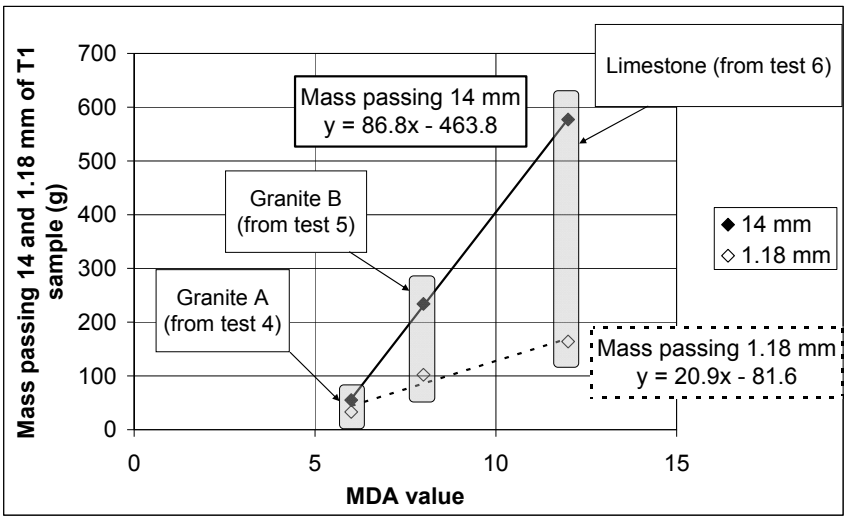

Figure 4.33(f). Correlation between ballast breakage from T1 sample and MDA value

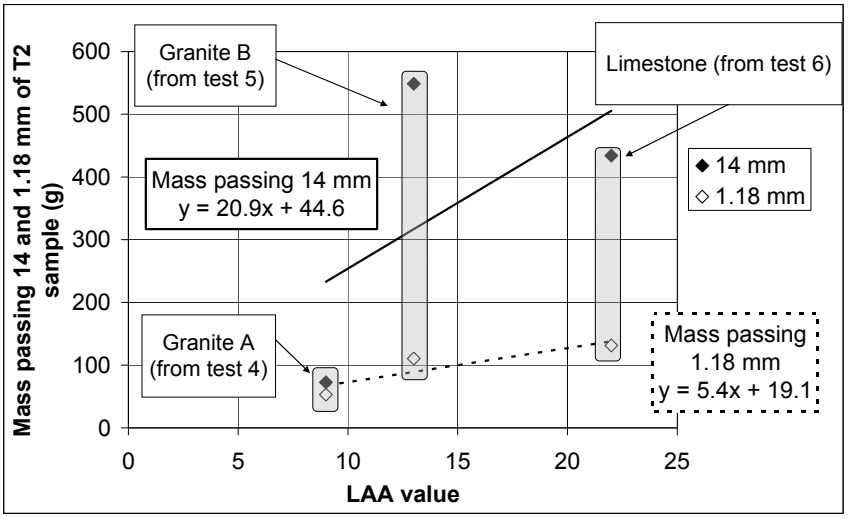

Figure 4.33(g). Correlation between ballast breakage from T2 sample and LAA value

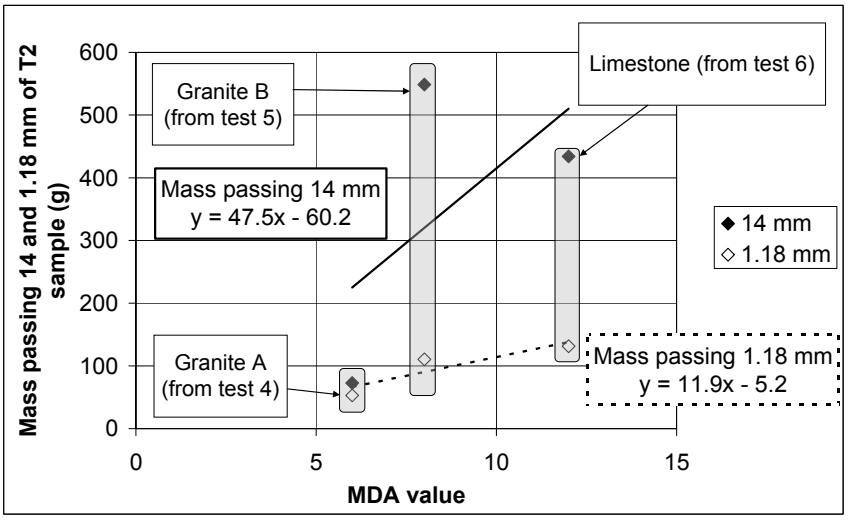

Figure 4.33(g). Correlation between ballast breakage from T2 sample and MDA value

Figure 4.33. Correlation between breakage and LAA/MDA values (a) – (h)

4.9. Conclusions

The Railway Test Facility (RTF) was a newly developed equipment to simulate train traffic loading and tamping maintenance for observing the settlement and ballast breakage. The whole facility was housed in a concrete pit which was filled with silt and ballast as the track bed material. Three concrete sleepers were placed on top of the ballast. Three servo hydraulic actuators, contained in the loading frame, supplied the cyclic loading which was transferred to the rail seats of the three sleepers. Tamping was performed in the RTF by a tamping bank which was modified from a real Plasser tamping machine. The loading frame could be removed for the tamping bank to be positioned for the tamping operation.

It can be concluded from the test results that

- The settlements of the outer sleepers are larger than the middle one probably because of the boundary effect between the pit walls and the ballast. However, the boundary effect should not affect the settlement of the middle sleeper as its location should be adequately far away from the pit walls.
- The settlements from different ballasts are similar to each other but are lower than the settlement in the real track. This is probably due to the large dynamic loading on site.
- With the same amount and magnitude of traffic loading, different ballast types had similar amount of settlement.

- Tamping can improve settlement but cause faster rate of settlement afterwards.
- Tamping tine insertion was the main source of degradation in this project.
- LAA and MDA values can predict the durability of ballast as the breakage from tamping increases with increasing LAA and MDA.

While the degradation from the traffic loading matches previous researches, the degradation from the tamping in the RTF does not. This is probably due to the restraint on the tamped sleeper and the means of vibration. The sleeper restraint in the RTF was small compared to Wright (1983) and the real tamping in which a tamping wagon is used. Also, the amplitude of vibration of the tamping tines in the RTF may decrease during the tamping operation due to the use of the hydraulic system rather than a mechanical system. Therefore, the hydraulic vibrating system may be more preferable than the mechanical vibrating system as it is less likely to damage the ballast. However, the reduced amplitude tamping needs to be further studied to ensure that similar performance can be achieved. Furthermore, the overall degradation from the test in the RTF is not comparable to the actual degree of fouling in the track. This is because the major source of fouling in the track was not included in the tests.

5. Triaxial Test

5.1. Introduction

A good understanding of ballast behaviour and the geotechnical parameters that control its performance will help in reducing ballast maintenance cost. Since ballast cannot easily be taken from the track in its in-situ condition and since controlled tests are difficult in the field, laboratory ballast testing that can simulate loading conditions in a railway is desirable. Cyclic triaxial testing is the most suitable test for this job as it is used extensively for testing geotechnical materials. However, triaxial tests on ballast have to be performed on large samples so that the aggregate sizes for the specified grading can be used. Triaxial tests using servo hydraulics can apply cyclic axial stresses to ballast to simulate the stresses due to traffic. Also, lateral stress on the ballast can be applied as a cell confining stress via pressurised air and water to simulate the effect of the surrounding ballast.

5.2. Triaxial test apparatus

The triaxial apparatus in this project, shown in Figure 5.1, was used to investigate the behaviour of ballast under static loading and repeated loading under different stress conditions. It was designed for a sample of 300-mm diameter and 450-mm height. It was manufactured by GDS Instrument Ltd. Figure 5.2 shows the schematic diagram of the apparatus. It utilises the triaxial apparatus system presented in Ng et al. (2002) based on a differential pressure measurement for volume change instead of on sample axial and radial displacement measurements. This method was preferred due to the irregular

outer surface profile of the sample caused by the large size and angular shape of the ballast.

The principle of this system is to use water in an inner cell which is in direct contact with the sample (Figure 5.2). Air at a specified pressure is directed to an outer cell so that the water in the neck is pressurised and consequently a confining pressure is applied to the sample. As the pressures in the inner and outer cells are equal, the inner cell volume remains constant so any change in the volume of the sample will displace an equivalent volume of water in the inner cell.

The volume change is measured by recording the differential pressure between the water in the neck of the inner cell and the water inside a reference tube using a differential pressure transducer. At the beginning of each test, the water levels in both the inner cell and the reference tube are equal. If the sample in the inner cell expands, the water level in the inner cell rises while the water level in the reference tube stays the same. The differential pressure transducer reading is converted to a volume change based on the known cross-sectional areas of the inner cell neck and the reference tube. Average radial strain can be calculated from the axial and volumetric strains. Furthermore, a scale was attached to the neck of the inner cell to double check the accuracy of the volume change measurement. The differential pressure transducer cannot register the differential pressure instantaneously. It was found that it was able to accurately read the volume change at the frequency of 0.2 Hz. As previously mentioned, a conventional on-sample measuring system such as strain collars

would measure the localised grain movement rather than the overall change in diameter of the sample and would be difficult to attach to the irregular surface of the sample. It should also be noted that this method was originally developed for a smaller and more uniform sample and would probably measure dynamic volume change at higher frequency.

Figure 5.1. The triaxial apparatus

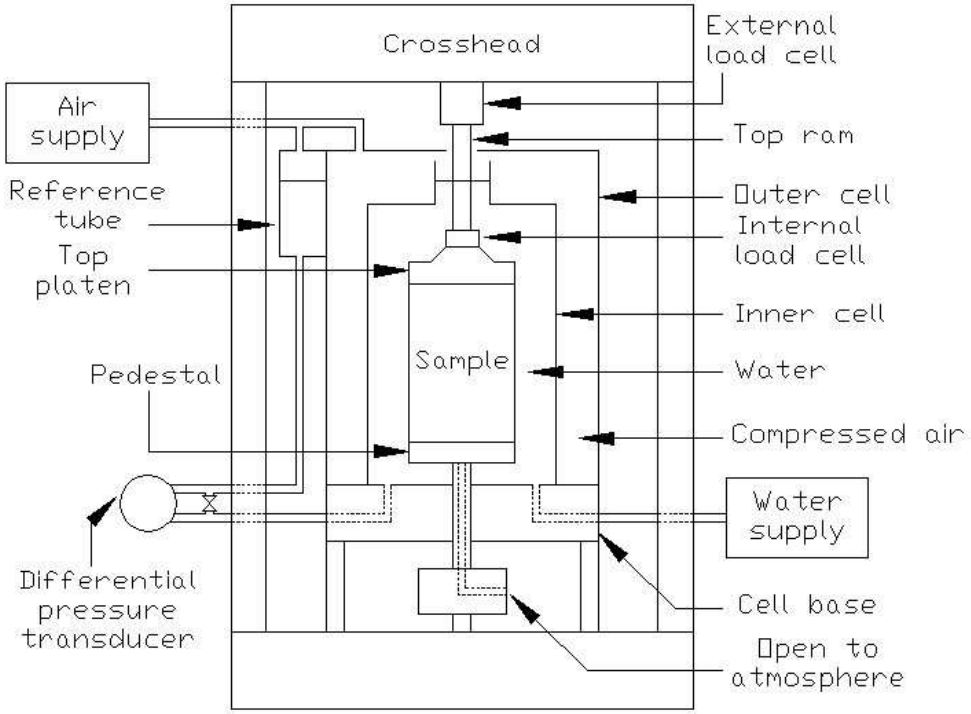

Figure 5.2. Schematic diagram of the triaxial apparatus

Axial load is applied to the sample by an actuator fitted to the base of the machine. The shaft of the actuator passes through a seal in the bottom of the cell and is connected to a pedestal supporting the sample. The load was monitored by a 100 kN external load cell and a 64 kN internal load cell. The internal load cell was optional but is independent of the friction of the shaft passing through the cell top. A comparison of the reading between the two cells showed that the frictional effect was negligible. The load on the sample was controlled by the feedback from the external load cell. It was later found that the thread that screwed the internal load cell to the top ram was damaged and it had to be removed. As the readings from both load cells had been found to be equal, only the external load cell was used afterwards.

Axial deformation was measured by an LVDT (Linear Variable Differential Transformer) displacement transducer connected to the loading actuator. This applied upward load thereby lifting the sample against the upper fixed crosshead so the LVDT was in direct contact with the sample. The displacement range of the system was 100 mm. This upward movement in the inner cell means that the actuator shaft displaces the water in the inner cell and this was subtracted from the total volume change to obtain the sample volume change.

5.3. Test sample

5.3.1. Materials and Grading

The same granite A and limestone were used in the triaxial tests. Different sample gradings were used with the different ballasts. This depended on the grading of each ballast when it was delivered to the laboratory. The sample gradings are shown in Figure 5.3.

5.3.2. Dimensions

The sample had a diameter and height of 300 mm and 450 mm. As the maximum grain size of a sample was 50 mm, the ratio of the sample diameter to maximum particle size (D/d_{max}) is six which is within the typical range of five and seven according to Skoglund (2002).

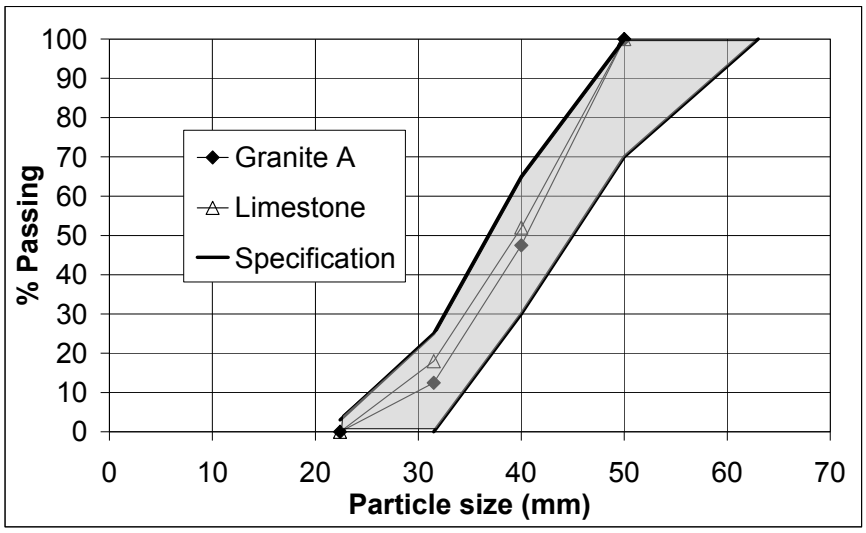

Figure 5.3. Grading of triaxial samples and ballast specification

The ratio of the height to diameter of the sample (*H*/*D*) was 1.5. However, Bishop and Green (1965) suggested the *H*/*D* ratio of two to eliminate the effect of friction at both ends of the sample. Nevertheless, the ratio of 1.5 enabled easier and more economical design of the cells in this project. Duncan and Dunlop (1968) concluded that end friction caused an insignificant increase in the angle of shearing resistance in their drained triaxial tests on sand. Furthermore, they added that lubrication at both ends was necessary when volumetric strain needed to be calculated. This was because end friction usually caused the triaxial sample to bulge into a barrel shape. This meant the diameter of the sample was not uniform through the whole height of the sample and therefore affected the calculation of volumetric strain. However, this was not a problem in this project since the volumetric strain could be measured directly. However, an effort was made to lubricate the ends of samples in this project. This will be explained in the later section.

5.3.3. Top platen, pedestal and sample discs

Stainless steel top platen, pedestal and sample discs were used in the sample preparation which is discussed in the next section. The top platen and pedestal each had a groove around their edges for sealing membranes around the sample by O-rings. The pedestal was screwed onto the lower ram with a vacuum line routed through the lower ram and the pedestal into the sample. The top platen made direct contact with the top ram when the sample was raised.

The top and bottom sample discs were in direct contact with the sample to protect the top platen and pedestal from damage by the sharp ballast particles. The discs were 310 mm in diameter, 8-mm thick, and had twenty 1.5-mm-diameter holes in the middle for drainage purpose.

5.3.4. Preparation

The sample preparation method in this project was changed several times to obtain an air/water-tight seal on the sample and optimum sample density. The method below is the final one that was found to work well.

Fifty five kilograms of ballast with the required grading was mixed on the floor by a shovel. Care was taken not to break the ballast. It was necessary to make the sample on the cell base which was bolted onto a vibrating table.

A 2-mm latex membrane was put inside and folded over the top and bottom of a split aluminium mould which has an internal diameter of 304 mm. The mould was made of two halves, joined with six bolts.

Next, a circular sheet of filter paper was placed on top of the pedestal to prevent fines from blocking and entering the drainage hole. The bottom sample disc was then placed on the filter paper and the mould plus the membrane was placed on the pedestal and the disc. Then, two circular latex sheets sandwiching silicon grease were put on the disc. They were used at both sample ends to reduce the friction. The bottom latex sheets had a 50-mm-diameter hole at the centre for drainage purpose while the top ones had no holes for drainage as there was no drainage path through the top platen.

The mould was then filled with the ballast in three layers. Each layer was vibrated for 30 seconds with a surcharge of 20 kg on top of the layer. While the mould was being filled, some small and flat particles were kept for levelling the final surface. On the top layer, the top cap was used instead of the 20 kg weight. The top of the sample was levelled by hand with the small and flat particles followed by another vibration with the top platen on top. This was repeated until the top of the sample was level.

After it was levelled, the top platen was removed and the remaining test material was weighed so that the mass of the sample could be found. The quantity and size of the surplus material varied with different samples so the grading of different samples could vary. Then, the lubricated latex sheets were placed on the top of the sample followed by the top sample discs and the top platen. With this method of sample preparation, the usual sample mass ranges between 48 and 52 kg. This is associated with bulk density of 1,500 – 1,630

kg/m^3 and void ratio of 0.6 – 0.7. This density is slightly lower than the approximated ballast density in the RTF.

Silicone grease was then applied in both the top and bottom grooves of the sample. The folded membrane ends were pulled over the grooves and two o-rings were used to seal the membrane into the grooves. Next, a vacuum pump was used to apply a partial vacuum of approximately 20 – 30 kPa vacuum to the sample via the hole at the bottom of the cell base. Full vacuum had been used but this would cause puncture of the membrane particularly with the limestone. There was a detachable tap connection between the vacuum pump and the drainage hole and this was used during transportation of the sample to the testing frame. The mould was then removed and the sample was covered by another membrane. This membrane had a thickness of 1 mm. It should be noted that even if there are holes in the inner membrane but none on the outer one, the seal can be maintained. Furthermore, due to frequent membrane puncturing, it was found that a bicycle puncture repair kit could be used to fix the holes in membranes. Both o-rings were removed from both grooves and immediately placed again in the grooves over the two layers of membrane. Insulating tape was put around both o-rings and two jubilee clips were used to cover the o-rings. The jubilee clips held the position of the o-rings during a test while the tape helped to maintain an even pressure on the o-rings.

To check if there was a leak in the sample, the inner cell was bolted onto the cell base and filled with water to the neck so that the sample would be surrounded by the water. The water level on the neck can be observed by

reading the scale on the neck. If the water level did not drop for approximately five minutes, it could be assumed that there was no leak on the sample. If there was a leak, the membrane and the seals at the sample ends should be checked and care taken to ensure that water did not enter the vacuum pump via the connecting pipe otherwise the vacuum pump could be damaged.

The outer cell was then bolted onto the cell base. The cell base was then positioned and bolted onto the testing frame. The air and water pipelines were connected to the cell base and the top of the outer cell. The air supply was then switched on and the required air pressure was supplied to the system. The vacuum was removed when the air pressure reached 30 kPa. The pressure was then adjusted to the required level of the test. After the required air pressure was reached, a seating load of 1 kN was put on the sample. More water was added into the inner cell as the water in the inner cell would go into the reference tube via the cross-drained valve which must be open at this stage. During this process, all pipelines should be free of air bubbles. If there were any, they should be released immediately. At the end of this process, the air pressure should be checked and the water level in the neck should be the same as the reference tube. The cross-drained valve was then closed. The sample was now ready for testing.

5.4. Test development

This type of large triaxial testing equipment is more difficult to use than a standard triaxial test as mechanical aids to manual handling are necessary. The sample is heavy and irregular in shape requiring non-standard membranes for

sealing. Consequently, certain difficulties were encountered when implementing the test programme.

5.4.1. Initial problems

At the start of the triaxial testing programme, the membrane was punctured every time the sample was pressurised. As a result, water entered the sample. To overcome this problem different membrane thicknesses and a doubling of the number of membranes were tried on granite A samples but the membrane was still punctured. It was found that the control system reading for the cell pressure was significantly under-registering which would contribute to the puncturing of the membrane as the real cell pressure would be too high. However, after the cell pressure set up was corrected, the water still entered the sample. The problem was traced to the seals at both ends of the sample letting in water. Different sealing methods were tried until good seals at both sample ends were obtained. The final sealing method was previously described in Section 5.3.4.

During the early stage of the test programme, it was found that the differential pressure transducer output, which was converted to sample volume change, sometimes did not follow the expected sinusoidal response as shown in Figure 5.4. The device is extremely sensitive and measures, in terms of pressure, the difference in a head of water which is changing by less than a millimetre per cycle up to long term changes of about 40 mm. It is possible that the electrical drift of the transducer output may have distorted the volumetric strain results. Sometimes, the electrical drift does not distort the waveform but causes an

error in resilient volume change. This then results in sudden significant increase or decrease in resilient volumetric strain and affects the calculated Poisson's ratio. This will be shown later. Also, the water level has to be totally stable and any disturbance of the water in the inner cell would influence the reading. Before this could be resolved, the differential pressure transducer stopped registering volume change and subsequently after it had been returned to the manufacturer, it was found that it had been over-ranged. Some tests were performed while the differential transducer was not available for approximately three and a half months and measurement of volume change in those tests was obtained by reading the water level on the scale of the inner cell neck. The scale was originally for double checking the accuracy of the volume change measurement. It should also be noted that the resilient volume change cannot be accurately obtained from reading the scale due to a very small change of water level in a cycle.

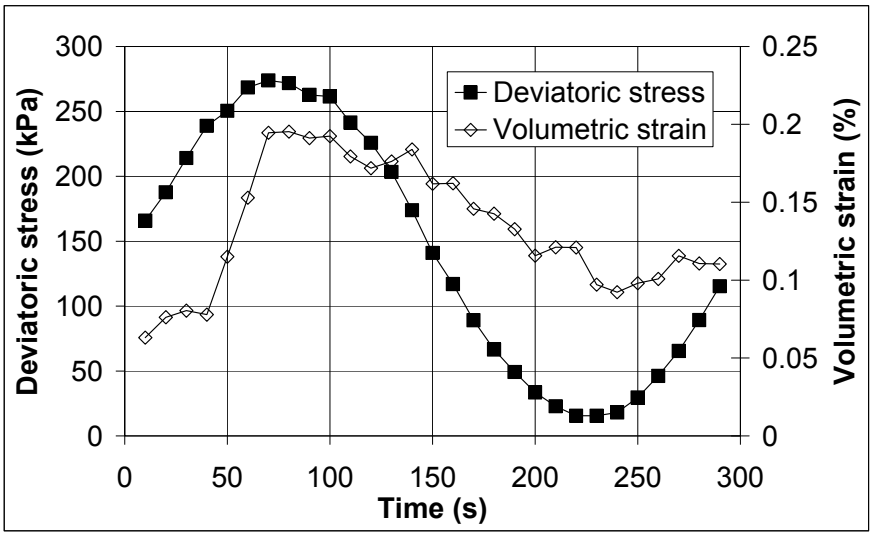

Figure 5.4. Deviatoric stress and random pattern of volumetric strain in a cycle

After the differential pressure transducer was repaired, it was calibrated and found to be usable again. Up to this point tests had been carried out on granite A without further membrane failures. Tests were then started using limestone ballast. However, the differential pressure transducer did not register the change in volume again. Therefore, another calibration was then performed and it was found that it registered the volume change but its sensitivity had to be doubled from the previous value to give the correct volume change reading. It was then found that the new sensitivity did not stay constant so it was sent back to the manufacturer for the second time. While it was away for repair for approximately two months, two alternative methods of volume change measurement were tried. These are an image analysis and ultrasonic level measurement.

5.4.2. Image analysis

A test was performed without both the inner and outer cells and was held by a partial vacuum instead of the cell pressure. A digital camera with image resolution of 7.1 megapixels was used to remotely take pictures of the sample during a test. However, White et al. (2003) reported that image resolution of 2 megapixels was adequate for this type of analysis. The camera was connected to a power supply as the test would last for approximately ten hours and the camera battery has insufficient power for this purpose. The picture of the sample is shown in Figure 5.5.

Figure 5.5. Test sample for the test with image analysis

The pictures were taken at the beginning of the test and at maximum and minimum load of cycles 1 – 25, 100, 200, 500, 1000, 2000, 5000, 10000, 20000, 50000, and 100000. They were then analysed by a program called "GeoPIV" run under MATLAB to obtain the sample movement from the test (White and Take, 2002 and White et al., 2003). This program is usually used in geotechnical experiments to track the movement of a fine grain soil over a series of images. The membrane must be spray-painted so that it has a suitable texture for the program to track the movement. Three columns of square meshes were placed on the vertical edges of the sample shown in Figure 5.6. The program searches around each mesh to detect the movement and, hence, obtain the displacement. The search area around each mesh is called a search zone. The sizes of a mesh and search zone are measured in pixels. As an example, the sizes of mesh and search zone used in the first test (25 and 50 pixels) are shown in Figure 5.7. The movement of the meshes was detected from each picture and then converted to axial and radial strains. The vertical

displacement of the sample was obtained by detecting the vertical movement of the bottom meshes i.e., the meshes in the bottom row shown in Figure 5.6 relative to the top meshes which were placed near the stationary top platen. The horizontal displacement was obtained by comparing the average horizontal distance between the left and right meshes to the original distance. The pictures of the meshes on the sample at the end of the test are shown in Figure 5.8.

Figure 5.6. Meshes on the sample at the beginning of the test

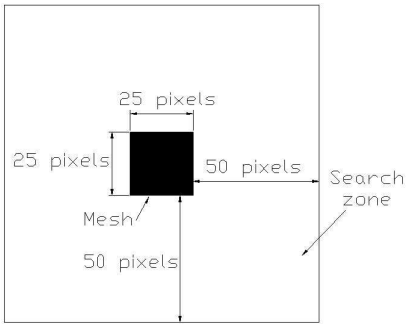

Figure 5.7. 25-pixel mesh with search zone of 50 pixels

Figure 5.8. Meshes on the sample at the end of the test

It can be seen from the figure that the meshes are scattered at the end of the test. A few of them are even outside the sample. That was probably because the load was increased from the seating load (1 kN) to the mean load (4.25 kN) in one minute. During this short period, not enough number of images was taken for the program to correctly detect the sample movement. Also, this loading rate was probably too quick for the strength of the sample. As a result, the sample was overly compressed i.e., axial strain increased to 12 % in one minute during this stage.

The plot of axial and radial strains against number of cycles from the test is shown in Figure 5.9. There was no physical measurement of the radial strain on the test. It can be seen from the figure that the axial strain from the image analysis was significantly different to the strain from the physical measurement. However, the slopes of both lines are the same. Therefore, the difference may be from the fast load build up at the start of the test again.

Furthermore, the permanent radial strain was expected to be negative rather than positive because the sample bulged.

For the second test, radial measurement using two LVDTs was tried by attaching them to rigid rods screwed into the base. Discs were fitted to the end of the spring loaded LVDT shafts so that they would rest against the membrane covered ballast at mid height of the specimen. However, this system of measurement could not accommodate the vertical movement of the sample during loading and the discs tilted and even became detached. Consequently, it was very difficult to obtain a direct measurement of the radial strain so the validation of the image analysis was limited to axial strain measurement from the actuator LVDT. Figure 5.10 shows the axial strain results from this test. As the load was built up too quickly in the previous test, this time it was built up from the seating load (1 kN) to the mean load (6.88 kN) at approximately 0.5 kN per minute. According to the figure, the discrepancy between the permanent axial strain from the image analysis and physical measurement was smaller than the previous test. Therefore, the reduction in loading rate improved the performance of the measurement technique. Furthermore, this loading rate prevented the sample from being overly compressed.

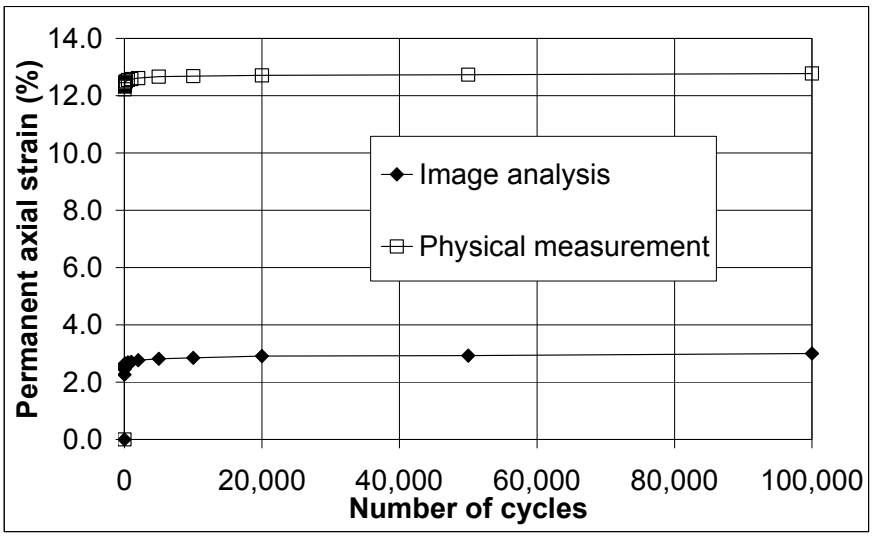

Figure 5.9(a). Permanent axial strain from the first test with image analysis

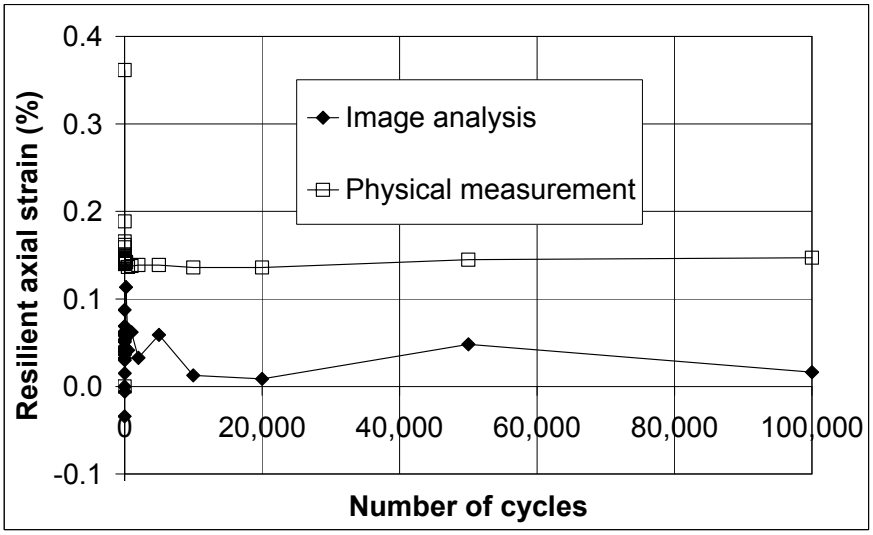

Figure 5.9(b). Resilient axial strain from the first test with image analysis

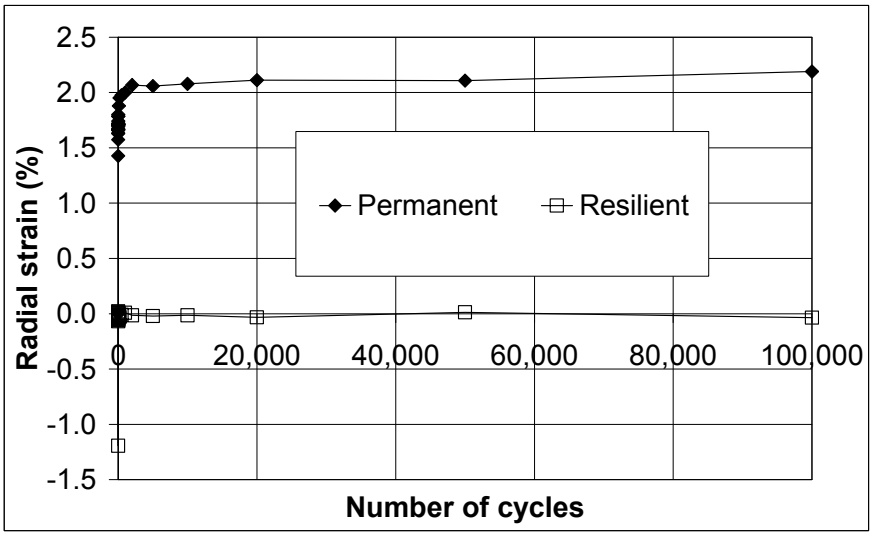

Figure 5.9(c). Permanent and resilient radial strains from the first test with image analysis

Figure 5.9. Strain results from the first triaxial test with image analysis (a) – (c)

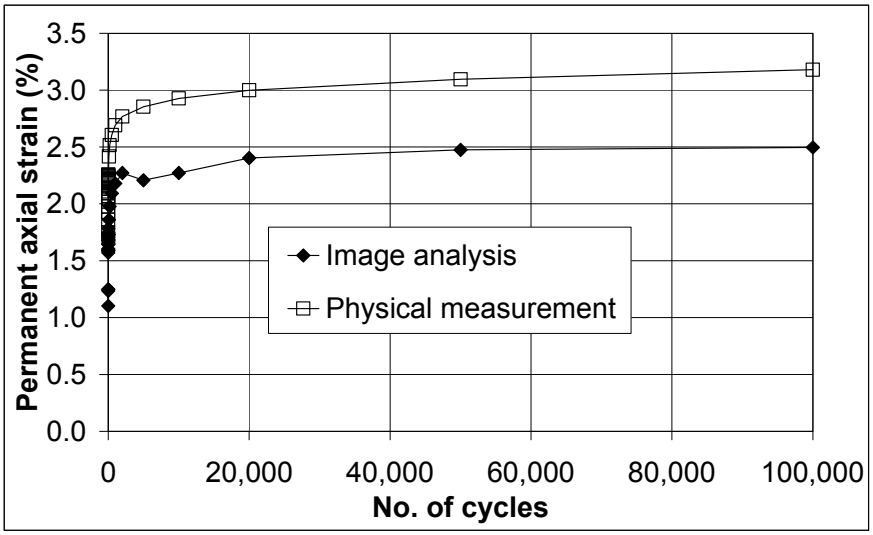

Figure 5.10(a). Permanent axial strain from the second test with image analysis

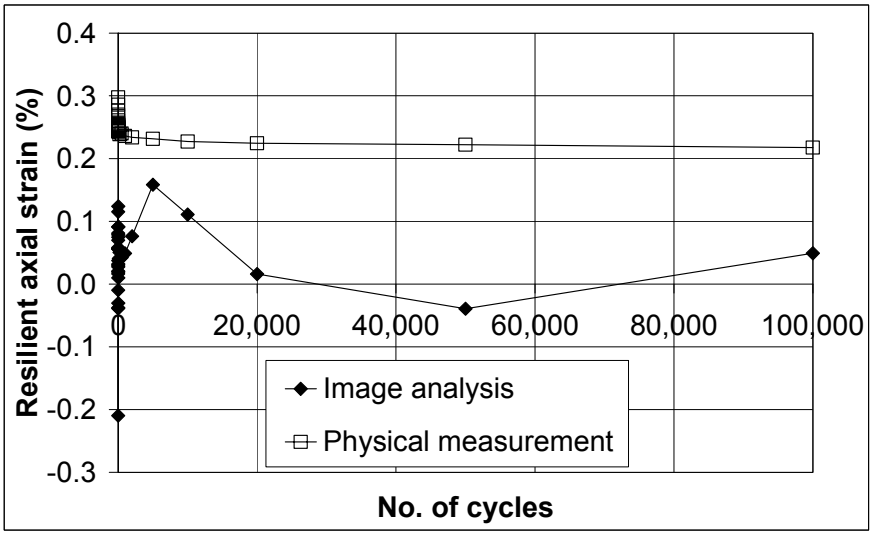

Figure 5.10(b). Resilient axial strain from the second test with image analysis

Figure 5.10. Axial strain results from the second triaxial test with image analysis

The pictures from this test were re-analysed with five different sizes of meshes and search zones. Both of them are measured in pixels. It was found that both of them affected the test results as shown in Figure 5.11. It can be concluded that the optimum sizes of the mesh and search zone are 25 and 50 pixels.

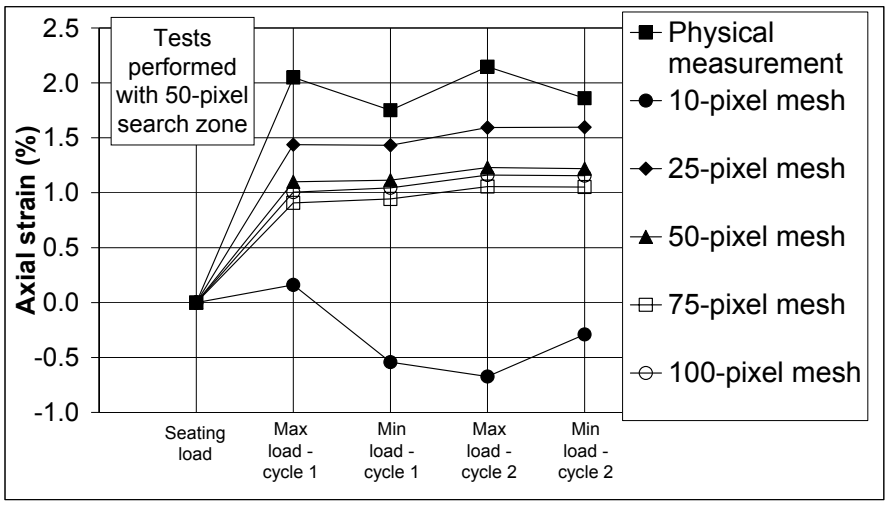

Figure 5.11(a). Effect of mesh size on axial strain

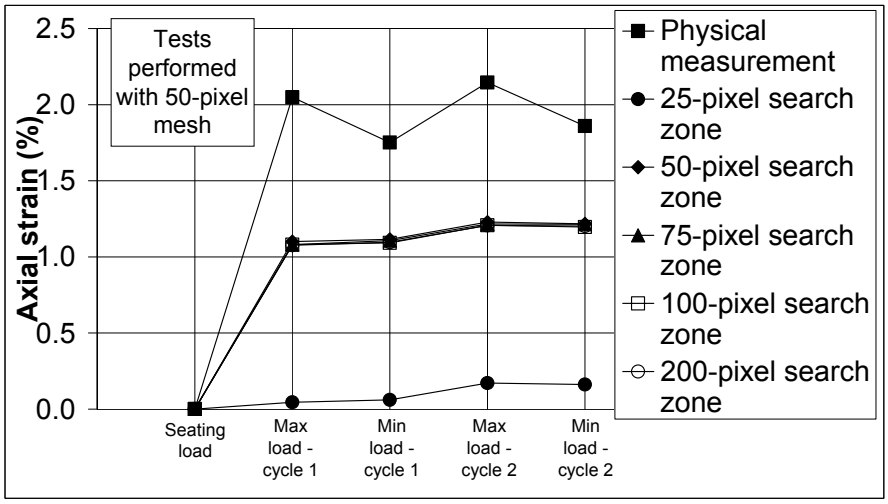

Figure 5.11(b). Effect of search zone on axial strain

Figure 5.11. Effect of mesh size and search zone on axial strain from image analysis

The third test with the image analysis was performed with two cameras and three LVDTs around the sample as shown in Figure 5.12. While the load was built up from the seating load (1 kN) to the mean load (6.88 kN), pictures of the sample were taken as many times as possible. These pictures would then be included in the analysis to help the program to cope with the large movement of meshes. Even though the discs were fixed to the LVDT shafts in this test to prevent tilting and detachment of the discs, it was still difficult to obtain the

measurement from the LVDTs and the LVDT setup did not stay rigid enough to accommodate the sample movement. Furthermore, it was found later that the sample rotated during the test. The rotation of the sample will have an adverse effect on the calculation of radial strain on the image analysis as the meshes will move horizontally by rotation instead of expansion and some meshes might move outside the sample. This might be due to the rotation of the bottom loading ram or because the screw between the ram and platen became loose or because of a combination of both. As a result, the radial strain measurements from both the cameras and the LVDTs were invalid. The axial strain results from this test are shown in Figure 5.13. It can be seen that permanent axial strain from the image analysis is very similar to the physical measurement while the same level of discrepancy of the resilient axial strain can still be seen.

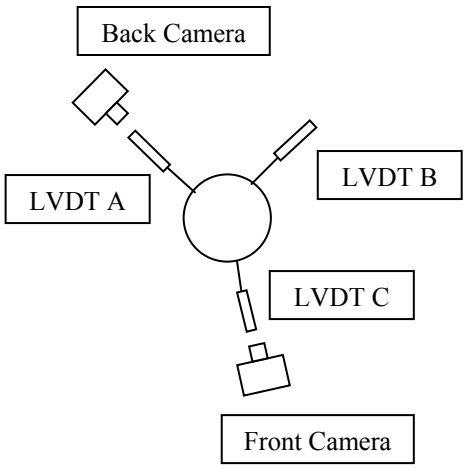

Figure 5.12. Arrangement of the cameras and LVDTs in the third test with image analysis

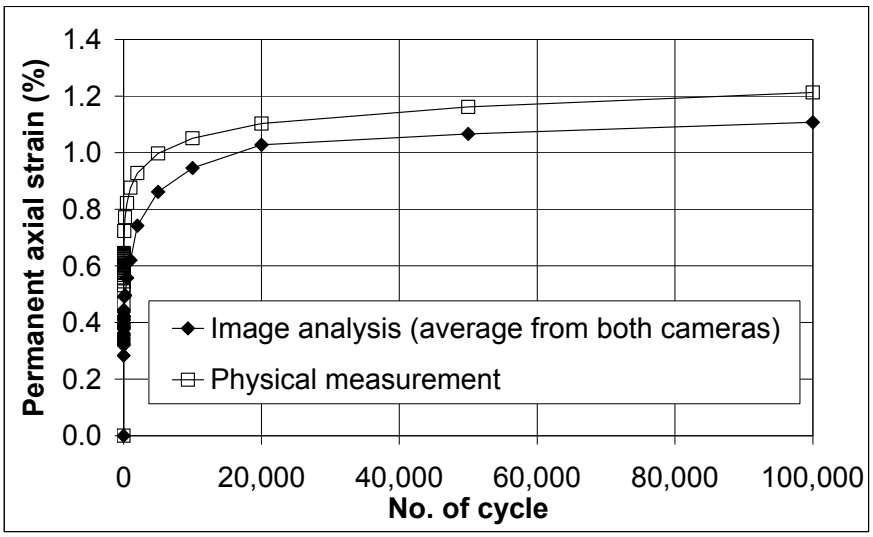

Figure 5.13(a). Permanent axial strain from the third test with image analysis

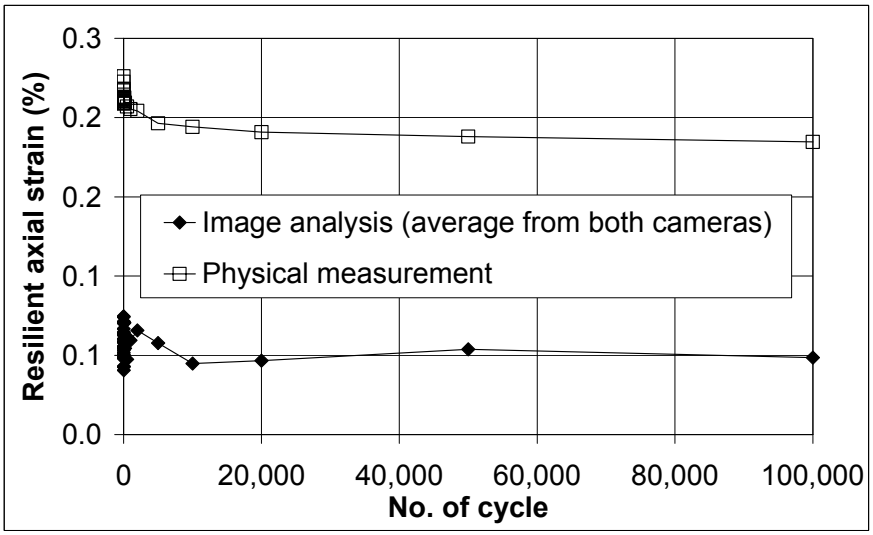

Figure 5.13(b). Resilient axial strain from the third test with image analysis

Figure 5.13. Axial strain results from the third triaxial test with image analysis

Later, it was realised that the calculation of the radial strain from the image analysis was not correct as the horizontal movement of the meshes in the pictures is not exactly equal to the movement along the diameter of the sample as shown in Figure 5.14. A new idea of measuring radial strain was initiated. Different points on a sample can be marked by stickers. The horizontal movement of each point from a camera can then be detected. However, if a

point moves toward the camera, the component of horizontal movement directly towards the camera cannot be detected. This can be solved by placing another camera at a different angle. Therefore, at least two cameras are needed in the test to ensure that all directional components of the horizontal movement of each point are obtained. However, the radial strains obtained from this method are from discrete points and the rotation of the sample is still a problem with this approach. Before the alternative method for measuring radial strain with the image analysis was tried, another test method was explored and found to be more promising and to have a simpler principle than the image analysis. Therefore, the test method was changed.

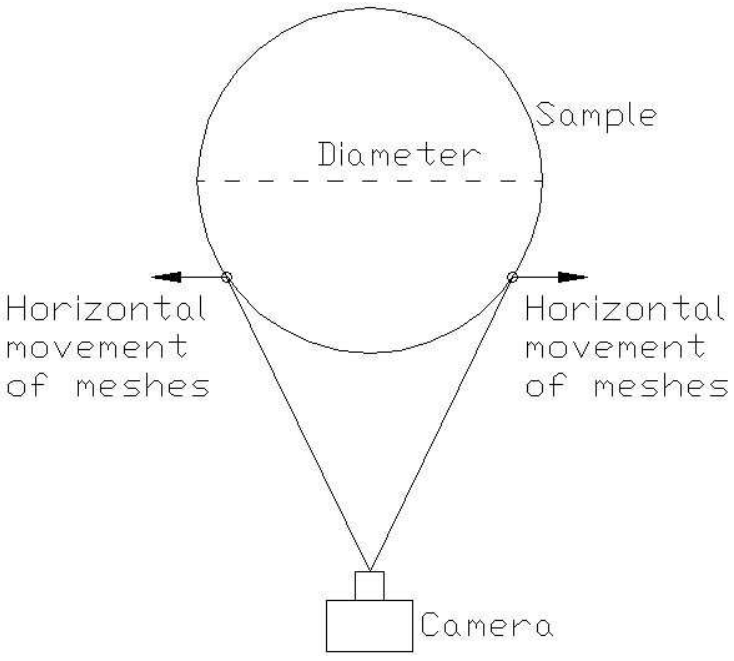

Figure 5.14. Horizontal movement of the meshes in the image analysis

5.4.3. Ultrasonic level measurement

The second method used an ultrasonic proximity transducer (UPT) shown in Figure 5.15. This type of transducer uses ultrasonics, i.e. sound wave above the

audible limit, to measure the distance from a transmitter to a surface. It measures the time lag between the transmitted sound waves and the return sound waves and converts this to voltage. It is ideally suited to provide a non contact switching device or an analogue device to measure fluid level. The model used had a range of 30 to 250 mm and was calibrated by positioning it over a beaker of water and raising the beaker in increments which was measured by a dial gauge. The output was found to be linear with a sensitivity of 0.045 V/mm and a resolution of 0.5 mm.

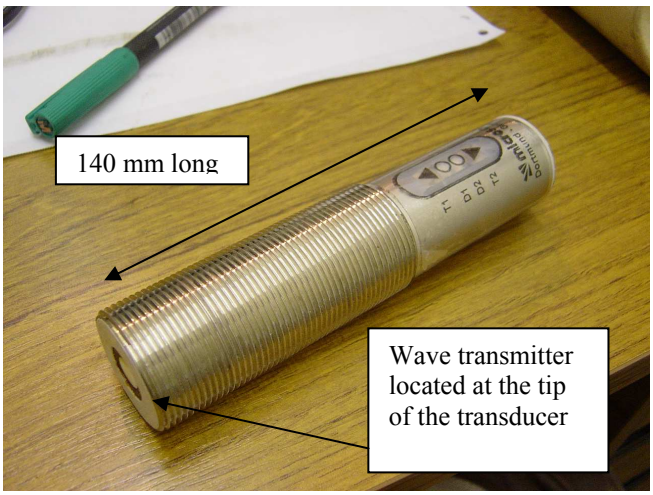

Figure 5.15. Ultrasonic proximity transducer (UPT)

Initially, the UPT was fitted to the top of the water level in the reference tube. Normally, this cylinder is locked off with a valve so that the differential pressure transducer can measure the change in head of the water in the neck of the inner cell relative to the fixed head in the reference tube. However, without using the differential pressure transducer it was possible to keep the valve open so that the water level in the reference tube would follow the water level in the inner cell. The volume change measurement accuracy of the UPT was done

with the triaxial cell assembled without a sample in place. The inner cell was filled with water and the connection made to the reference tube to equalise its water level with the inner cell. The actuator was raised to a fixed amount and this displaced a known volume of water in the inner cell. Confirmation of this volume change was checked with a scale attached to the neck of the inner cell. It was found that the UPT measured this volume change accurately but there was a time delay before the water level in the reference tube equalised with the level in the neck of the inner cell. This lag would be a problem for dynamic volume change measurement and it was clear that a direct measurement of the change in water level in the neck was necessary.

The only way of fitting the UPT above the neck of the inner cell without a significant modification to the cell top was to carry out a test with the cell top (outer cell) removed. It was clamped to a shaft supporting the load cell so that it could look directly down to the water in the inner cell. This was done initially without a sample and the UPT worked satisfactorily when calibrated by raising the actuator to simulate a known volume change.

A test was then carried out with a sample under vacuum in the inner cell as the external pressure could not be applied with the outer cell removed. This system appeared to be working well for the low frequency up to 1 cycle per minute. However, at 4 Hz the upper shaft supporting the load cell could be seen to be moving laterally, because the top platen was tilted due to uneven settlement of the ballast. This would not happen when the cell top is in place as it acts as a support for the upper shaft and keeps the top platen level. The test was stopped

at this stage and only limited results from the UPT were obtained. However, the differential pressure transducer had now been returned from the manufacturer and was used in the remaining part of this test and the later tests.

After that, the differential pressure transducer was used in the later tests. However, its sensitivity did not stay constant again even though the manufacturer said that it was working fine. As testing needed to continue, it was calibrated before and after every test by pushing the bottom ram upwards to displace a known volume to the water in the inner cell. The volume change reading from the differential pressure transducer was then plotted against the known volume change to obtain the conversion factor. The average conversion factor for the calibrations before and after each test was used to convert the reading to the real volume change. It was found that the factor varies between different tests but the factors obtained before and after each test were equal.

The use of the image analysis technique and the UPT to measure volume change were not readily adaptable because the triaxial cell arrangement had been designed to work with the differential pressure transducer as described in section 5.2. It was essential that testing should continue preferably with the outer cell fitted as maintaining a vacuum on a sample continually puts an unacceptable demand on a vacuum pump if a robust vacuum system is not available.

5.5. Test Procedures

Both monotonic and cyclic triaxial tests were performed in the project. After both types of tests, the sample was sieved to obtain the particle size distribution. For the monotonic tests, the sample was put under a seating load of 1 kN at the beginning. The sample was then loaded at 1 mm/min until the axial strain reached approximately 12 %. This was to prevent the sample from touching the inner cell according to an observation in the first monotonic test.

Cyclic tests on granite A and limestone were performed by slightly different methods. For cyclic tests on granite A, the sample was put under a seating load of 1 kN. The load was brought to the mean load and cyclic loading was started with the frequency of 0.2 Hz for the first 99 cycles. The rest of the test would be loaded with a frequency of 4 Hz until cycle 100,000. However, cycles 100, 200, 500, 1000, 2000, 5000, 10000, 20000, 50000, and 100000 were loaded with a duration of 5 minutes per cycle. This was to obtain the resilient sample volume change in the test. It should be noted that before and after these slow cycles, the test was paused for 10 minutes to wait for the water level in the inner cell to stabilise as unstable water in the inner cell would cause errors in the volume change reading. During the pauses, the load was dropped to the seating load of 1 kN.

For cyclic tests on limestone, the sample was also put under the seating load of 1 kN. However, the load was slowly built to the mean load with the rate of approximately 0.5 kN per minute to avoid the sample being overly compressed. Furthermore, cycles 1 to 5 and 6 to 30 were loaded with a duration of 5

minutes per cycle and 1 minute per cycle, respectively. After that, most parts of the test were performed with the frequency of 4 Hz until cycle 100,000. However, cycles 31-100, 181-200, 481-500, 981-1000, 1981-2000, 4981-5000, 9984-10000, 19981-20000, 49981-50000, and 99981-100000 were loaded at 0.2 Hz to obtain the resilient sample volume change.

The speed (or frequency) of the slow cycles for obtaining the sample volume change was changed from 5 minutes/cycle to 0.2 Hz because the electrical drift of the differential pressure transducer may distort the sample volume change over an individual cycle in some cyclic tests on granite A as shown in Section 5.4.1. Therefore, having a group of slow cycles is more accurate than having an individual cycle as the volume change measurement response can stabilise.

5.6. Test Programme

The triaxial tests in this project were divided into three test series and are summarised in Table 5.1 and the *q-p'* stress paths of cyclic tests are shown in Figure 5.16. As a sample is loaded until axial strain reaches approximately 12 % in monotonic test (Series 2), the maximum deviatoric stress is unknown before the test. Hence, the *q-p'* stress path from this series cannot be plotted. It should be noted that the name of each test includes the test series, cell pressure, and q/p'_{max} (for only Series 1 and 3). There are special terms in some tests in Series 3: (I) and (UPT). These indicate that image analysis and ultrasonic proximity transducer were used to measure volume change, respectively.

Series 1 was to observe the repeatability of the cyclic triaxial test. The tests in this series were performed only on granite A as it was the only available material at that time. According to the visual observation, breakage from the tests in Series 1 is minimal probably due to the material properties of granite A. As the main theme of the project is ballast degradation, a larger amount of ballast breakage was needed. Therefore, the material was changed to limestone due to its larger values of LAA and MDA compared to those of granite A.

The tests in Series 2 were monotonic triaxial tests on limestone ballast. It should be noted that all tests in Series 2 were performed without the differential pressure transducer as it was sent for repair. Furthermore, the image analysis and the UPT had not been developed for testing at that time. As a result, the sample volume change was obtained from reading the water level on the scale of the inner cell neck.

The first test of Series 2 was performed without the inner cell. This was to check if the sample was going to touch the inner cell due to its radial expansion. As a result, sample volume change cannot be obtained. In this test, air was used as the confining medium as water would distort the visual observation of the radial expansion. The cell pressure of 10 kPa was chosen to obtain a large radial expansion. It was found that the sample can be loaded to 12 % axial strain without touching the inner cell. After this test, three more monotonic tests with cell pressures of 10, 30, and 60 kPa were performed.

Different cyclic triaxial tests were performed on limestone in Series 3. Three tests in this series were performed with image analysis. One test in this series was performed with the UPT. However, the transducer was used until cycle 2,000 as it was found that the upper shaft supporting the load cell was moving laterally as it was not supported by the cell top bearing. At that time, the differential pressure transducer had just come back from repair. It was therefore used to measure the sample volume change in the later part of the test and the other tests in this series.

Test series	No. of test	Test number	Cell pressure (kPa)	Maximum deviatoric stress (kPa)	q/p'_{max}	Volume change measure-ment method	Density (kg/m^3)
1 (Cyclic test on granite A)	8	S1-90/1.5a	90	270	1.5	DPT*	1,506
		S1-90/1.5b	90	270	1.5	DPT*	1,579
		S1-90/1.5c	90	270	1.5	DPT*	1,554
		S1-90/1.5d	90	270	1.5	DPT*	1,509
		S1-90/1.5e	90	270	1.5	DPT*	1,515
		S1-90/1.5f	90	270	1.5	Scale**	1,515
		S1-90/1.5g	90	270	1.5	Scale**	1,515
		S1-90/1.5h	90	270	1.5	Scale**	1,515
2 (Monotonic test on limestone)	4	S2-10a	10	N/A	N/A	None	1,551
		S2-10b	10	N/A	N/A	Scale**	1,511
		S2-30	30	N/A	N/A	Scale**	1,539
		S2-60	60	N/A	N/A	Scale**	1,545
3 (Cyclic test on limestone)	8	S3-30/1.7(I)	30	117.7	1.7	Image analysis	1,517
		S3-30/2.0a(I)	30	180	2.0	Image analysis	1,549
		S3-60/1.5a(I)	60	180	1.5	Image analysis	1,553
		S3-30/2.0b (UPT)	30	180	2.0	UPT and DPT***	1,559
		S3-60/1.5b	60	180	1.5	DPT*	1,600
		S3-60/2.0a	60	360	2.0	DPT*	1,575
		S3-10/2.0	10	60	2.0	DPT*	1,539
		S3-60/2.0b	60	360	2.0	DPT*	1,592

* Volume change is measured by the differential pressure transducer.

** Volume change is measured by reading water level on scale of the inner cell neck.

*** The volume change during the first 2,000 cycles was measured by the ultrasonic proximity transducer. After that, the differential pressure transducer was used instead due to the problem mentioned in Section 5.4.3.

Table 5.1. List of triaxial tests performed in this project

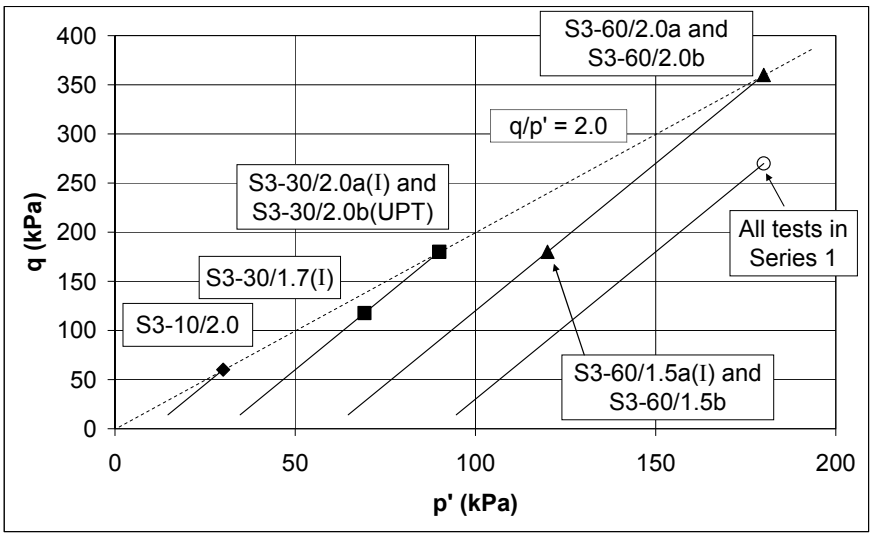

Figure 5.16. q-p' stress paths of cyclic triaxial tests (Series 1 and 3)

5.7. Results

5.7.1. Series 1 – Repeatability of cyclic triaxial test

Eight cyclic triaxial tests on granite A with cell pressure of 90 kPa and q/p'_{max} of 1.5 were performed in Series 1 to observe the test repeatability. Normally, at least three tests should be enough to observe the repeatability. However, due to errors in volume change measurement and problems with the differential pressure transducer, the tests had to be repeated more than three times.

According to Fair (2003), the permanent axial strains from cyclic triaxial tests on ballast from similarly prepared tests are not consistent. The cause of this discrepancy is the bedding errors occurring during the first cycle. Following that, the permanent axial strains of the first cycles from all tests in Series 1 were removed.

Figure 5.17 shows the permanent axial strain from the tests. It should be noted that wrong parameter was input before performing cycle 500 in test S1-90/1.5a. As a result, the sample was overly compressed and the permanent axial strain rises as shown in Figure 5.17b. Following Fair (2003), error bars are included in Figure 5.17c. They represent the standard error from the mean (*S.E.*). The definition of the standard error is shown in Equation 5.1. Fair (2003), stated that the results from samples that were prepared and tested in the same way is 95% probable to fall somewhere in the range of the error bar.

$$S.E. = \frac{S}{\sqrt{n}} \tag{5.1}$$

where $S.E.$ = Standard error

S = Standard deviation

n = Number of samples

It should be noted from Figure 5.17a that the permanent axial strain from test S1-90/1.5b is significantly lower than the other tests. Moreover, Figure 5.17b shows that the permanent axial strain of S1-90/1.5a is also significantly lower than the other tests. Therefore, the permanent axial strains from S1-90/1.5a and b were not included in the calculation of the average and standard error in Figure 5.17c. Furthermore, the results from tests S1-90/1.5e and S1-90/1.5h stop at cycles 20,000 and 50,000 due to a software fault.

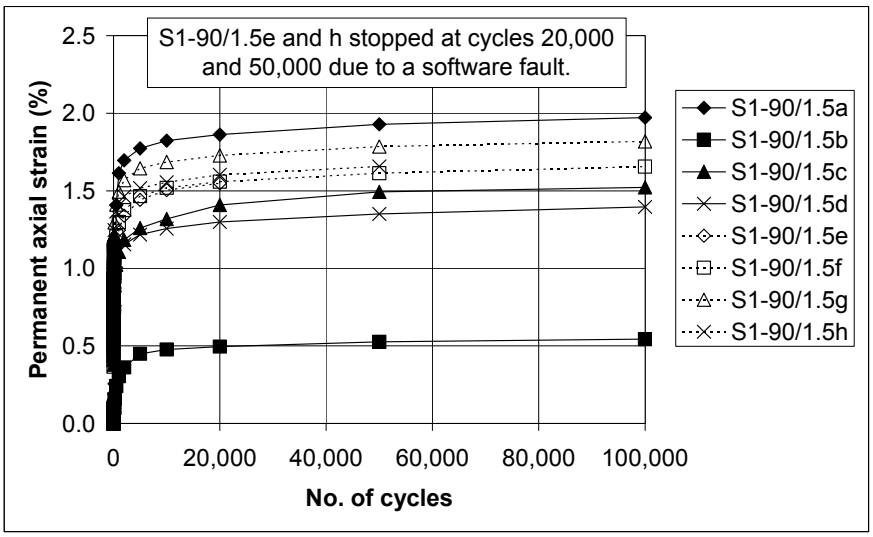

Figure 5.17(a). Permanent axial strain in Series 1

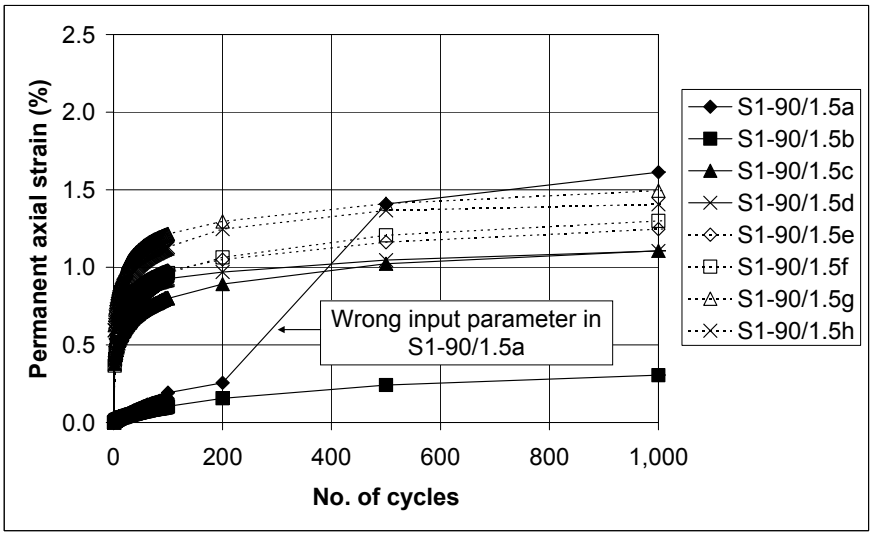

Figure 5.17(b). Permanent axial strain in Series 1 (up to cycle 1,000)

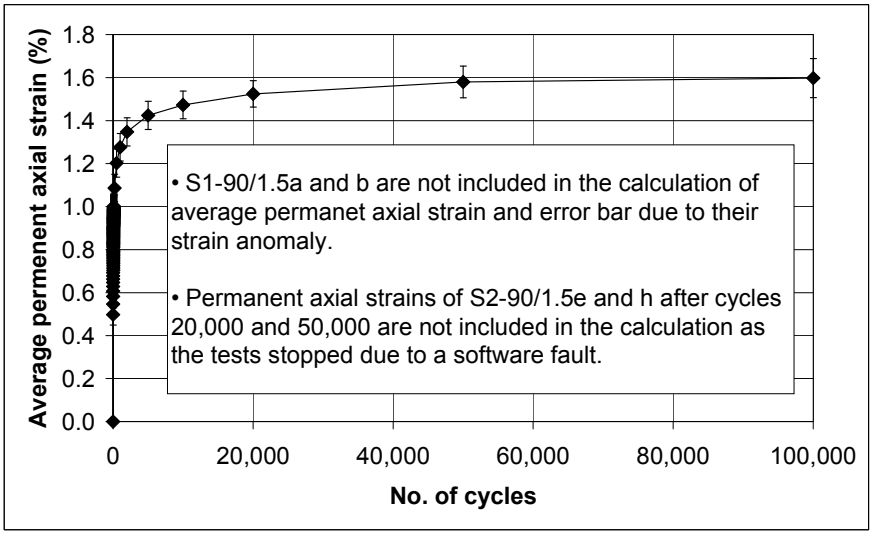

Figure 5.17(c). Average permanent axial strain in Series 1 with error bars

Figure 5.17. Permanent axial strain in Series 1

The error bar approach was also performed on the permanent volumetric strain, resilient modulus, and Poisson's ratio. The resilient modulus and Poisson's ratio are calculated by the formulae shown in Equations 5.2 and 5.3. The graphs are shown from Figure 5.18 to Figure 5.20.

$$M_r = \frac{q_{\max} - q_{\min}}{\varepsilon_{a,r}} = \frac{\left[\frac{F}{A_0}\left(\frac{1-\varepsilon_a}{1-\varepsilon_v}\right)\right]_{\max-\min}}{\varepsilon_{a,r}} \qquad (5.2)$$

$$\nu = \frac{\varepsilon_{r,r}}{\varepsilon_{a,r}} = \frac{\left(\frac{\varepsilon_{v,r} - \varepsilon_{a,r}}{2}\right)}{\varepsilon_{a,r}} = \frac{\varepsilon_{v,r} - \varepsilon_{a,r}}{2\varepsilon_{a,r}} \qquad (5.3)$$

where M_r = Resilient Modulus

$q_{\max}$ = Maximum deviatoric stress in a cycle

$q_{\min}$ = Minimum deviatoric stress in a cycle

$\varepsilon_{a,r}$ = Resilient axial strain

F = Applied force

A_0 = Initial cross sectional area of the sample

ε_a = Axial strain

ε_v = Volumetric strain

$\varepsilon_{r,r}$ = Resilient radial strain

$\varepsilon_{v,r}$ = Resilient volumetric strain

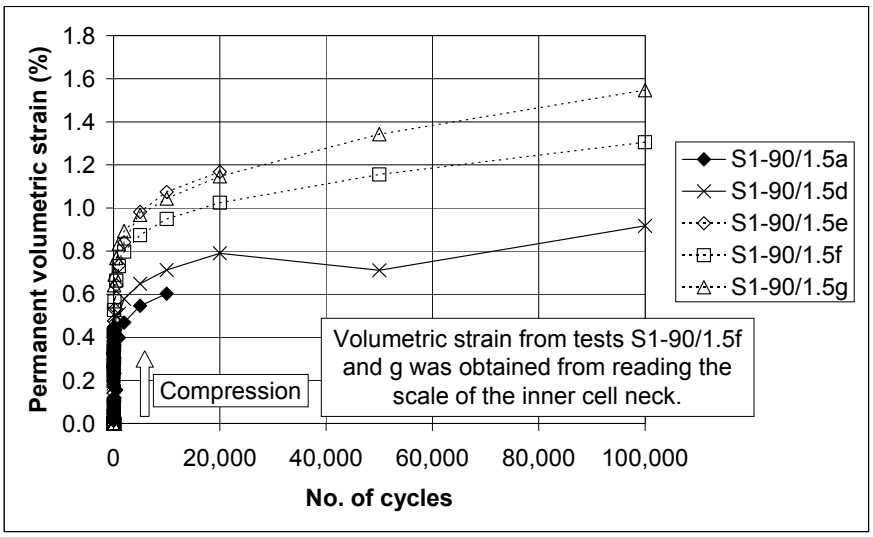

Figure 5.18(a). Permanent volumetric strain in Series 1

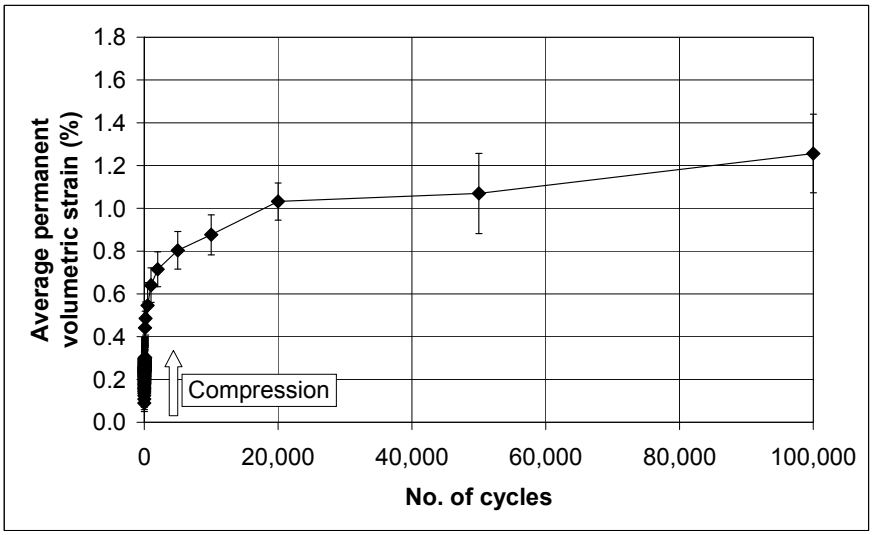

Figure 5.18(b). Average permanent volumetric strain in Series 1 with error bars

Figure 5.18. Permanent volumetric strain in Series 1

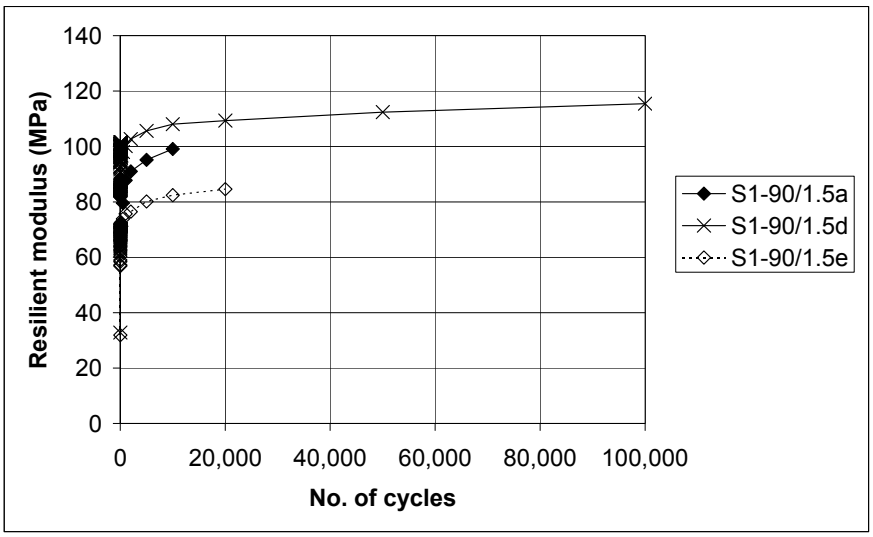

Figure 5.19(a). Resilient modulus in Series 1

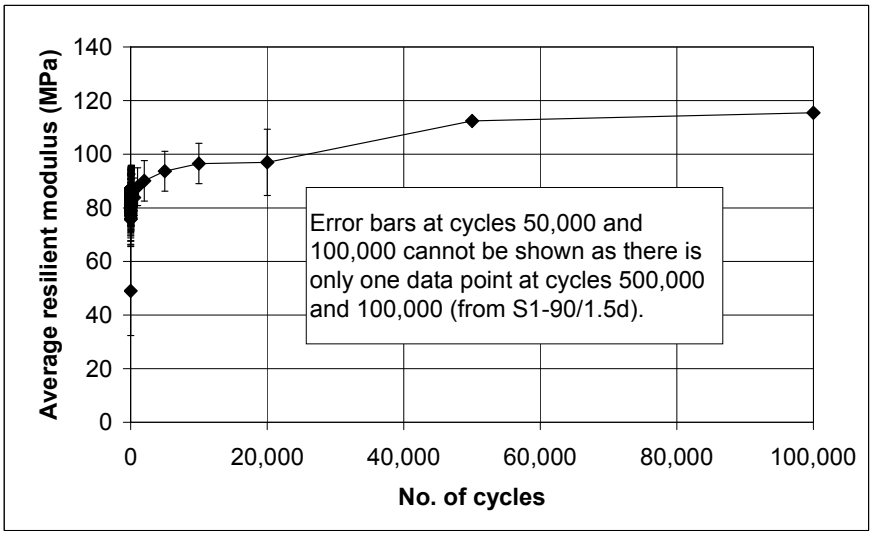

Figure 5.19(b). Average resilient modulus in Series 1 with error bars

Figure 5.19. Resilient modulus in Series 1

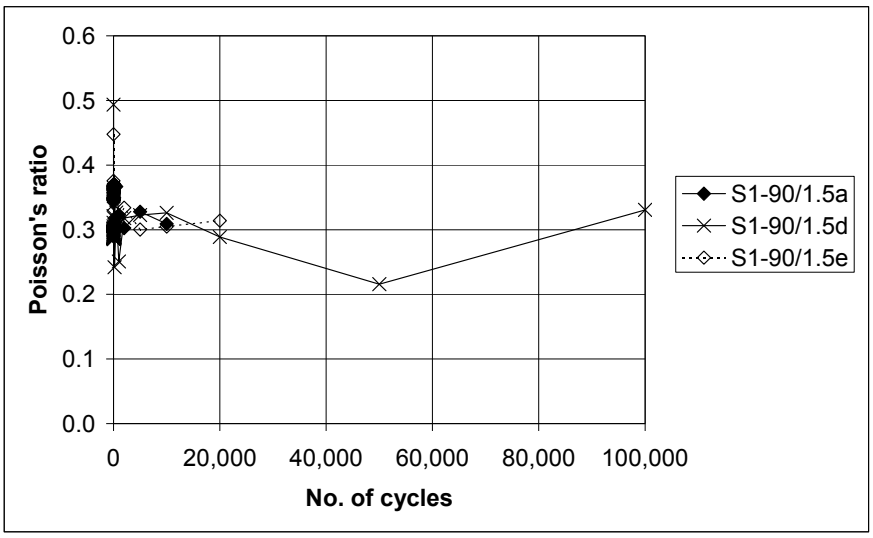

Figure 5.20(a). Poisson's ratio in Series 1

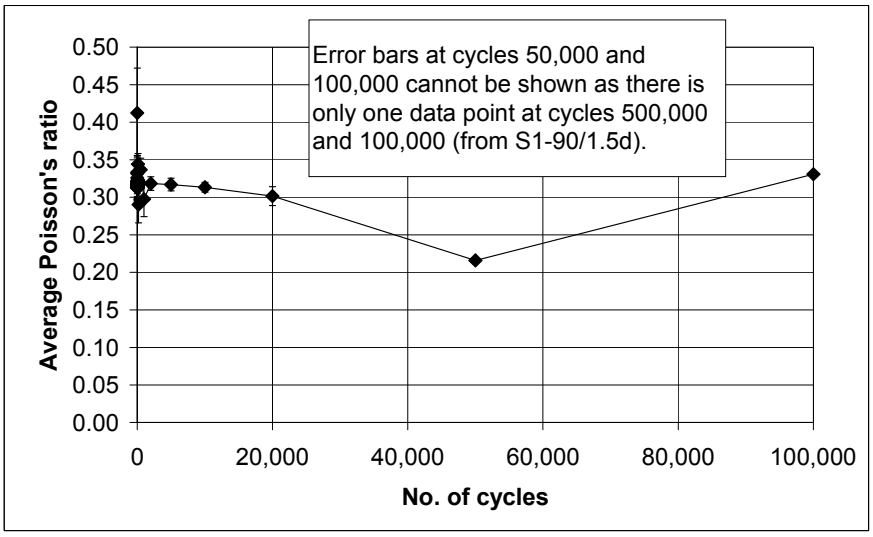

Figure 5.20(b). Average Poisson's ratio in Series 1 with error bars

Figure 5.20. Poisson's ratio in Series 1

It should be noted from Figure 5.18 that

- The results from test S1-90/1.5a stop at cycle 10,000. This is because as the sample contracted, water needed to be added into the inner cell during the test to keep the water level in the measurable range of the differential pressure transducer. In this test, cycles 10,001 to 19,999 were performed with frequency of 4 Hz which was too fast for the

differential pressure transducer to register the sample volume change. After cycle 19,999, the water level was almost out of the measurable range. Water was then added right away before reading the volume change due to cycles 10,000 to 19,999. Therefore, the track of volume change was lost and later volume change of the sample could not be obtained.

- The results from tests S1-90/1.5b and c are not presented because the sample volume changes in these tests did not follow the expected sinusoidal response. An example was shown in Figure 5.4. As a result, the volumetric strain could not be obtained from both tests. This behaviour was found to occur randomly and did not happen in any other tests in this Series.
- The results from test S1-90/1.5e stop at cycle 20,000 because the test stopped itself due to a software fault.
- The volumetric strain could not be measured in test S1-90/1.5h because the water in the inner cell dropped below the measurable range somewhere between cycle 1 and 99. As a result, the track of volume change was lost and the volume change could not be measured afterwards.

It should be noted from Figure 5.19 (resilient modulus) and Figure 5.20 (Poisson's ratio) that

- Only test results from S1-90/1.5a, d and e are presented in both figures. This is because these three tests are the only tests that the resilient volumetric strain could be measured.

- The big drop in Poisson's ratio in test S1-90/1.5d was probably due to the electrical drift from the differential pressure transducer as explained in Section 5.4.1.

Figure 5.21 shows the particle size distribution after the tests. Similar to the RTF results, no particles smaller than 22.4 mm were in each sample before the test and only the particle size distribution of particles smaller than 22.4 mm is shown in mass passing instead of percentage passing. As the initial mass of each test is similar, the behaviour from Figure 5.21 is similar to a degradation plot using percentage passing. Only the first four tests of Series 1 are presented because after the first four tests, the degradation on the sample could not be seen by visual observation and it was felt that the subsequent tests needed to be performed as quickly as possible. As a result, the same material was used for all subsequent tests (tests S1-90/1.5e to h) and was thrown away afterwards as the degradation obtained after the test would be the accumulation from those tests.

It can be seen from Figure 5.21 that the degradation from test S1-90/1.5b are much larger than the others. Both permanent axial strain and degradation from this test are significantly different from the other tests in this series. The cause of this discrepancy is still unknown but the degradation from this test will also be treated as an anomaly. Even though the sample in S1-90/1.5a was overly compressed, the degradation is not significantly different from S1-90/1.5c and d and it can be concluded that the degradation from the tests is also repeatable.

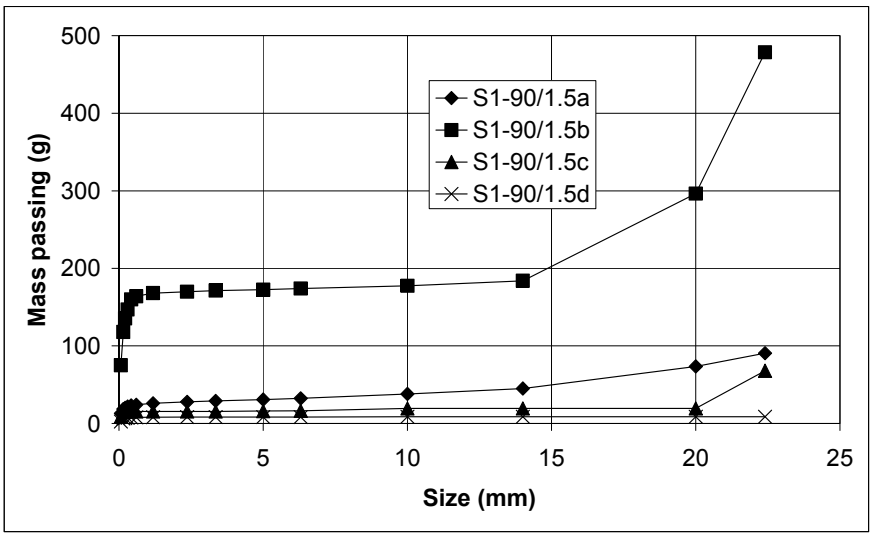

Figure 5.21. Particles smaller than 22.4 mm from the tests in Series 1

5.7.2. Series 2 – Monotonic triaxial tests on limestone

Four monotonic tests on limestone ballast have been carried out in Series 2, two with confining pressure of 10 kPa (S2-10a and S2-10b), one with confining pressure of 30 kPa (S2-30), and the last one with confining pressure of 60 kPa (S2-60). Initially, the confining stresses of 10, 30, and 90 kPa were intended to be used in both monotonic and cyclic triaxial tests on limestone (series 2 and 3) to cover a big range of confining stress. However, limestone sample usually punctured the membrane when the confining stress was 90 kPa. Therefore, the confining stresses were then changed to 10, 30, and 60 kPa.

It should be noted that test S2-10a was performed without the inner cell and water to check if the sample was going to touch the inner cell when it bulged. Therefore, the volumetric strain cannot be obtained from that test.

Figure 5.22 and Figure 5.23 show the plot of deviatoric stress against axial strain and *q-p'* stress paths from the tests in Series 2. Test S2-10a is not included in the figures because volumetric strain is required to calculate the deviatoric stress according to Equation 5.2. It can be seen from Figure 5.22 that the deviatoric stress eventually becomes stable but does not significantly drop. This suggests that each sample reached its peak strength but not the ultimate strength.

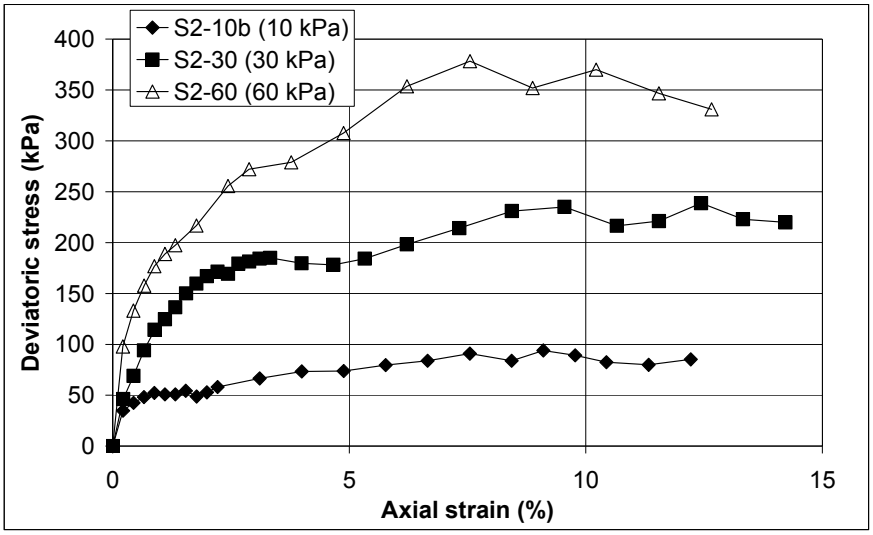

Figure 5.22. Deviatoric stress vs axial strain from monotonic triaxial tests on limestone (Series 2)

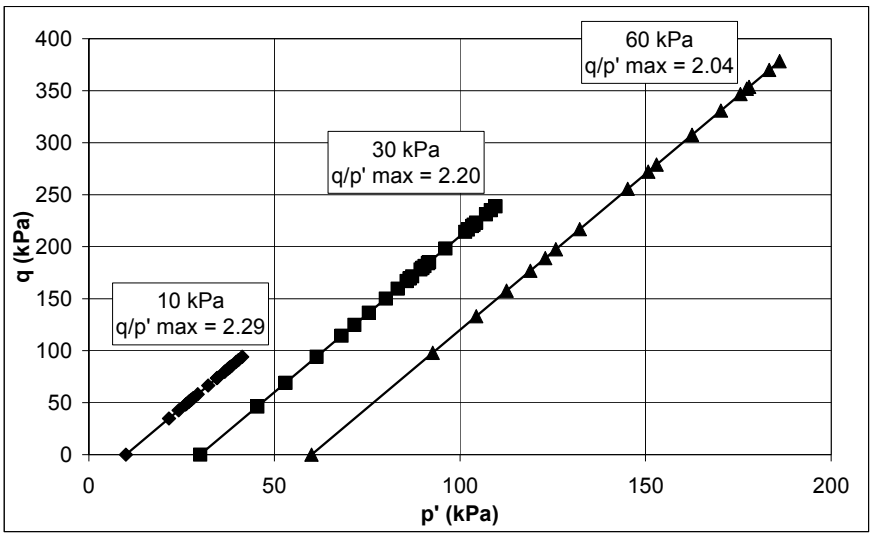

Figure 5.23. q-p' stress paths in Series 2

The stiffness of a test sample is defined by two parameters; the tangent modulus at zero axial strain and secant modulus. Tangent modulus (E_t) at zero axial strain is the slope at the initial portion of the curve of deviatoric stress against axial strain (i.e., Figure 5.22) and secant modulus is the slope of the line joining the origin to any point of the curve. Both moduli are illustrated in Figure 5.24. Secant modulus (E_s) was calculated at deviatoric stresses of 60, 117.7, 180, and 360 kPa as these were the maximum deviatoric stresses in the cyclic tests on limestone (Series 3). Table 5.2 summarises the moduli obtained from the curves in Figure 5.22.

Figure 5.25 shows the plot between volumetric strain and axial strain. The volumetric strain was obtained from reading the scale of the inner cell as the differential pressure transducer was sent for repair at that time. It can be seen from the figure that after a short period of volumetric compression, the sample began to dilate. The test with 10 kPa has the largest dilation corresponding to

its largest q/p'_{max} according to Figure 5.23. Also, Figure 5.26 shows the Mohr-Coulomb curved envelope attributed to dilation for the tests in Series 2.

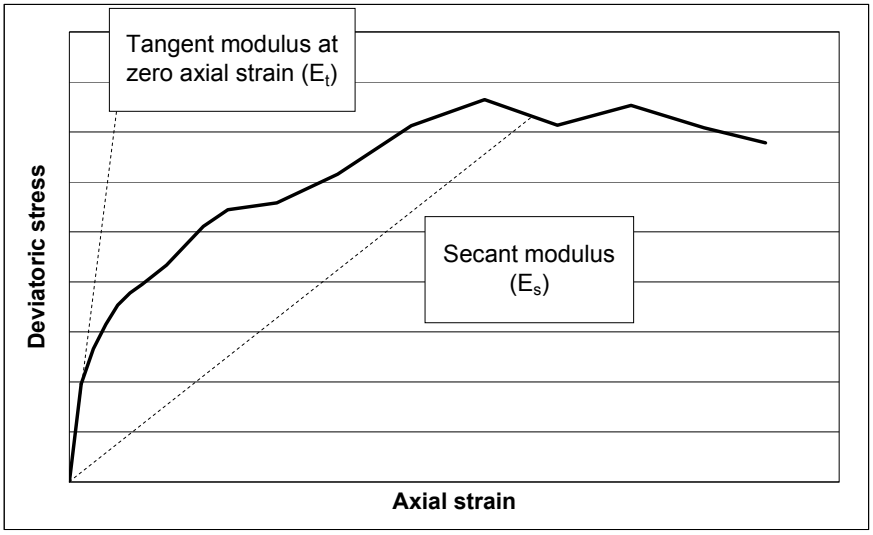

Figure 5.24. Definition of tangent modulus at zero axial strain (E_t) and secant modulus (E_s)

Test	Cell pressure (kPa)	Tangent modulus at zero axial strain (MPa)	Secant moduli at different deviatoric stress (MPa)			
			At 60 kPa deviatoric stress	At 117.7 kPa deviatoric stress	At 180 kPa deviatoric stress	At 360 kPa deviatoric stress
S2-10b	10	16	2	N/A	N/A	N/A
S2-30	30	21	17	12	7	N/A
S2-60	60	45	45	35	19	5

Table 5.2. Tangent modulus at zero axial strain and secant moduli from Series 2

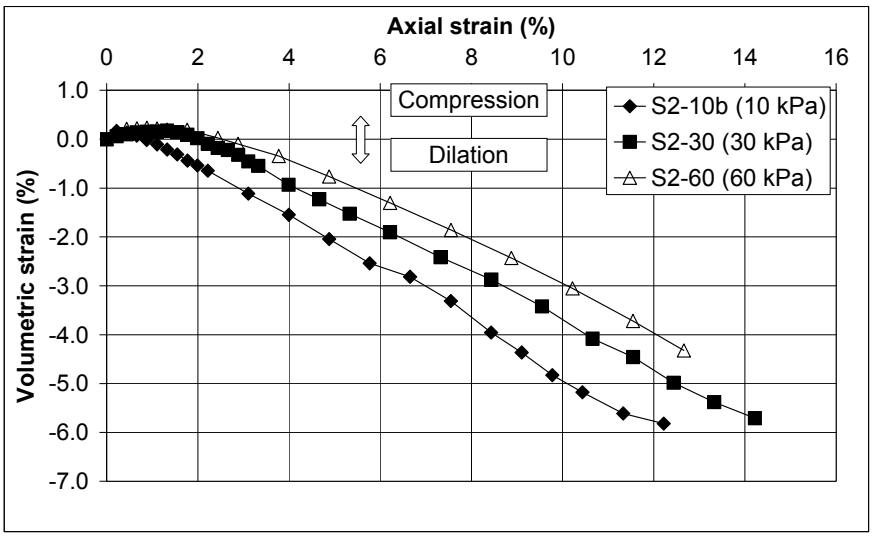

Figure 5.25. Volumetric strain vs axial strain from Series 2

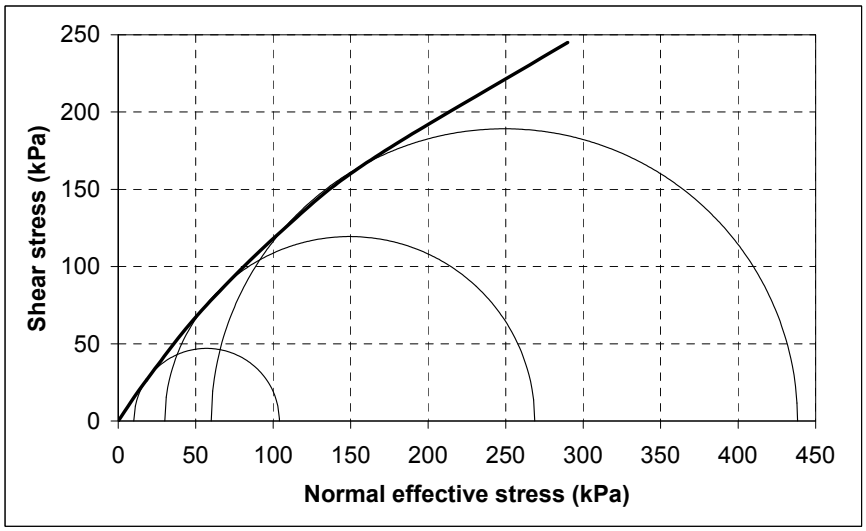

Figure 5.26. Mohr-Coulomb failure envelope of the limestone ballast for Series 2

Figure 5.27 shows the particle size distributions of the samples after the monotonic tests. The particle size distribution of test S2-10a is also shown in the figure as this result does not relate to the volume change measurement. It can be seen from the figure that the breakage increases with increasing cell pressure. This finding agrees with Key (2003) and Indraratna et al. (1998).

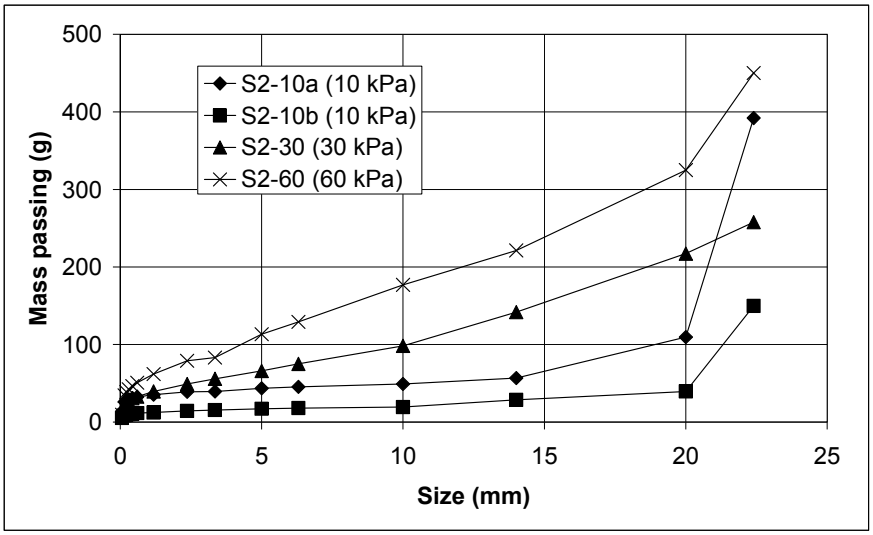

Figure 5.27. Particles smaller than 22.4 mm from the tests in Series 2

5.7.3. Series 3 – Cyclic triaxial tests on limestone

Eight cyclic triaxial tests on limestone were carried out in Series 3. Similar to Series 1, the first cycle permanent axial strains from all tests in Series 3 were removed. For comparative purposes, the eight tests are grouped in different ways in the figures namely, results from tests with cell pressure of 30 kPa, cell pressure of 60 kPa, q/p'_{max} of 2, and maximum deviatoric stress of 180 kPa. It should be noted that there are no separate plots for the results from tests with a cell pressure of 10 kPa in the figures as there was only one such test in Series 3. Furthermore, there are no separate plots for permanent volumetric strain, resilient modulus, and Poisson's ratio from tests with cell pressure of 30 kPa. This is because these parameters are related to the volume change measurement as mentioned earlier and there was only one test in Series 3 a with cell pressure of 30 kPa that had a valid volume change measurement (S3-30/2.0b(UPT)). The other tests with 30 kPa cell pressure (S3-30/1.7(I) and S3-

30/2.0(I)) were performed with image analysis which could not measure volume change accurately.

It can be seen from Figure 5.28 (permanent axial strain against number of cycles) that:

- It should be noted that the permanent axial strain results presented in the image analysis section (Section 5.4.2) are from tests S3-30/1.7(I), S3-30/2.0a(I), and S3-60/1.5a(I). However, the permanent axial strains from those tests presented in Figure 5.9a, Figure 5.10a, and Figure 5.13a are different. This is because the first cycle permanent axial strains were not removed from those results.
- For tests with the same cell pressure and stress ratio (e.g. S3-30/2.0a(I) and S3-30/2.0b(UPT) or S3-60/1.5a(I) and S3-60/1.5b), there are some discrepancies in permanent axial strain. However, the level of discrepancy is the same as the permanent axial strains from the tests in Series 1.
- With the same cell pressure, permanent axial strain increases with q/p'_{max}.
- With the same q/p'_{max}, the sample contracts more with increasing cell pressure.
- With the same maximum deviatoric stress, permanent axial strain increases with increasing q/p'_{max}.

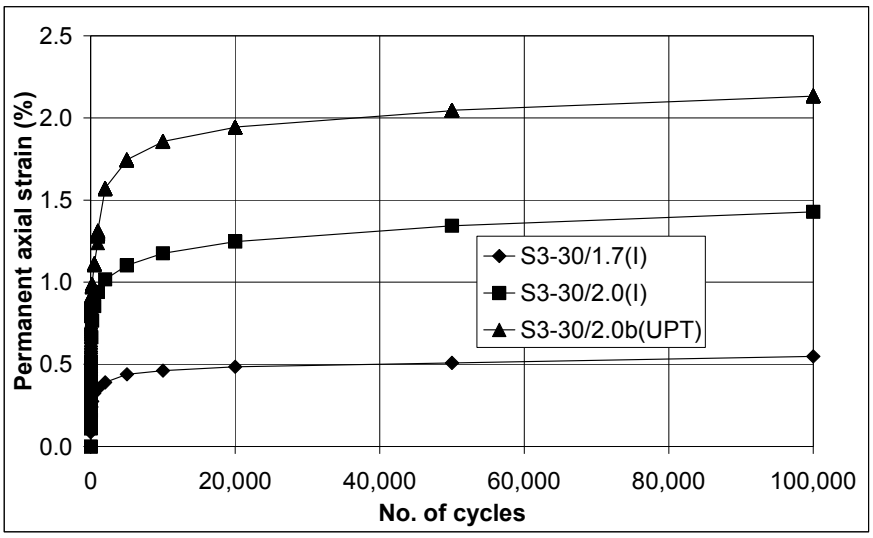

Figure 5.28(a). Permanent axial strains from tests with cell pressure of 30 kPa

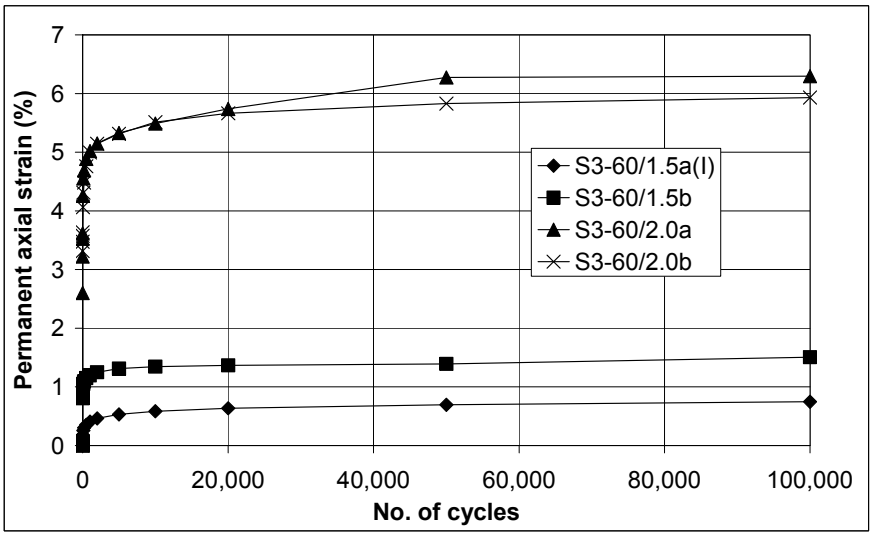

Figure 5.28(b). Permanent axial strains from tests with cell pressure of 60 kPa

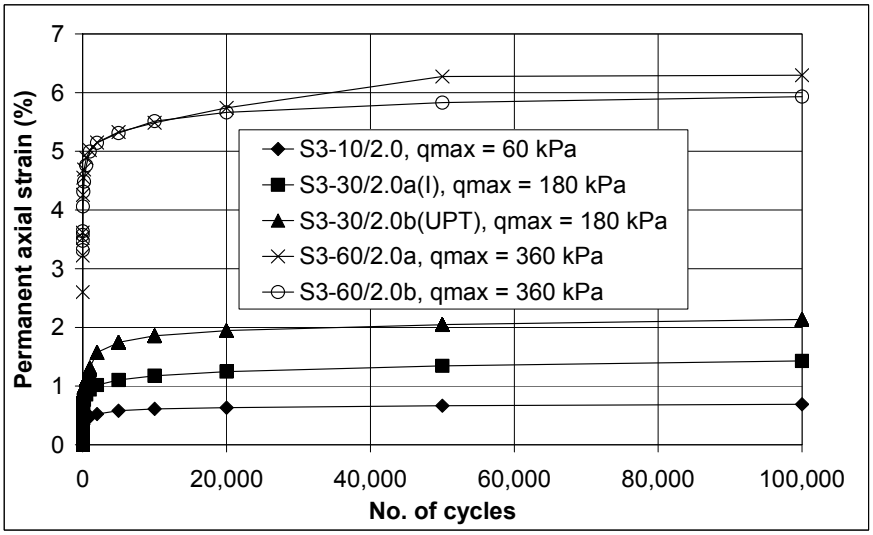

Figure 5.28(c). Permanent axial strains from tests with q/p'_{max} of 2.0

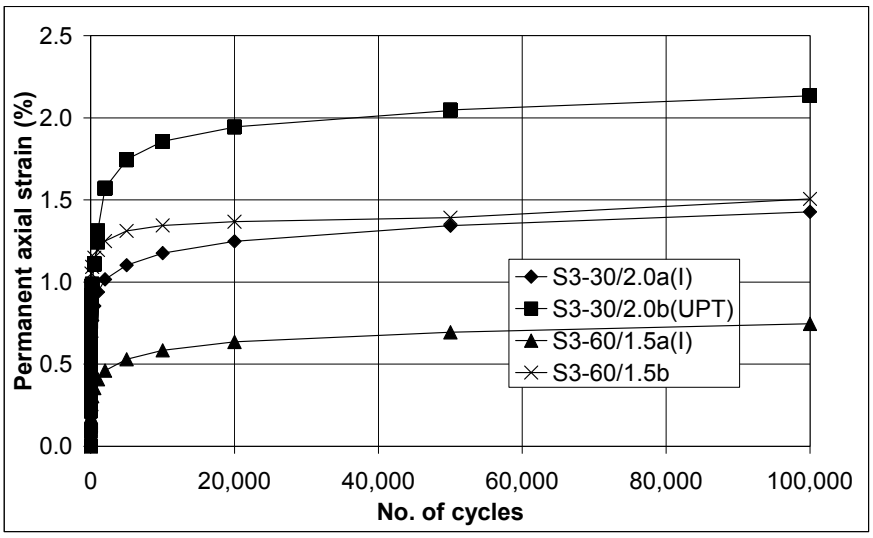

Figure 5.28(d). Permanent axial strains from tests with max deviatoric stress of 180 kPa

Figure 5.28. Permanent axial strain from the tests in Series 3 (a) – (d)

It can be seen from Figure 5.29 (permanent volumetric strain against number of cycles) that:

- The samples from S3-60/2.0a and b dilated at the beginning of the tests (negative permanent volumetric strain). This might be because the maximum deviatoric stress in these tests (360 kPa) was equal to the maximum deviatoric stress in the monotonic test with 60 kPa (S2-60). After the first few cycles, the samples started to contract.
- The permanent volumetric strain from S3-60/2.0a was found to dilate again after 20,000 cycles. Theoretically, this is not possible. Therefore, test S3-60/2.0b was performed to check if this behaviour was repeatable. It was found that this behaviour was not seen in S3-60/2.0b. Even though the behaviours of permanent volumetric strains of both tests are different, the permanent axial strains are the same (Figure 5.29a).

- According to Figure 5.29a, the permanent volumetric strain seems to increase with decreasing q/p'_{max} under the same confining stress. However, Suiker et al. (2005) found that with the same cell pressure, there is no definite trend for permanent volumetric strain against q/p'_{max}.
- Only S3-10/2.0 shows dilative behaviour.
- With the same q/p'_{max}, the permanent volumetric strain should increase with increasing cell pressure. However, the strain from S3-60/2.0b is less than S3-30/2.0b (Figure 5.29b). This is probably due to the dilation at the beginning of S3-60/2.0b.
- With the same maximum deviatoric stress, the permanent volumetric strain here seems to increase with decreasing cell pressure in Figure 5.29c. This contradicts with the findings of Indraratna et al. (2005) as they found that the sample became more compressive with increasing cell pressure. However, this is not generally true as Fair (2003) found that there was no definite trend for permanent volumetric strain against cell pressure with the same maximum deviatoric stress.

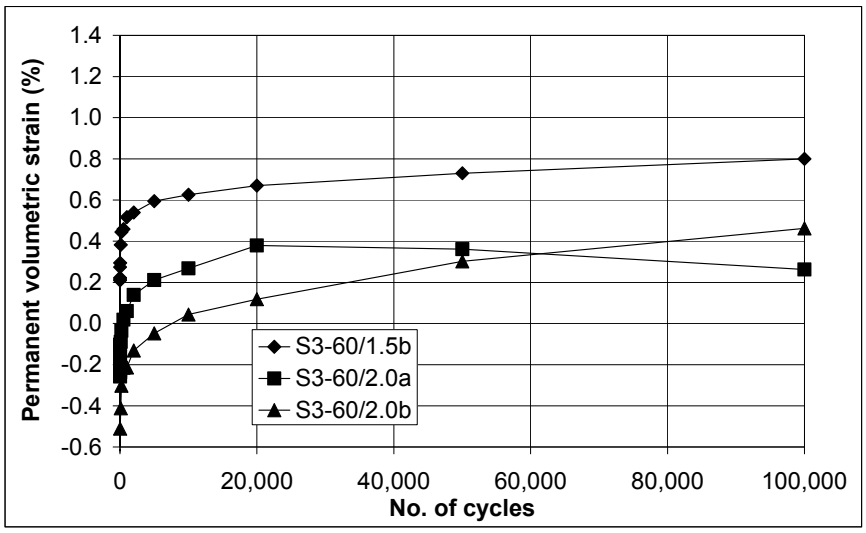

Figure 5.29(a). Permanent volumetric strains from tests with cell pressure of 60 kPa

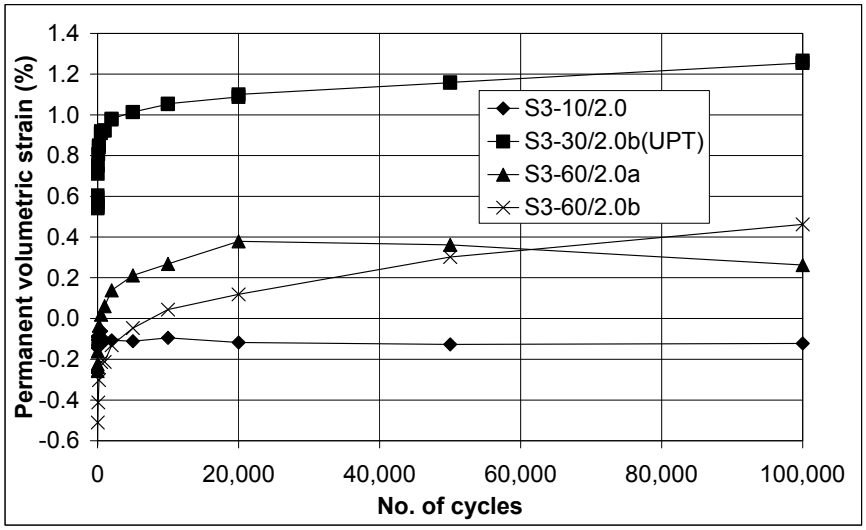

Figure 5.29(b). Permanent volumetric strains from tests with q/p'_{max} of 2.0

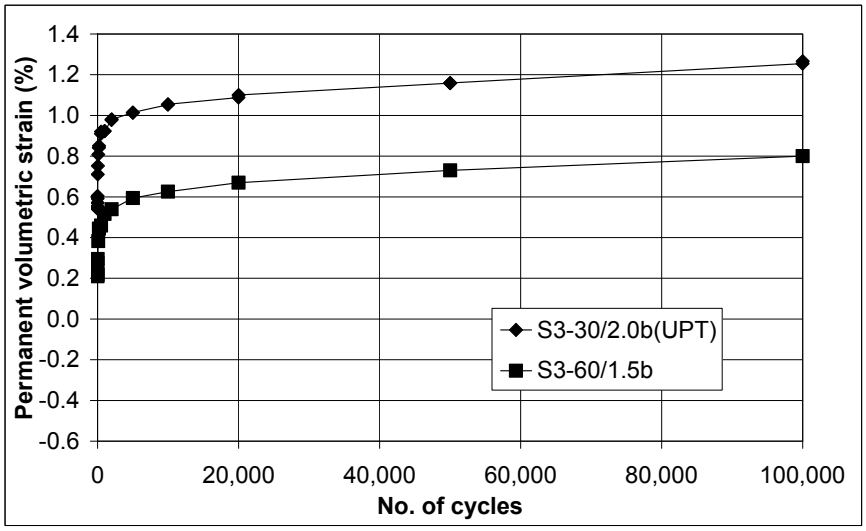

Figure 5.29(c). Permanent volumetric strains from tests with max deviatoric stress of 180 kPa

Figure 5.29. Permanent volumetric strain from the tests in Series 3

Figure 5.30 shows the resilient modulus from the tests in Series 3. As the resilient modulus was found to follow the K-θ model as stated in Section 2.6.1.1, the sum of principle stresses (θ) for each test is also indicated in the plot. Also, the final resilient modulus is plotted against the sum of principal stress together with the K-θ model in Figure 5.31. According to the figure, both empirical constants k_1 and k_2 are 9.2 and 0.5.

Figure 5.32 shows the plots between Poisson's ratio and the number of cycles. It can be seen that the Poisson's ratio increases with increasing maximum deviatoric stress (Figure 5.32a) and decreasing cell pressure (Figure 5.32b). This matches the findings from many researchers in the review of Lekarp et al. (2000a). However, the definite trend of Poisson's ratio cannot be found from the tests with q/p'_{max} of 2.0 (Figure 5.32c). The drift from S3-60/2.0b was probably due to the electrical drift from the differential pressure transducer again.

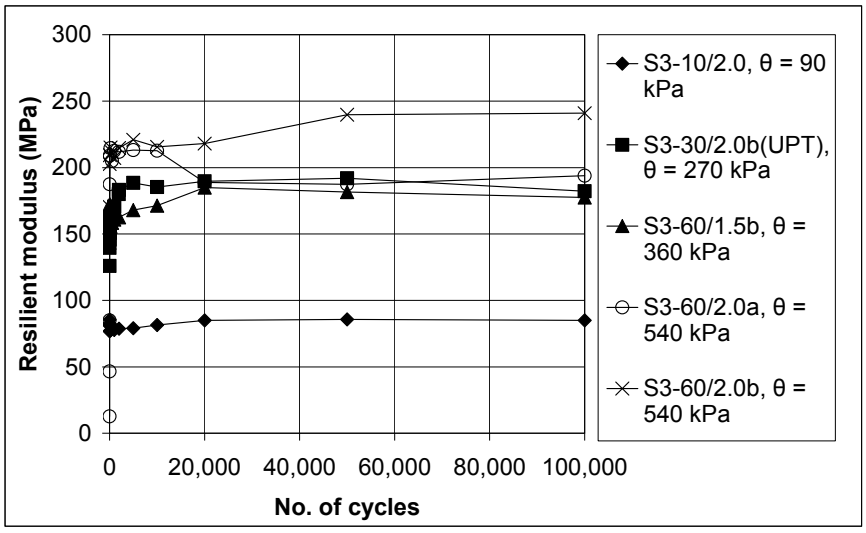

Figure 5.30. Resilient modulus from the tests in Series 3

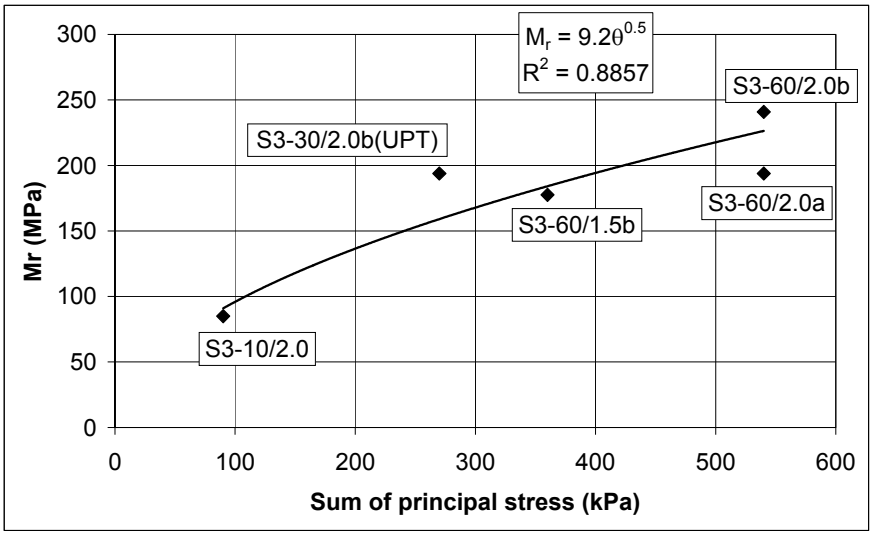

Figure 5.31. Resilient modulus vs sum of principle stress

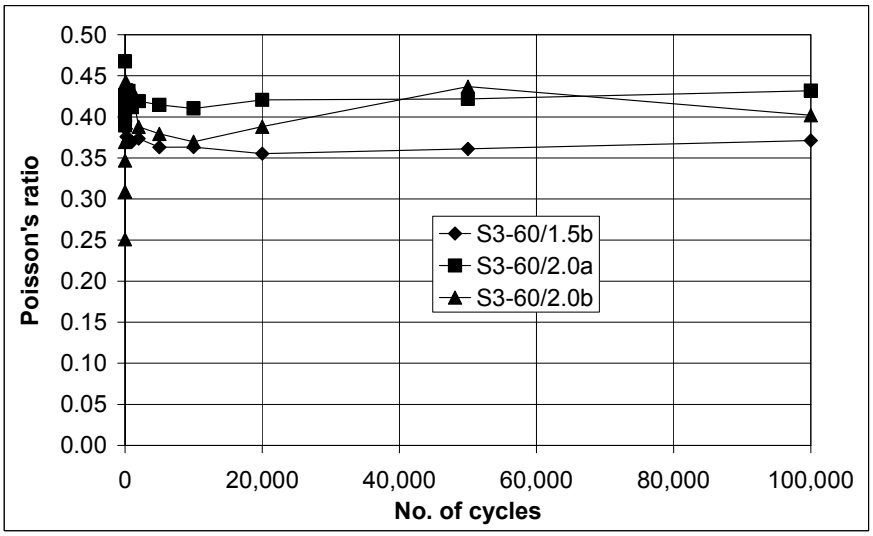

Figure 5.32(a). Poisson's ratio from tests with cell pressure of 60 kPa

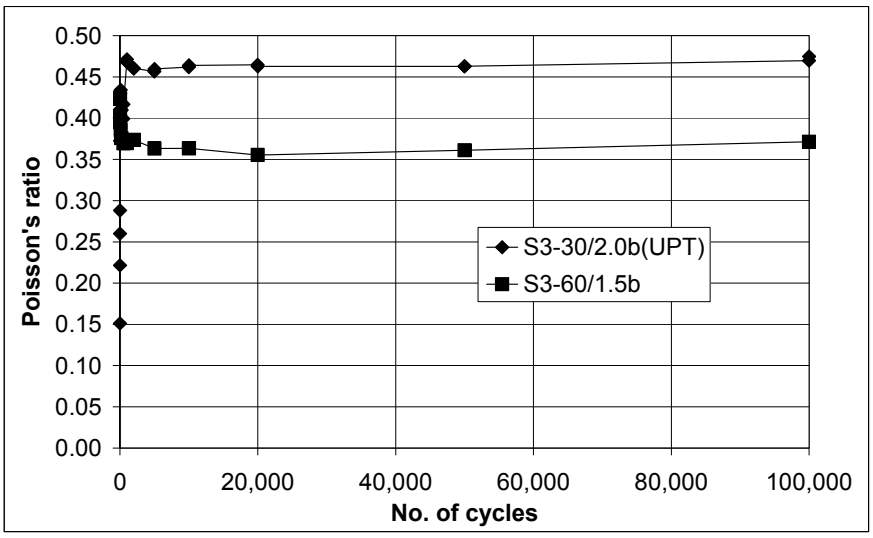

Figure 5.32(b). Poisson's ratio from tests with max deviatoric stress of 180 kPa

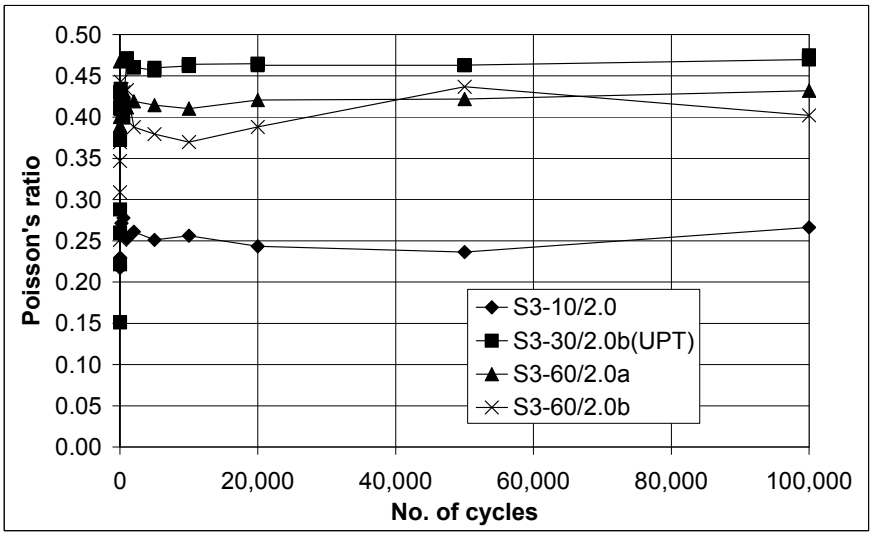

Figure 5.32(c). Poisson's ratio from tests with q/p'_{max} of 2.0

Figure 5.32. Poisson's ratio in Series 3

Figure 5.33 shows the particle size distribution after the tests in Series 3. It can be seen that with the same confining stress, breakage increases with increasing maximum deviatoric stress (Figure 5.33a and b). However, breakage from S3-30/1.7(I) is probably larger than it should have been (Figure 5.33a). This is because the sample was overly compressed due to the fast loading rate as stated in Section 5.4.2 (the first test with the image analysis).

It can be seen from Figure 5.33c that the breakage levels from all tests with maximum deviatoric stress of 180 kPa are not significantly different regardless of the confining pressure. This matches the findings of Indraratna et al. (2005). According to their triaxial tests on ballast, minimal breakage occurred when the confining pressure is between 30 and 75 kPa as shown in Figure 5.34. They defined this region as the optimum degradation zone or ODZ. It should be noted that the ballast breakage index in the figure indicates the breakage level based on calculation of area under the particle size distribution before and after each test as shown in Figure 5.35. It also can be seen from the Figure 5.34 that the breakage levels at different confining pressure in ODZ (zone II in the figure) are not significantly different.

The reason proposed by Indraratna et al. (2005) for the minimal breakage in the ODZ is that ballast particles are held together with sufficient confinement to provide optimum coordination number i.e., average number of contacts with neighbouring particles. Large breakage occurs when confining pressure is below 30 kPa due to dilative behaviour of the sample under small average coordination number. Moreover, breakage level increases when the confining pressure is above 75 kPa because of the increase in confining stress and because the coordination number has reached it maximum level.

According to Figure 5.33d, the breakage from tests with 60 kPa confining stress (S3-60/2.0a and S3-60/2.0b) is larger than the one with 30 kPa (S3-30/2.0a(I) and S3-30/2.0b(UPT)) due to large deviatoric stress in the tests with 60 kPa. Furthermore, the breakage from S3-10/2.0 is approximately equal to

S3-30/2.0a(I) even though the maximum deviatoric stress in S3-10/2.0 is much lower. This is because with dilative behaviour from test S3-10/2.0, the resulting breakage is large and comparable to the breakage from a test with higher deviatoric stress but in the optimum degradation zone.

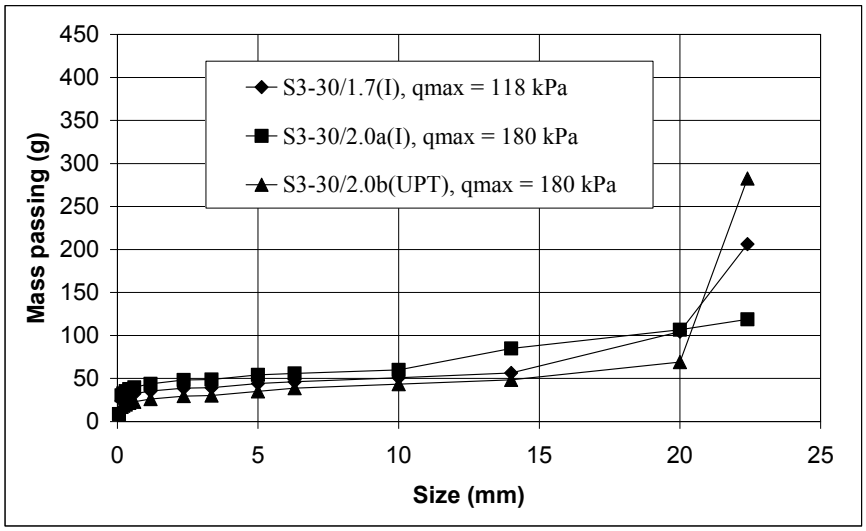

Figure 5.33(a). Particles smaller than 22.4 mm from tests with cell pressure of 30 kPa

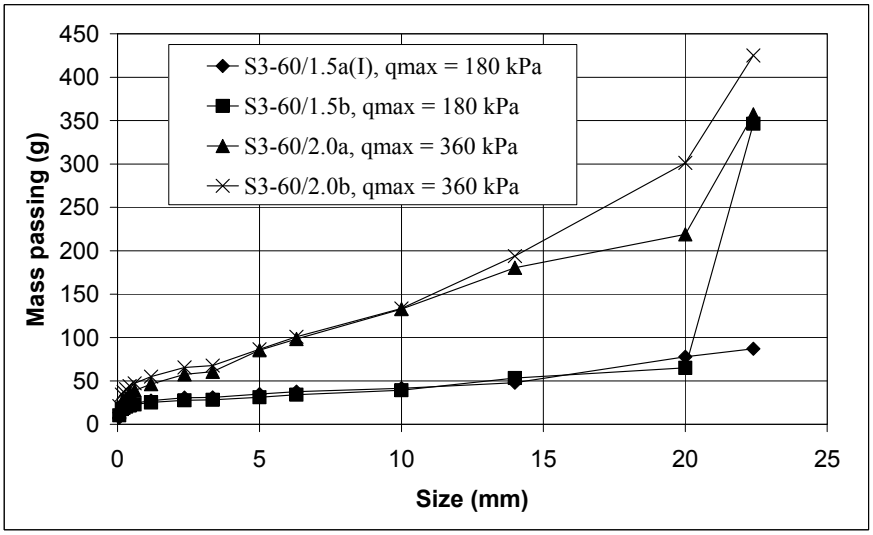

Figure 5.33(b). Particles smaller than 22.4 mm from tests with cell pressure of 60 kPa

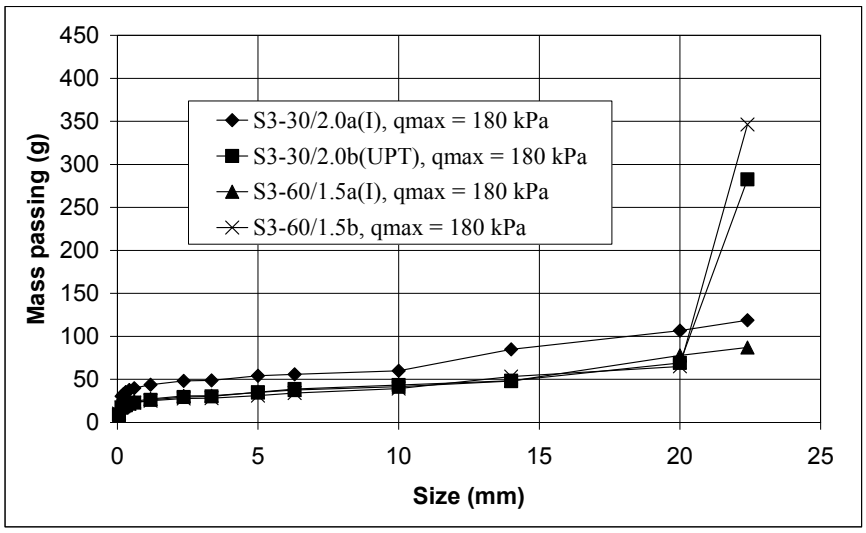

Figure 5.33(c). Particles smaller than 22.4 mm from tests with max deviatoric stress of 180 kPa

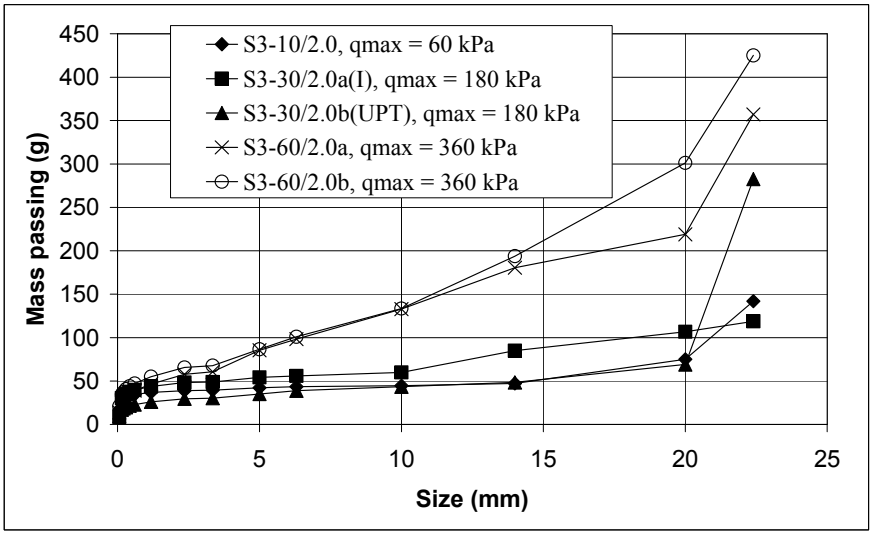

Figure 5.33(d). Particles smaller than 22.4 mm from tests with q/p'_{max} of 2

Figure 5.33. Particles smaller than 22.4 mm from the tests in Series 3 (a) – (d)

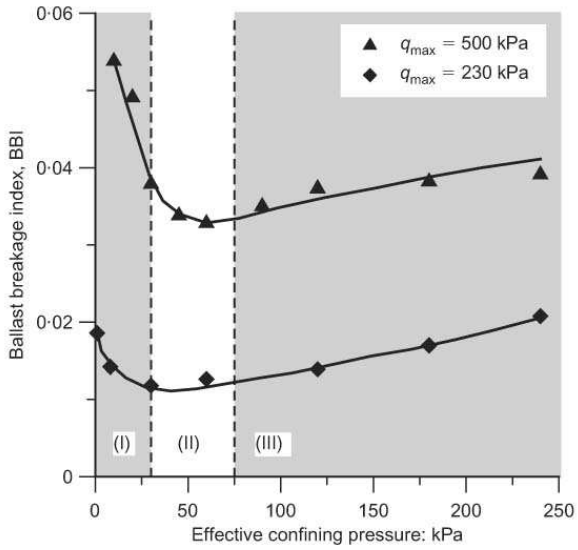

Figure 5.34. Effect of confining pressure on particle degradation (Indraratna et al, 2005)

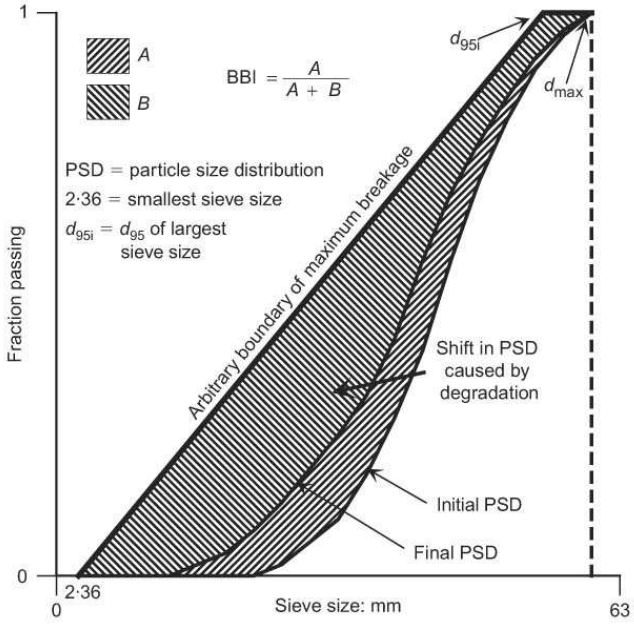

Figure 5.35. Ballast breakage index in Indraratna et al. (2005)

5.8. Discussion

The accuracy of the volume change measurement in this project was dependent on the differential transducer. The principle of using the water filled sample within an air pressurised outer cell so that sample volume change displaces

water in the inner cell is sound. However, the pressure differential caused by this volume change relative to the reference is very small so a sensitive transducer is necessary to detect the pressure change. The air pressure in the cell has to be well-controlled as varying air pressure can cause fluctuation of the water in the inner cell neck. Also, the free water surface in the neck will eventually become unstable with increasing loading frequency and surface tension where the water contacts the neck will cause drag on the movement of the water. These factors influence the response of the differential pressure transducer but it seemed to work reasonably well when used with extreme care.

The image analysis and ultrasonic level measurement were considered to have a potential to measure radial/volumetric strains. For the image analysis, GeoPIV could be adapted to analyse the permanent axial strain from the test very satisfactorily even though it is usually used with fine grain soil. However, further development is still needed for this method to analyse the resilient axial strain and both resilient and permanent radial strain.

It is difficult to observe the condition of the sample as the water in the inner cell distorts its shape particularly when trying to see if it has expanded against the wall of the inner cell or if the membrane is punctured. Furthermore, the outer cell is reinforced by circumferential strips of fibre (shown in Figure 5.1) and the top strip can be in the eye line for the reading of the water level in the inner cell neck.

An attempt was made to correlate the breakage and volumetric strain from the tests in Series 2 (monotonic tests on limestone) and 3 (cyclic tests on limestone). In Series 2, the correlation was made between mass passing 14 and 1.18 mm and the volumetric strain at 12 % axial strain as shown in Figure 5.36 while a correlation between mass passing 14 and 1.18 mm and the final permanent volumetric strain was made in Series 3 as shown in Figure 5.37. Due to the error in sample volume change of S3-60/2.0a (dilation after contraction of sample, see Figure 5.29), the results from this test are not included in the correlation. It also should be noted that all samples in Series 2 (monotonic tests on limestone) dilated while most samples in Series 3 (cyclic tests on limestone) contracted.

It can be seen from Figure 5.36 that a good correlation was obtained for the monotonic test results. Larger dilation is associated with smaller breakage. This matches the findings from Indraratna et al. (1998). This is probably because with large dilation, the particles in the sample can move around or rearrange more freely to avoid breakage. Particles in a monotonic test sample constantly rearrange themselves during the test as the diameter and volume of sample increase to compensate for the reduction of sample height. This is unlike a cyclic triaxial test where the particle rearrangement does not occur as much because maximum deviatoric stress is constant and permanent axial strain stay constant after a certain amount of load applications due to the shakedown concept.

The correlation from Series 3 (cyclic tests on limestone) in Figure 5.37 shows an opposite behaviour. If the results from the only dilative sample in this series (S3-10/2.0, see Figure 5.29b) are ignored in the correlation, it could be seen that the larger the compression, the smaller the breakage even though the correlation is not as good. However, the degradations from those tests are probably too small for its trend against the permanent volumetric strain to be observed as they are in the optimum degradation zone i.e., the middle zone in Figure 5.34.

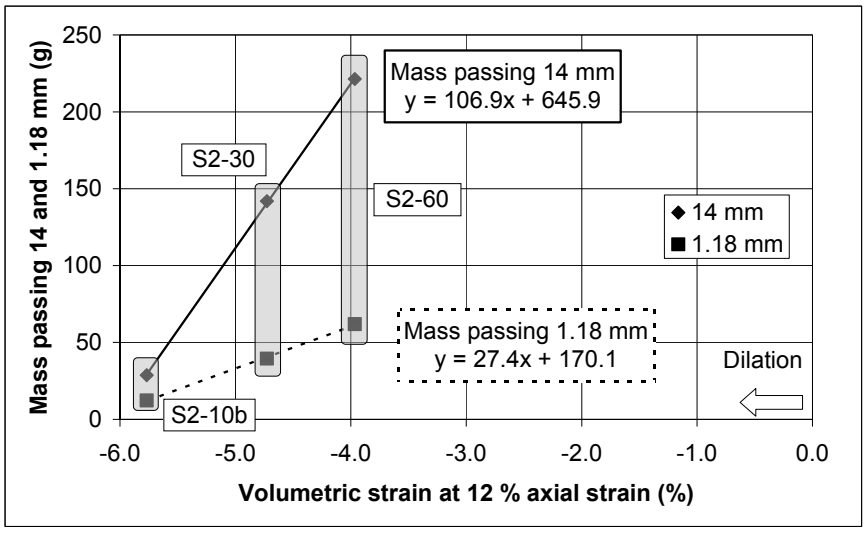

Figure 5.36. Correlation between mass passing 14 and 1.18 mm and volumetric strain at 12 % axial strain from Series 2 (monotonic tests on limestone)

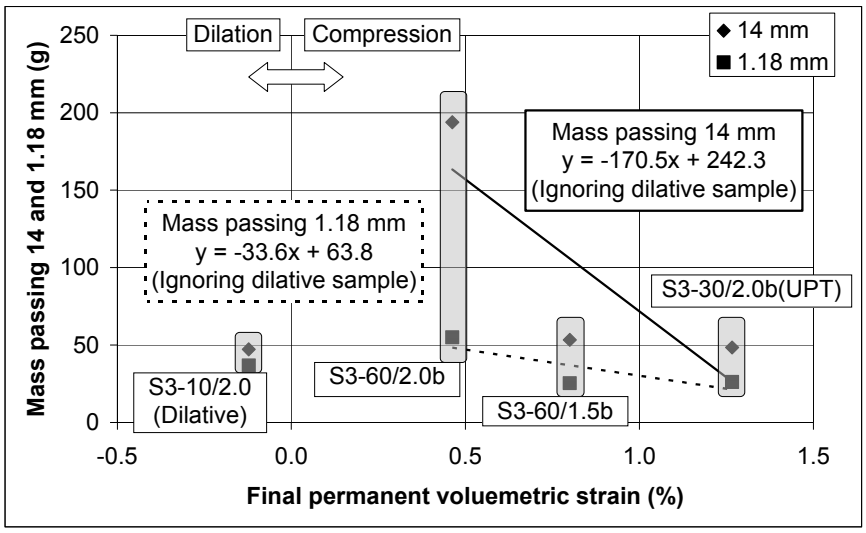

Figure 5.37. Correlation between mass passing 14 and 1.18 mm and volumetric strain from Series 3 (cyclic tests on limestone)

5.9. Conclusion

The triaxial apparatus in this project was used to investigate the ballast behaviour under various monotonic and cyclic conditions. Unlike normal triaxial apparatus, the system in this project measures axial displacement and volume change instead of axial and radial displacements. The volume change measurement is measured by a differential pressure transducer that records the head difference between the water that surrounds the sample in the inner cell and the fixed water level in the reference tube as shown in Figure 5.2. As the sample volume changes, the water level in the inner cell changes. The differential pressure transducer registers the change in head and converts it to the volume change reading. However, the differential pressure transducer is a major problem in this project as it was highly sensitive and easily damaged.

While the differential pressure transducer was damaged and sent for repair, three alternative methods of volume change measurement were tried. The first method is simply reading the change of water level from the scale on the inner cell neck. The scale was originally for double checking the accuracy of the volume change measurement from the differential pressure transducer. The reading from this method cannot be expected to be highly accurate. Furthermore, resilient volume change cannot be obtained from this method due to a very small change of water level in a cycle.

The second method was an image analysis. Many photographs of the sample were taken during a test. The sample movement could then be analysed from the series of photographs by a computer program called "GeoPIV" to obtain axial and radial strains of the sample from the vertical and horizontal movements. Even though a reasonably accurate permanent axial strain could be obtained from this method, it was later realised that the horizontal movement of the sample was not the true radial strain. The volume change measurement was therefore changed to the third one.

The third method used an ultrasonic proximity transducer. This transducer uses sound wave above the audible limit to measure the distance from the transducer to a surface. It was used in the system to look directly down to the water in the inner cell by clamping it to the shaft supporting the load cell with the outer cell removed. However, the shaft was found to be moving laterally due to uneven settlement of ballast. Therefore, the volume change measurement had to be by the differential pressure transducer as it came back from repair at that time.

The uses of the image analysis and UPT have potential for volume change measurement. However, they still need further development. This cannot be done in this project as the testing needed to continue and the current test system is not readily compatible with other methods of volume change measurement.

After the differential pressure transducer was used again, it was found that its sensitivity did not stay constant. This problem was temporary solved by calibrating the differential pressure transducer before and after each test to obtain a calibration factor that converted the volume change reading to the real volume change. Even though the sensitivity did not stay constant from different tests, it did not change within a test.

The triaxial tests in this project were grouped into three series. Series 1 was to observe the test repeatability by performing cyclic loading on granite A. All tests in Series 1 were performed with cell pressure of 90 kPa and q/p'_{max} of 1.5. It was found from this series that:

- The tests were repeatable as the permanent axial and volumetric strains, resilient modulus, Poisson's ratio, and breakage could be reproduced with small discrepancies from different tests.
- The electrical drift from the differential pressure transducer affected the measurement of volume change and calculation of Poisson's ratio.
- The breakage from granite A was small probably due to small LAA and MDA values. Therefore, limestone, which has larger LAA and MDA, was used in the other series of tests.

Series 2 was monotonic tests on limestone with three different cell pressures (10, 30, and 60 kPa). The samples were loaded at 1 mm per minute to approximately 12% axial strain to ensure that the sample would not touch the inner cell due to the expansion. It was found that the peak strength was reached in each sample. The volume change in this series was measured by reading the inner cell neck as the differential pressure transducer was sent for repair.

Various cyclic tests on limestone were performed in Series 3. The volume change of most tests in this series was measured by the differential pressure transducer. The image analysis and UPT were used in the other tests. The volume change measurement could not be obtained from the test with image analysis due to the problem with radial strain measurement.

An attempt was made to correlate the breakage with volumetric strain in both Series 2 (monotonic tests on limestone) and 3 (cyclic tests on limestone). It was found in Series 2 that larger dilation leads to smaller breakage probably because particles in a sample can rearrange themselves better with larger dilation. However, Series 3 shows the opposite finding as the larger contraction of sample leads to smaller breakage (ignoring the dilative sample in the series) even though the correlation is not as good as Series 2. This is because the sample behaviour in Series 2 was dilative while it was compressive in Series 3.

6. Comparison of results for RTF and triaxial tests

To compare the test results from the RTF to triaxial tests, the stress conditions under the loading area of the RTF should be known and are approximated by the Shell BISAR computer program following Kwan (2006) who used the program to approximate the settlement from the RTF. This program is normally used to compute elastic stresses, strains, and deflections in a pavement structures with up to ten layers of material from circular uniformly distributed loads at the surface. It assumes that the pavement structure has an infinite horizontal extent. This program was chosen to approximate the stress conditions in the RTF due to its simplicity. The results from RTF test 6 and Series 3 triaxial tests will be compared as they all were performed on limestone and various stress conditions were examined in Series 3 triaxial tests.

As BISAR can only simulate conditions under a circular load, a series of circular loads is arranged as shown in Figure 6.1 to simulate the load from the sleeper. The figure also indicates four points where stresses are computed at various depths below. These are located at x = 190, 722.5, 960, and 1,440 mm. The total area of the circular loads is equal to the area of the sleeper and the diameter of each circle is not much different from the sleeper width. Furthermore, the circles do not overlap to avoid stress concentration. As a result, nine circular loads were used to represent the load from the sleeper. Each circle has a diameter of 320 mm.

According to the contact pressure at the sleeper base (Shenton, 1974), previously shown in Figure 2.36, the distribution can be simplified as shown in

Figure 6.2. The simplified stress under the middle third of the sleeper is approximately 3.33 times smaller than the stress on both of its sides. To represent the maximum load of 94 kN in the RTF and keep the loading proportion, each circle in the middle third area applies 51.7 kPa (i.e., low stress area) while each of the other circles applies 155 kPa (i.e., high stress area) as shown in Figure 6.1.

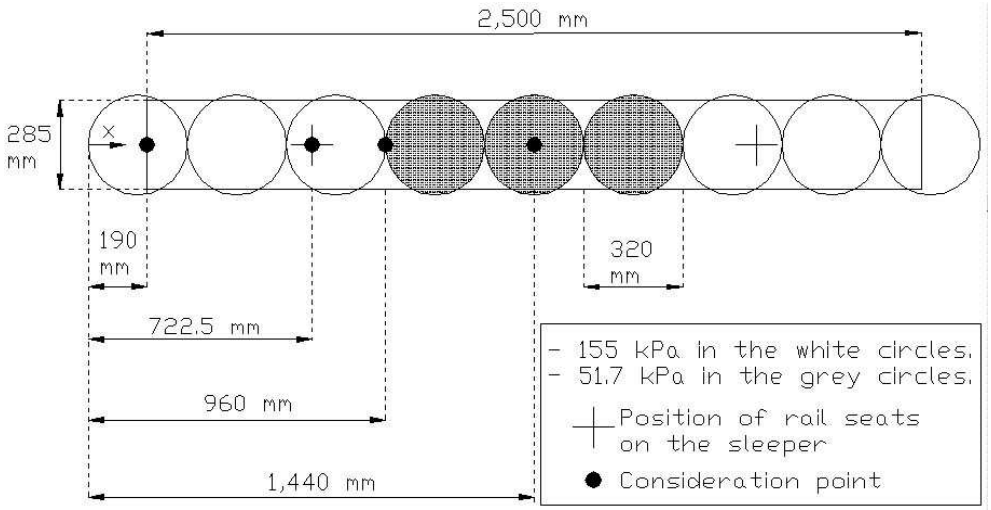

Figure 6.1. Loading arrangement for the analysis in BISAR

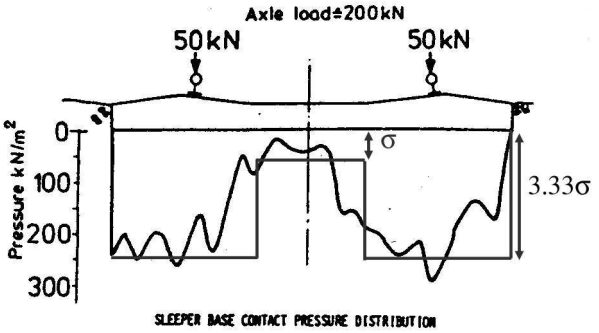

Figure 6.2. Simplification of sleeper base contact pressure distribution (Shenton, 1974)

There are three layers of materials in this analysis to simulate the ballast, subgrade, and concrete floor below the subgrade in the RTF. Under each of the four points shown in Figure 6.1, stresses are calculated at 15, 45, 75, …, 255, and 285 mm below the top of the ballast layer and at 50 mm below the top of the subgrade as shown in Figure 6.3. The figure also shows the pavement structural details with Young's modulus and Poisson's ratio for each layer. The Young's moduli and Poisson's ratios of the subgrade and concrete floor are the same values used in the BISAR analysis in Kwan (2006). A relatively large number of Young's modulus is chosen for concrete floor to represent a very stiff base. The Young's modulus and the Poisson's ratio of ballast are 175 MPa and 0.4. These are the average values of the resilient modulus and Poisson's ratio from the triaxial tests in series 3 (cyclic tests on limestone) and are also comparable to the values used by Kwan (2006) which are 100 MPa and 0.3.

The average vertical stress at 50 mm below the top of the subgrade under the rail seat from the pressure cell in the RTF is 43 kPa while the vertical stress at the same place from BISAR analysis is approximately 38 kPa. It can be seen that the values from the pressure cell and analysis are comparable.

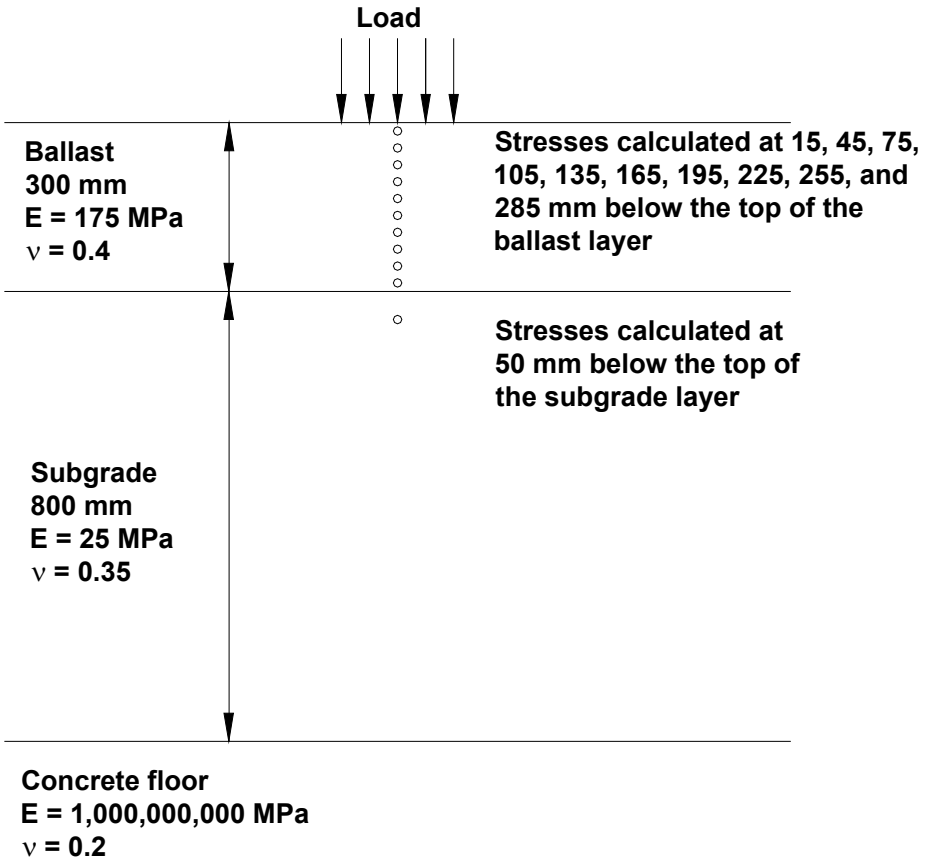

Figure 6.3. Structural details for the analysis in BISAR

Principal stresses obtained from each point in the ballast layer are converted to the three-dimensional stress invariants q and p' as shown in Equations 6.1 and 6.2 (Powrie, 1997). Even though the directions of the principal stresses obtained from the calculation are not vertical and horizontal due to the effect of principal stress rotation, these stress invariants calculated from the principal stresses are used as the equivalents of the deviatoric stress and average principal stress in a triaxial test. After obtaining both stress invariants, the equivalent confining stress and q/p'_{max} for a triaxial test can, hence, be calculated. The equivalent confining stress is shown in Equation 6.3 and the equivalent q/p'_{max} is simply dividing the stress invariant q by the stress invariant p'.

$$q = \sqrt{\frac{(\sigma'_1 - \sigma'_2)^2 + (\sigma'_1 - \sigma'_3)^2 + (\sigma'_2 - \sigma'_3)^2}{2}} \quad (6.1)$$

$$p' = \frac{\sigma'_1 + \sigma'_2 + \sigma'_3}{3} \quad (6.2)$$

$$\sigma'_{c,e} = \frac{3p' - q}{3} \quad (6.3)$$

where σ'_1 = Major principal stress

σ'_2 = Intermediate principal stress

σ'_3 = Minor principal stress

$\sigma'_{c,e}$ = Equivalent confining stress in triaxial test

Figure 6.4 shows the plot between the equivalent confining stress and ballast depth. Each line of the plot represents the confining stress under each point in Figure 6.1. It can be seen that below 150 mm, the confining stress starts to become negative. This is because the program assumes an infinite horizontal extent of the pavement structure. It can be seen that the stress conditions at x = 190 and 722.5 mm are the same and significantly different from the stress conditions at the other two points. This is because one of those other two points is at the point where the stress magnitude drops and the other is in the middle of the low stress area (see Figure 6.1). As both x = 190 and 722.5 mm are equal in the high stress area, the stress conditions from these points will therefore be used as the prediction of the stress conditions under the rail seat in the RTF.

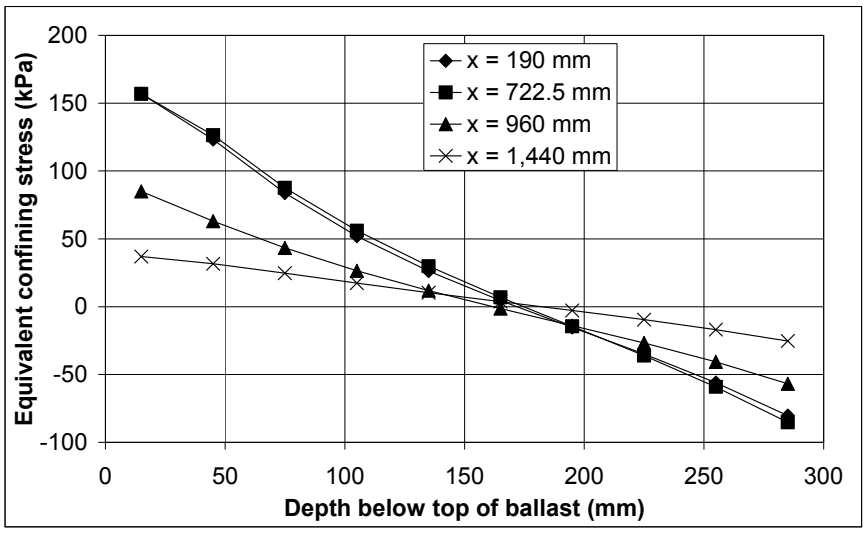

Figure 6.4. Equivalent confining stress vs depth below top of ballast from BISAR analysis

Figure 6.5 shows the plot of equivalent q/p'_{max} against confining stress from the predicted stress conditions under the rail seat using BISAR together with the stress conditions from Series 3 triaxial tests. Only confining stresses between 0 and 60 kPa are shown in the plot for comparative purposes. It can be seen that the stress conditions from the triaxial tests except those with 60 kPa confining stress and q/p'_{max} of 2.0 (S3-60/2.0a and b) are reasonable compared to the prediction.

It should be noted that BISAR predicted q/p'_{max} over 3 when the confining stress is low. This is practically impossible as q/p'_{max} over 3 results in negative confining stress. Such condition was obtained from BISAR because it assumed an infinite horizontal extent of pavement.

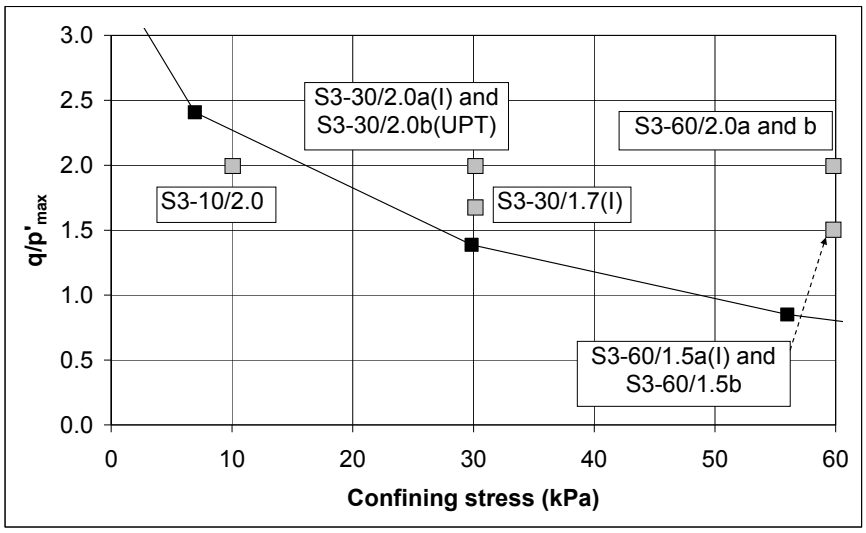

Figure 6.5. Stress conditions from BISAR analysis and Series 3 triaxial tests

The permanent axial strains from all triaxial tests in Series 3 are compared to the strain from the RTF test 6 (settlement divided by the initial ballast height). This is because both Series 3 triaxial tests and RTF test 6 were performed on limestone. The strains from those tests are plotted against the number of cycle and shown in Figure 6.6. It should be noted that the strain from the RTF after cycle 100,000 is not included in the plot as the triaxial tests were performed for 100,000 cycles. Also, to compare the results on the same basis, unlike the comparison of results in Chapter 5, the first cycle permanent axial strains are not removed from all test results. This is because the first data point of the settlement from the RTF is at cycle 100 instead of cycle 1 as the settlement data from the RTF was collected manually unlike the automatic data collection in the triaxial tests. Therefore, the strain from the first cycle of loading in the RTF cannot be removed. It can be seen that the strain from S3-30/1.7(I) is very large. This is because the sample was overly compressed due to the fast initial loading rate in the test as explained in Section 5.4.2 (Image analysis section).

Similar to the permanent axial strain, the particle size distributions of particles smaller than 22.4 mm from all tests are shown in Figure 6.7. Both permanent axial strain and particle size distribution results from all triaxial tests except S3-60/2.0a and b are comparable to the results from the RTF. This is also in agreement with the comparison of the stress conditions in Figure 6.5 where the stress condition of these two tests is considerably different from the prediction.

However, there are some deficiencies of the BISAR as follows.

- Only circular loads can be simulated in BISAR.
- The stress/strain calculation in BISAR is based on an elastic approach.
- BISAR cannot simulate cyclic loading.
- The program permits and calculates negative horizontal stress which is not permissible for granular material.

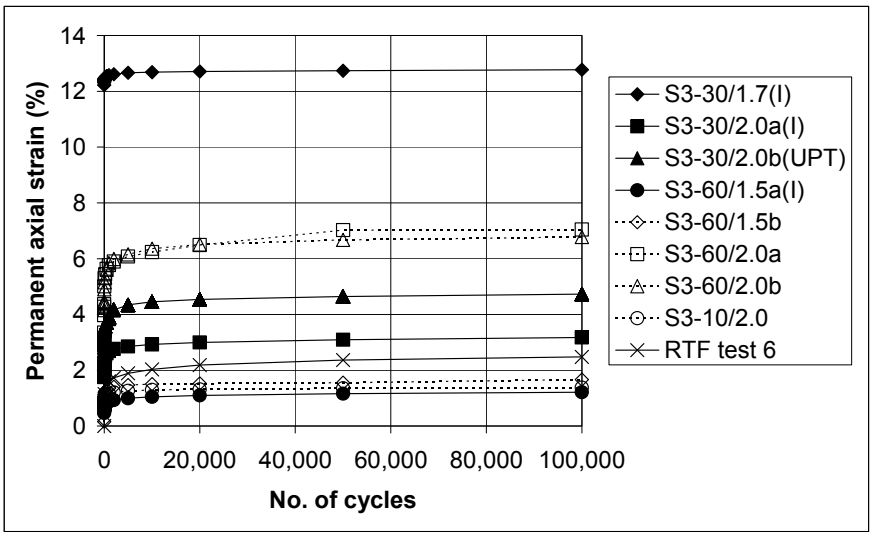

Figure 6.6. Permanent axial strains from triaxial tests in Series 3 and RTF test 6

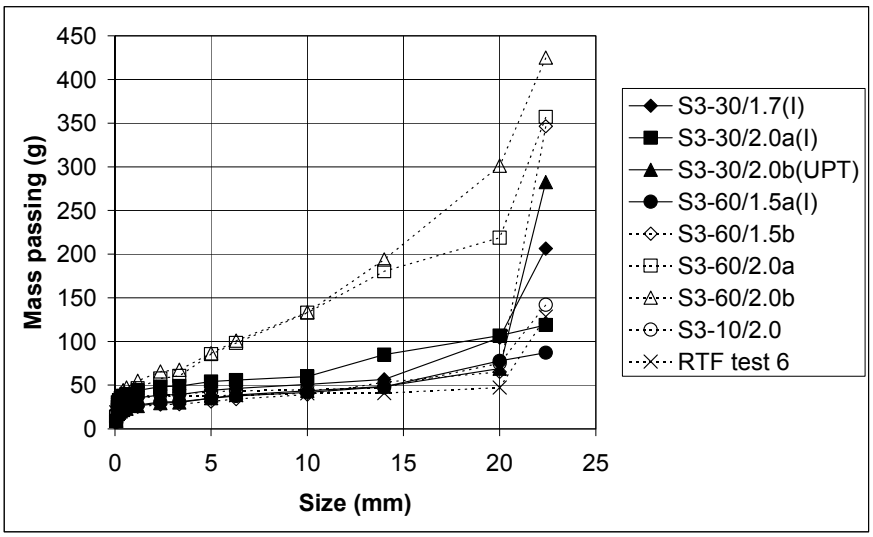

Figure 6.7. Particles smaller than 14 mm from triaxial tests in Series 3 and RTF test 6

A simple analysis can be performed to compare the results from the RTF test with the triaxial test. This analysis is based on the findings from Selig and Waters (1994) and Shenton (1978). According to the box test results of Selig and Waters (1994), the observed horizontal stress in ballast eventually reached 30 kPa as previously shown in Figure 2.35. And from Figure 6.2, Shenton (1974) found that the maximum contact pressure at sleeper base was approximately 200 – 250 kPa

From both findings, it is reasonable to simulate the condition of ballast under traffic loading in the RTF by a cyclic triaxial test with constant confining stress of 30 kPa and maximum axial stress of 200 – 250 kPa. The values of constant confining stress and maximum axial stresses result in q/p'_{max} from 1.96 to 2.13. And it is shown that the permanent axial strain (Figure 6.6) and particle size distribution (Figure 6.7) from cyclic triaxial tests on limestone with 30 kPa confining stress and q/p'_{max} of 2.0 are comparable to the traffic loading test on

limestone (RTF test 6). Even though this analysis method is simple and gives a quick estimation of a stress condition, it might be doubtful as it is based on others' research and the conditions of those research projects are not fully understood.

Therefore, it can be concluded that even though BISAR has some deficiencies, it can estimate the stress condition in the RTF. Also, triaxial tests with the conditions that match the line in Figure 6.5 are recommended for further research.

7. Conclusions and recommendations for further research

7.1. Conclusions

The conclusions that can be drawn from this research are:

- LAA and MDA values correlate well with the breakage from tamping.
- Index tests such as LAA and MDA are economical and easy to perform. They can also assess ballast performance well in terms of durability.
- The settlements of different ballast types from the traffic loading simulation in the RTF are similar to each other. The settlement from the RTF unreinforced tests were about 60 % of the settlement that would be expected on site. This is probably because the traffic loads on site are larger particularly if dynamic effects are present. However, this comparison might not be on the same basis as the researchers did not report all test conditions and parameters.
- The overall degradation from the RTF tests is lower than the site degradation because of the higher traffic loads and also there are fouling materials mixing with the ballast such as wagon spillage and airborne dirt which would exacerbate degradation.
- The level of ballast degradation from RTF traffic loading is similar to the previous research (Awoleye, 1993). However, it should be noted that the scale and ballast density in that research is smaller than the RTF.
- Tamping can improve track settlement but cause faster rate of settlement afterwards.

- The results from the RTF tamping bank suggest that plunging of the tamping tines into the ballast layer is more damaging than squeezing.
- Ballast degradation was much less from the tamping tests in this project compared to the work done by Wright (1983).
    - Although the tamping bank was a refurbished full-scale device, it utilised a hydraulic vibrating actuator instead of a mechanical vibrator and was mounted in a frame which did not have the same mass as a 35-tonne tamping machine carriage.
    - These differences may have contributed to a reduction in damage to the ballast for tamping tests.
    - This type of vibrator may be advantageous as it is less likely to damage the ballast than the fixed amplitude mechanical vibrator. However, this should be further studied in more detail.
- Using painted ballast in columns beneath the tamping tines, in the squeezed location, and under the rail seating was a successful means of quantifying breakage.
- The triaxial test on the ballast was repeatable. The permanent axial and volumetric strains, resilient modulus, Poisson's ratio, and breakage could be quantified with small discrepancies between tests.
- According to the monotonic triaxial test results, larger dilation is accompanied by smaller breakage. This is probably because the particles in the sample can rearrange more freely with larger dilation.
- With the same confining stress, the breakage of the ballast sample increases with increasing deviatoric stress.

- The range of confining stresses in the cyclic triaxial tests was not large enough to observe the effect of confining stress on ballast breakage. The confining stresses used in the tests are in the optimum degradation zone (30 – 75 kPa, Figure 5.34) according to Indraratna et al. (2005).
- Even with some deficiencies, the BISAR elastic model can predict the stress condition under traffic loading in the RTF as shown in the line in Figure 6.5.

7.2. Recommendation for further research

The recommendations for the RTF are to make its performance more representative of the in service loading conditions. A feature of the laboratory tamping bank is that it has the facility to vary parameters which can influence the damage to the ballast. Modifications to the triaxial tests are also recommended to improve performance. These points and ideas for further experiments are outlined below.

- Ballast of each size does not need to be prepared to make up a specified grading for the samples in both the RTF and triaxial test. Instead, particles smaller than 22.4 mm should be removed from the sample. However, it should be ensured that the samples conform to the grading specification.
- In the RTF, the ballast under the sleeper at the rail seating should be at a slightly higher level than under the middle portion of the sleeper to ensure that the stress on ballast under the rail seating is higher than the centre.

- The magnitude and frequency of traffic loading in the RTF can be increased to simulate the effect of the dynamic loading and to reduce the test duration. However, the capacity of the facility has to be increased to achieve this.
- The arrangement for the extra confinement test in the RTF could be extended by dividing the pit into four sections. More test results can be generated with this type of installation. For example, each section can be filled with different sizes of ballast to observe the resulting breakage.
- Ballast gradings used for testing in both the RTF and triaxial tests can be varied to observe its effect on the settlement and degradation.
- The fines collector and accelerometer could be further developed to measure the fines generated during each test and the resilient displacement of the subgrade in the RTF.
- The amplitude of tamping tine vibration should be monitored and recorded during each tamp to detect any changes in response to the ballast behaviour.
- The amplitude of tamping tine vibration, hydraulic oil pressure, rate of lowering tamping tines, and shape of tamping tines can all be varied in the RTF tamping bank to observe the resulting breakage, the performance of settlement improvement, and the rate of settlement from subsequent traffic loading.
- As the tamping bank in this project caused reduced particle breakage, it could be tried on site.

- Triaxial tests with stress conditions matching the line in Figure 6.5 should be performed and compared with traffic loading tests from the RTF.
- The image analysis can be further developed to measure the radial strain of a sample by placing a series of stickers on the sample and using two cameras. More details can be found in Section 5.4.2.
- Another model of ultrasonic proximity transducer can be used to measure the sample volume change. This model is a flat transducer with a transmitter that operates at right angles from the end rather than the axial cylindrical type used in this project. This would be easier to locate above the neck of the inner cell as shown in Figure 7.1. This method does not require a significant modification to the system.
- The ultrasonic proximity transducer can also be used to measure sample volume change in a different way as shown in Figure 7.2.
    - This method does not use the inner cell. The outer cell is fully filled with water. The transducer is placed above the pipe that connects to the outer cell. As the volume of sample changes, the transducer can register the change of water level in the pipe. The change of the water level can be converted to the volume change by the known cross-sectional area of the pipe.
    - Since the water is open to the atmosphere, the sample must be under vacuum. The limitation of this method is that a modification of the outer cell is required and a robust vacuum system is also required and the maximum equivalent confining pressure from the vacuum is 100 kPa.

- This limitation can be overcome by using pressurised water to apply the confining pressure instead of using vacuum but the system has to be sealed above the water surface in the pipe and compressed air with equal pressure must be supplied between the water surface and the seal (Figure 7.2).
- Direct measurement of the water surface level is used in this method instead of measuring the water head difference, which can fluctuate with the air pressure in the arrangement used in this project. Also, the water level in this recommended system will not oscillate with the rapid movement in the system. Therefore, the response during a cyclic test should improve.

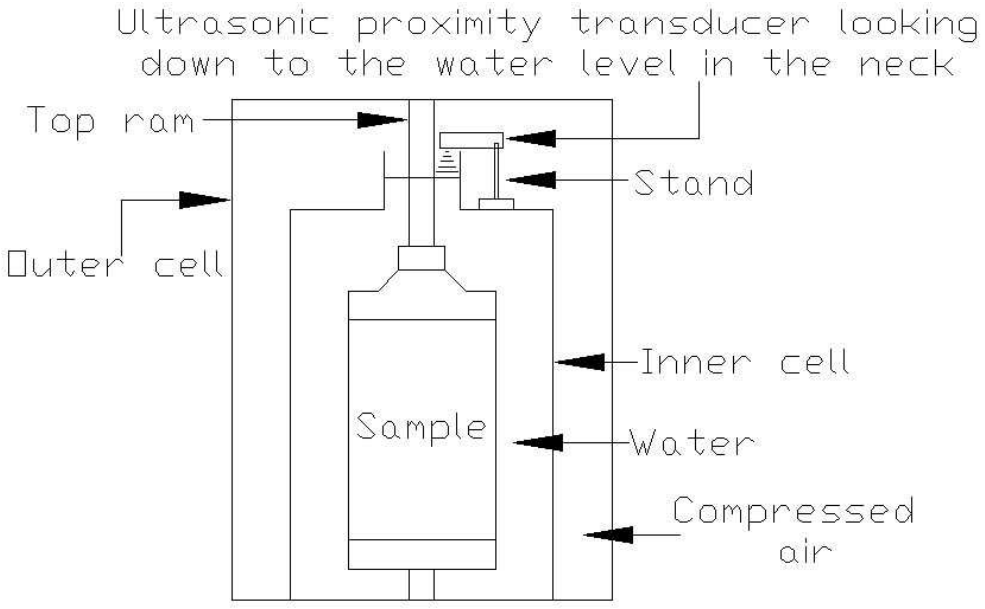

Figure 7.1. Use of alternative ultrasonic proximity transducer to measure volume change

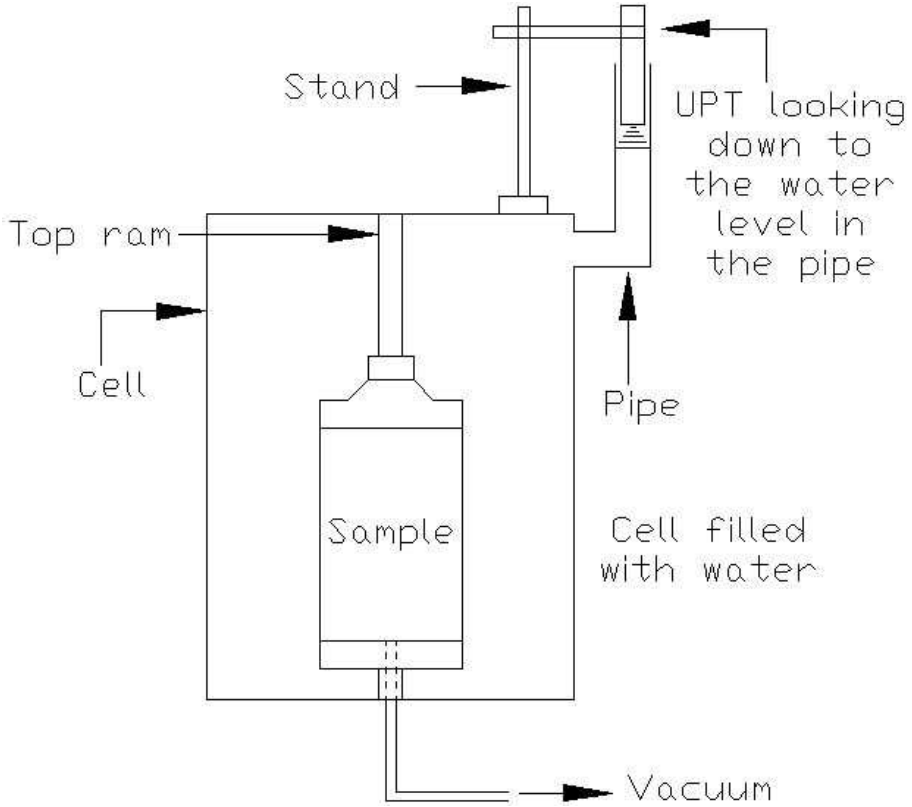

Figure 7.2. Alternative method of volume change measurement by the ultrasonic proximity transducer

References

1. Aitken, P. (2006). Exploring Excel's function part 6: TTEST(). [online], 14 April. Available at <URL:http://www.quepublishing.com/articles/article.asp?p=461631&rl=1> [Accessed 2 Dec 2006].
2. Ashby, M. F. and Jones, D. R. H. (1996). *Engineering materials 1*. Oxford: Butterworth-Heinemann.
3. Ashby, M. F. and Jones, D. R. H. (1998). *Engineering materials 2*. Oxford: Butterworth-Heinemann.
4. Awoleye, E. O. A. (1993). Ballast type - ballast life predictions. Derby, *British rail research* LR CES 122, October 1993.
5. Barksdale, R. D. (1972). Laboratory evaluation of rutting in basecourse materials. *Proc., 3rd Int. Conf. on Struct. Des. of Asphalt Pavements*, pp. 161-174.
6. Brown, S. F. and Hyde, A. F. L. (1975). Significance of cyclic confining stress in repeated-load triaxial testiing of granular material. *Transportation research record* **537**, pp. 49-58.
7. Bishop, A. W. and Green, G. E. (1965). The influence of end restraint on the compression strength of a cohesionless Soil. *Geotechnique* **15**, pp. 243-266.
8. Bombardier Inc. (2007). Commuter trains. [online], Available at <URL:http://www.bombardier.com> [Accessed 24 Aug 2007].

9. Boyce, J. R., Brown, S. F. and Pell, P. S. (1976). The resilient behaviour of granular material under repeated loading. *Eighth conference of Australian road research board*, pp. 1-12.
10. British Standard: BS EN 933-3 (1997). *Determination of particle shape- Flakiness index.*
11. British Standard: BS EN 1097-1 (1996). *Tests for mechanical and physical properties of aggregates- Determination of the resistance to wear (micro-Deval).*
12. British Standard: BS EN 1097-2 (1998). *Tests for mechanical and physical properties of aggregates- Methods for the determination of resistance to fragmentation.*
13. British Standard: BS EN 13450 (2002). *Aggregates for railway ballast.*
14. British Standard: BS EN 1097-6 (2000). *Determination of particle density and water absorption*.
15. Collins, I. F. and Boulbibane, M. (2000). Geomechanical analysis of unbound oavements based on shakedown theory. *Journal of geotechnical and geoenvironmental engineering*, ASCE. Vol. 126, No. 1, pp. 50-59.
16. Cundall, P. A. and Strack, O. D. L. (1979). A discrete numerical model for granular assemblies. *Géotechnique* **29**, No. 1, pp. 47-65.
17. Davidge, R. W. (1979). *Mechanical behaviour of ceramics*. Cambridge university Press.
18. Dawson, A. R., Thom, N. H. and Paute, J.-L. (1996). Mechanical characteristics of unbound granular materials as a fucntion of condition. *Flexible pavements*. A. G. Correia ed. Rotterdam, A. A. Balkema. pp. 35-44.

19. Devore, J. and Farnum, N. (1999). *Applied statistics for engineers and scientists*. Belmont, California, Brooks/Cole publishing company.

20. Duncan, J. M. and Dunlop, P. (1968). The significance of cap and base restraint. *Journal of the soil mechanics and foundation division*, Proceeding of ASCE. Vol. **94(SM1)**, pp. 271-290.

21. Fair, P. (2003). *The geotechnical behaviour of ballast materials for railway track maintenance*. Ph.D. dissertation, University of Sheffield.

22. Fukumoto, T. (1992). Particle breakage characteristics in granular soils. *Soils and foundations* **32**, No. 1, pp. 26-40.

23. Golightly, C. R. (1990). *Engineering properties of carbonate sands*. Ph.D. dissertation, Bradford University.

24. Hertzberg, R. W. (1996). *Deformation and fracture mechanics of engineering materials*. New York: John Wiley & Sons.

25. Heydinger, A. G., Xie, Q., Randolph, B. W. and Gupta, J. D. (1996). Analysis of resilient modulus of dense- and open-graded aggregates. *Transportation research record* **1547**, pp. 1-6.

26. Hicks, R. G. and Monismith, C. L. (1971). Factors influencing the resilient properties of granular materials. *Highway research record* **345**, pp. 15-31.

27. Hornby, E. (2007). *Personal communication*, 11 June, University of Nottingham.

28. Indraratna, B., Ionescu, D., and Christie, H. D. (1998). Shear behaviour of railway ballast based on large-scale triaxial tests. *Journal of geotechnical and geoenvironmental engineering* **124**, No. 5, pp. 439-449.

29. Indraratna, B., Lackenby, J. and Christie, D. (2005). Effect of confining pressure on the degradation of ballast under cyclic loading. *Geotechnique* **55**, No. 4, pp. 325-328.
30. Ionescu, D. (2004). Ballast degradation and measurement of ballast fouling. *Seventh railway engineering conference*, Commonwealth Institute, London.
31. Key, A. (1998). *Behaviour of two layer railway track ballast under cyclic and monotonic loading*, Ph.D. dissertation, University of Sheffield.
32. Knutson, R. M. (1976). *Factors influencing the repeated load behaviour of railway ballast*, Ph.D. dissertation, University of Illinois Urbana-Champaign.
33. Knutson, R. M. and Thompson, M. R. (1978). Permanent-deformation behavior of railway ballast. *Transportation Research Record* **694**, pp. 47-53.
34. Kolisoja, P. (1997). Factors affecting deformation properties of coarse grained granular materials. *International conference on soil mechanics and foundation engineering*, pp. 337-342.
35. Kwan, Cho Ching. (2006). *Geogrid Reinforcement of railway ballast*, Ph.D. dissertation, University of Nottingham.
36. Lekarp, F. and Dawson, A. R. (1998) Modelling permanent deformation behaviour of unbound granular materials. *Construction and building materials* **12**, No. 1, pp. 9-18.
37. Lekarp, F., Isacsson, U. and Dawson, A. (2000a). State of the art I: Resilient response of unbound aggregates. *Journal of transportation engineering*, ASCE. Vol. **126**, No. 1, pp. 66-75.

38. Lekarp, F., Isacsson, U. and Dawson, A. (2000b). State of the art II: Permanent strain response of unbound aggregates. *Journal of transportation engineering*, ASCE. Vol. **126**, No. 1, pp. 76-83.

39. Lim, W. L. (2004). *Mechanics of railway ballast behaviour*. Ph.D. dissertation, University of Nottingham.

40. McDowell, G. R. (2001). Statistics of soil particle strength. *Geotechnique* **51**, No. 10, pp. 897-900.

41. McDowell, G. R. (2002). On the yielding and plastic compression of sand. *Soils and foundations* **42**, No. 1, pp. 139-145.

42. McDowell, G. R. and Amon, A. (2000). The application of Weibull statistics to the fracture of soil particles. *Soils and foundations* **40**, No. 5, pp. 133-141.

43. McDowell, G. R. and Bolton, M. D. (1998). On the micromechanics of crushable aggregates. *Géotechnique* **48**, No. 5, pp. 667-679.

44. McDowell, G. R., Bolton, M. D. and Robertson, D. (1996). The fractal crushing of granular materials. *J. Mech. Phys. Solids* **44**, No. 12, pp. 2079-2102.

45. Monismith, C. L., Seed, H. B., Mitry, F. G. and Chan, C. K. (1967). Prediction of pavement deflections from laboratory tests. *Second Int. Conf. Struct. Des. of Asphalt Pavements*, pp. 109-140.

46. Morgan, J. R. (1966). The response of granular materials under repeated loading *Proceeding of ARRB*. 3rd conference, pp. 1178-1192.

47. Ng, C. W. W., Zhan, L. T. and Cui, Y. J. (2002). A new simple system for measuring volume changes in unsaturated soils. *Canadian geotechnical journal* **39**, No. 3, pp. 757-764.

48. Oda, M. (1977). Co-ordination number and its relation to shear strength of granular material. *Soils and foundations* **17**, No. 2, pp. 29-42.

49. Pappin, J. W. (1979). *Characteristics of a granular material for pavement analysis*. Ph.D. dissertation, University of Nottingham.

50. Ping, W. V. and Yang, Z. (1998). Experimental verification of resilient deformation for granular subgrades. *Transportation Research Record* **1639**, pp. 12-22.

51. Powrie, W. (1997). *Soil mechanics: Concepts and Applications*. London, E & FN Spon.

52. Profillidis, V. A. (2000). *Railway Engineering*. Aldershot: Ashgate Publishing Limited.

53. Rahimzadeh, B., Jones, M., Hakim, B., and Thom, N. (2004). Performance testing of unbound materials within the pavement foundation. In: Dawson, A. R., ed. *Pavement Unbound*. London, Taylor & Francis group.

54. Railtrack Line Specification (2000). RT/CE/S/006 Issue 3. *Track Ballast.*

55. Railtrack Line Specification (2002). RT/CE/S/006 Issue 5. *Track Construction Standards*.

56. Railway Group Standard (2003). GT/RT5014 Issue 2. *Trackbed and Track Drainage*.

57. Raymond, G. P. and Bathurst, R. J. (1994). Repeated-load response of aggregates in relation to track quality index. *Canadian Geotechnical Journal* **31**, No. 4, pp. 547-554.

58. Selig, E. T. and Alva-Hurtado, J. E. (1982). Predicting effects of repeated wheel loading on track settlement. *Proceeding of the 2nd International Heavy Haul Conference*, Colorado Springs, pp. 476-487.

59. Selig, E. T. and Waters, J. M. (1994). *Track Geotechnology and Substructure Management*. London: Thomas Telford.

60. Shenton, M. J. (1974). Deformation of railway ballast under repeated loading conditions. *British Railways Research and Development Division*.

61. Shipway, P. H. and Hutchings, I. M. (1993). Fracture of brittle spheres under compression and impact loading I. Elastic stress distributions. *Philosophical Magazine A* **67**, No. 6, pp. 1389-1404.

62. Skoglund, K. A. (2002). *A study of some factors in mechanistic railway track design*. Ph.D. dissertation, Norwegian University of Science and Technology.

63. Suiker, A. S. J., Selig, E. T., and Frenkel, R. (2005). Static and cyclic triaxial testing of ballast and subballast. *Journal of geotechnical and geoenvironmental engineering*, ASCE. Vol. **131**, No. 6, pp. 771-782.

64. The American Society for Testing and Materials: ASTM D 1557-78 (1978). *Standard test methods for moisture density relations of soil-aggregate mixtures using 10-lb (4.54 kg) rammer and 18-in (457-mm) drop*.

65. Thom, N. H. and Brown, S. F. (1987). Effect of moisture on the structural performance of a crushed-limestone road base. *Transportation Research Record* **1121**, pp. 50-56.

66. Thom, N. H. and Brown, S. F. (1988). The effect of grading and density on the mechanical properties of a crushed dolomitic limestone. *Proceeding of the Australian Road Research Board* **14**, No. 7, pp. 94-100.

67. Thom, N. H. and Brown, S. F. (1989). The mechanical properties of unbound aggregates from various sources. *Unbound Aggregates in Roads*. R. H. Jones and A. R. Dawson eds. London, Butterworth: pp. 130-142.

68. Uzan, J. (1985). *Characterization of granular material*. Transportation Research Record **1022**, pp. 52-59.

69. Weibull, W. (1951). A statistical distribution function of wide applicability. *Journal of Applied Mechanics* **18**, pp. 293-297.

70. White, D. J. and Take, W.A. (2002). GeoPIV: Particle Image Velocimetry (PIV) software for use in geotechnical testing. *Cambridge University Engineering Department Technical Report,* **D-SOILS-TR322**.

71. White, D. J., Take, W. A., and Bolton, M. D. (2003). Soil deformation measurement using particle image velocimetry (PIV) and photogrammetry. *Géotechnique* **53**, No. 7, pp. 619-631.

72. Wright, S. E. (1983). Damage caused to ballast by mechanical maintenance techniques. *British Rail Research Technical Memorandum* TM TD 15, May 1983.